UNIVERSITÀ DEGLI STUDI DI TRIESTE

UNIVERSITÀ DEGLI STUDI DI UDINE

XXXIV CICLO DEL DOTTORATO DI RICERCA IN

AMBIENTE E VITA

MONITORING AND MODELLING CRYOSPHERE PROCESSES USING HIGH RESOLUTION SURVEYS

Settore scientifico-disciplinare:

AGR/08

DOTTORANDA
JESSICA DE MARCO

COORDINATORE
PROF. GIORGIO ALBERTI

SUPERVISORE DI TESI
PROF. FEDERICO CAZORZI

SUPERVISORE DI TESI
DOTT. LUCA CARTURAN

ANNO ACCADEMICO 2020/2021

I. Summary

Glaciers are valuable indicators of global warming, and their fluctuation can severely affect natural ecosystems and human society. They directly influence water supply, sea level and they can cause severe natural hazards. Medium- to large- sized glaciers have been widely studied to understand past, present and future responses to climate change, while smaller ice bodies tend to have a highly scattered response and deserve further investigations. For this reason, and due to the recent increase in their number as a consequence of the fragmentation of larger glaciers, smaller glaciers (<0.5 km^2) have seen a recent increase in interest and scientific research.

This thesis aims to study the recent and past behaviour of the lowermost Italian glacier, a very small glacier known as Ghiacciaio Occidentale del Montasio (Julian Alps), which is located far below the regional equilibrium-line altitude. Glacier elevation changes, mass balances, surface displacements and change in surface cover were monitored using high resolution techniques (in particular Structure from Motion Multi-View Stereo, SfM-MVS) and reconstructing Digital Elevation Models (DEMs) from historical images and maps. Glacier changes were correlated to air temperature and precipitation trends to better characterise and understand its climatic response.

The first object of the thesis was to investigate the reliability of the SfM-MVS technique for monitoring elevation changes in debris covered areas such as the lower half of the Montasio Glacier. The technique was tested over easy-to-access riverbeds with different morphologies and patterns, to point out critical aspects and minimise errors in the acquisition and processing phases. SfM-MVS proved to have high repeatability with unchanged acquisition setup, while surveys performed with different sensors might introduce systematic errors in the elevation change detection analysis. Overall, this technique was considered adequately accurate and precise for monitoring small debris covered areas, such as the Montasio Glacier.

Bases on these results, the focus moved to the recent (2006-2019) dynamics of the Montasio Glacier. Data acquired with both SfM-MVS and laser scanning (terrestrial and aerial) techniques were used to analyse the annual mass balance of the glacier. The study confirmed a complex relationship between the glacier mass balance and the extent of the debris-covered area. It also highlighted the unusual behaviour of this glacier, characterised by: i) a remarkably lower imbalance compared to others Alpine reference glaciers, ii) a nonsignificant correlation of mass balance with air temperature, and iii) a high sensitivity to precipitations during the accumulation season.

The analysis of the recent dynamics opened new questions regarding the long-term climatic sensitivity of the glacier and its relationship with the debris cover, at the secular time scale. Therefore,

an historical analysis was performed to reconstruct glacier DEMs for five different years (1920, 1948, 1982, 2006 and 2020), which enabled the calculation of the geodetic mass balance rate in the last century. The Montasio Glacier behaviour was comparable with the other alpine glaciers trough the 20th Century until the early 1980s. In the recent decades, however, it progressively decoupled from the typical response of alpine glaciers, showing increasing departure and much lower imbalance. The progressive increase in thickness and extent of the debris layer observed after the 1940s, in association with the avalanche feeding and the shadowing effect of the Mt. Jof di Montasio, were confirmed as the main causes of the current minor imbalance and low sensitivity to air temperature fluctuations.

This thesis demonstrates that high-resolution SfM-MVS represents a cost-effective method, which can be successfully adopted for monitoring the response of glaciers with characteristics similar to the Montasio Glacier. The study provides a full characterisation of the current and past dynamics and behaviour of the Montasio Glacier, from both climatic and glaciological perspectives. Based on the results of this study, it can be assumed that a transition to periglacial conditioning (i.e. a transformation to a rock glacier) is improbable, and that the glacier should not quickly disappear in the near future.

II. Publications and conferences

PUBLICATIONS

De Marco, J.; Maset, E.; Cucchiaro, S.; Beinat, A.; Cazorzi, F. Assessing Repeatability and Reproducibility of Structure-from-Motion Photogrammetry for 3D Terrain Mapping of Riverbeds. *Remote Sens.* **2021**, *13*, 2572. *https://doi.org/10.3390/rs13132572*

De Marco, J.; Carturan, L.; Piermattei, L.; Cucchiaro, S.; Moro, D.; Dalla Fontana, G.; Cazorzi, F. Minor Imbalance of the Lowermost Italian Glacier from 2006 to 2019. *Water* **2020**, *12*, 2503. https://doi.org/10.3390/w12092503

De Marco, J.; Carturan, L.; Maset, E.; Cucchiaro, S.;Visintini D.; De Infanti R.; Cazorzi, F. Century-long multi-source analyses highlight decreasing vulnerability for a small, debris-covered and avalanche-fed glacier in the Eastern Italian Alps. (*Under submission*)

Carturan, L.; Bondesan, A.; Carton, A.; Cazorzi, F.; Cucchiaro, S.; **De Marco, J.**; Piermattei, L. The glaciated landscape across the first world war front: quantitative reconstructions based on digitized historical images and modern techniques. Geografia Fisica e Dinamica Quaternaria **2020**, 43, 143-155. DOI: 10.4461/GFDQ.2020.43.

POSTERS

De Marco, J.; Zaramella M.; Borga M.; Cazorzi F.; Carturan, L.; Dalla Fontana G. Modelling the spatial variability of snow water equivalent and snow cover by using a topography-based distribution function snowmelt model: comparison with a fully distributed model. In: EGU General Assembly 2019, Vienna, Austria.

Contents:

Chapter 1

Introduction

1 Introduction

1.1 Glaciers significance and their importance for climate change monitoring

Glaciers and ice caps outside Greenland and Antarctica have considerable mass losses which are contributing significantly to the global sea level rise since the 1990s, even though they only contain a fraction of the worldwide ice volume [1,2]. In fact, their fluctuations can severely affect global trends in freshwater supply [3] and it has been foreseen that their reduction due to global warming will have important consequences during 21st century [4,5].

Moreover, glaciers are considered important contributors to sea level changes [6–8]; in fact, a significant increase in glacier mass loss rates has been observed in the last three decades, and it was estimated to be 335 billion tons year^{-1} equivalent to almost 1 mm year^{-1} in sea levels rise [9]. In general, glaciers alone caused a 9,625 billion tons of ice loss between 1961 and 2016, that is equivalent to 27 mm sea-level rise [10].

Nowadays, glaciers are key indicators in a global warming scenario, since their mass balance allow to perform inference analysis on climatic changes [11]. In glaciology, the mass balance (or climatic mass balance) measures the changes (gains and losses in water equivalent - W.E.) of all or a part of a glacier during a specified time span [12], which usually corresponds to one hydrological year recording the interval between two successive annual minima. There are different approaches to estimate the mass balance, that differ in the adopted technologies for data acquisition and post processing workflows.

The direct or glaciological method is based on field measurements of ablation and accumulation totals [13–15]. In this case, mass balance measurements are performed on single points all over the glacier and interpolated to obtain a distributed mass balance. Most of the longest mass balance time series have been performed with this method [8]. However it is time consuming, prone to errors and not always applicable due to glaciers characteristics and hazards [16]. This approach may introduce errors based on sampling points number and distribution [17,18].

The hydrological method estimates the net glacier mass balance via modelling water dynamics in the glacier catchment. It has been used in many parts of the world (e.g. 19–21), although mostly on glaciers smaller than 10 km^2 [12]. The procedure requires an accurate estimation of all components (precipitation, runoff, evaporation, and the changes of other water store) which are not always easily achievable. In fact, precipitations present a complex spatial variation especially at high altitudes, and evaporation is difficult to calculate [22].

Then, we can cite the gravimetric method, which employees the Gravity Recovery and Climate Experiment (GRACE) to make direct measurements of changes in the Earth's mass distribution over large regions. Major advantages of this approach are that it directly determines changes in mass rather than volume and it is able to capture annual variations resulting from winter accumulation and summer ablation [23–25]; however, it can be applied only to very large areas [12].

Last but not least, there is the geodetic method, which is the main approach used in this thesis. It derives glacier mass balance from the difference between Digital Elevation Models (DEMs) of the glacier surface corrected for the average density of ice, firn and snow. This method can be based on different remote sensing technologies such as satellites images, satellite interferometry, aerial photogrammetry, Structure from Motion, terrestrial and aerial laser scanning. An important limitation of these approaches is the estimation of snow and ice densities which are likely to change through time and need to be assumed or modelled [26].

1.2 Very small glaciers

Glaciers are defined as "perennial masses of ice, and possibly firn and snow, originating on the land surface by the recrystallization of snow or other forms of solid precipitation and showing evidence of past or present flow" [27]. However, while this definition is unanimously accepted, there in not a complete agreement about the "very small glacier" class definition. In fact, as summarised in Fischer (2018) [28], they can be defined using qualitative methods, mainly based on morphologic aspects or using quantitative methods based on glacier size thresholds (e.g. 27,29,30).

In this thesis the quantitative definition of Huss and Fischer (2016) [30] was adopted, which defines "very small" the glaciers that occupy less than 0.5 km^2. Very small glaciers cover around 13% of the global glacier area and retain 5% of overall ice volume, but they are widespread, representing 80-90% of the glaciers in mid- and low-latitude mountain range [30–32]. With these numbers, they act as an important water storage regulating the hydrological regime in several mountain areas or in poorly glacierized drainage basins [30,33–35].

For this reason, there is an increasing concern about water reservoirs in the current global warming scenario [30,33,36]. Indeed, estimation reported in Huss and Fischer (2016) [30] suggest that before 2040, 90% of very small glacier volume will be lost and around 70% of them will be completely vanished.

Very small glaciers have a very broad variety of characteristics in terms of morphology, surface type, dynamic and location. Some of them can be highly influenced by local topography, like those located in extremely shaded cirques or niches, that provide protection from direct solar radiation, avalanche snow, and debris, which slow down the mass loss process [37,38]. Indeed, even if their overall mass balance sensitivity to air temperature and precipitation is similar to that of larger ice masses, a strong variability exists within very small glaciers [30], which usually show shortest response times to climate forcing [39–41].

Even if the interest for very small glacier has recently grown in the scientific community, there is still a considerable uncertainty about their response to climate. Monitoring the evolution of very small glaciers could provide new insights regarding their fate over longer time-scales, e.g. their disappearance versus transitioning into debris-covered and/or rock glaciers, which may also have implications for catchment hydrology [42–44]. For these reasons, there is a need for improving our knowledge about the behaviour of very small glaciers, for example analysing their recent and historical changes.

In this thesis we studied the Ghiacciaio Occidentale del Montasio (here in after Montasio Glacier), a very small glacier with peculiar characteristics. It is located in the Eastern Italian Alps (Julian Alps), and it is known as the lowermost Italian glacier, with a mean elevation of 1910 m a.l.s., which is extremely below the regional ELA (Equilibrium Line Altitude). It stays in a small niche heavily shaded by the north side of the Mt. Jof di Montasio, which is also an important source of avalanches and rockfalls. The Montasio Glacier is indeed an avalanche fed glacier characterized by a thick debris cover over the ablation zone.

Several aspects make direct surveys on this glacier challenging: *i*) the avalanches and the rock falls represent real hazards; *ii*) the same processes prevent the use of glaciological methods for mass balance determinations; *iii*) the GNSS coverage is usually compromised in the upper part due to the high walls of the Jof di Montasio; and *iv*) the small size of the glacier prevent the use of satellite images that are usually employed over larger glaciers, due to the poor spatial resolution. For these reasons, this glacier is a clear example of a ‘difficult’ study area, but at the same time it is an interesting case study where to test and refine high resolution techniques such as SfM-MVS and laser scanning [45–47].

1.3 High resolution topographic techniques for geodetic mass balance measurements

The availability of remote sensing data is rapidly increasing, also considering that their cost is becoming more affordable. Depending on the platform and the sensor type, both small and very large areas can be monitored with a wide range of spatial resolutions. Especially high-resolution surveys are becoming more and more interesting and employed to study glacier mass changes (Table 1.1- e.g. 48–50). As previously mentioned, some of the most used technologies involve Synthetic Aperture Radar (SAR), laser scanning and photogrammetric surveys.

More in detail, SAR is a class of side-looking radar systems typically mounted on an aircraft or spacecraft. Interferometric SAR (IfSAR or InSAR) uses the parallax (phase shift) in two different SAR images collected at different radar antenna elevation angles to generate a 3D surface with vertical resolution typically at a submetric scale [51]. Since this technology is effective even in absence of light and can penetrate most clouds, it is often applied to estimate glacier mass changes especially at higher latitudes due to the polar night [52–55]. However, the creation of high-quality DEMs is not straightforward and requires a certain level of expertise.

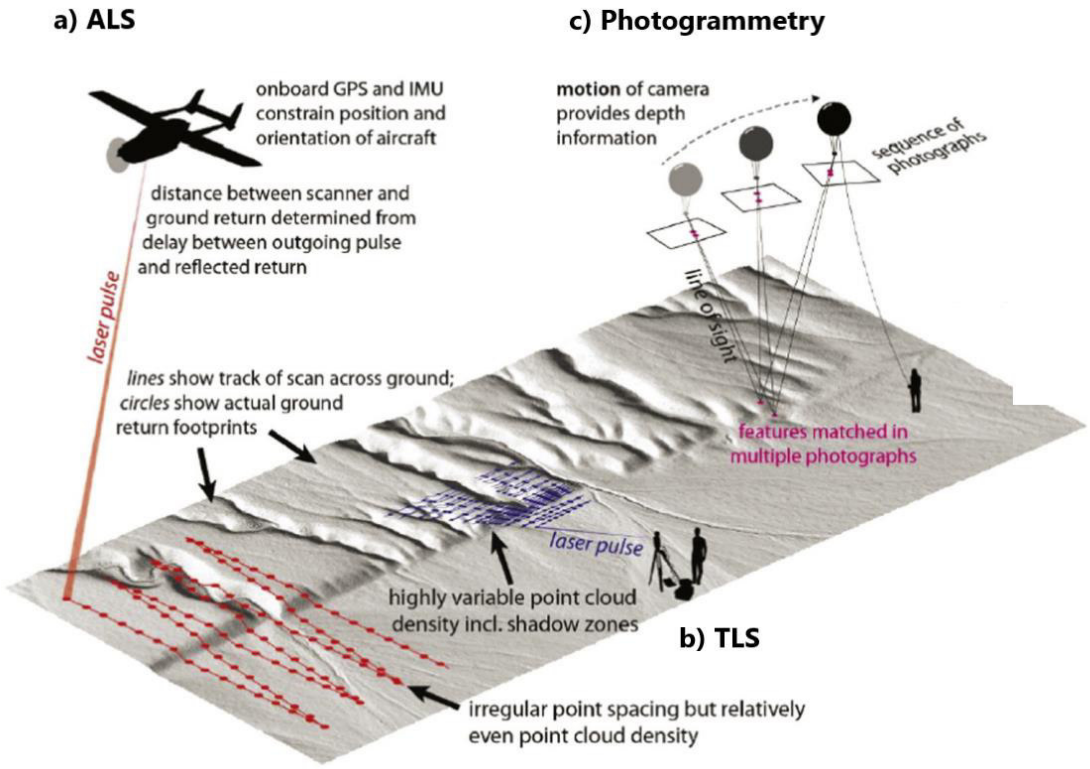

Figure 1.1 *Representation of different raw data acquisition: ALS (a), TLS (b), and SfM (c). Modified from Passalacqua (2015) [51]*

Laser scanners are active sensors which emit laser pulses toward the investigated objects and then record the backscattered radiation [56], thus directly producing a point cloud of the surveyed area. The sensor can be mounted on both ground-based (TLS - Terrestrial Laser Scanner) and airborne (ALS - Aerial Laser Scanner) platforms (Figure 1.1.a and 1.1.b). The former allows to cover a relatively small area based on the position of the TLS, and could require more than one acquisition to cover the entire study area. Moreover, data collection can be time consuming, but the point cloud density can be extremely high, achieving millimetre to centimetre precision. Conversely, ALS can cover vast areas but with slightly lower position accuracy (from a few centimetres to decimetres) and less point density (from 4 to more than 100 points m^{-2}) according the distance from the surfaces. Moreover, it requires the integration of Global Navigate Satellite System (GNSS) and inertial measurement unit (IMU) helicopter data to obtain the georeferenced position of every single point.

Both systems are considered highly precise and accurate and are often used as reference data for quality check of other high-resolution techniques [46].

Photogrammetric surveys reconstruct surface topography based on multiple images acquired from different perspectives (Figure 1.1.c). Depending on the needs, cameras can be mounted on satellites, aircraft, unmanned aerial vehicles (UAV), on tripods or even just carried around manually, allowing a wide range of solutions for both spatial extent and resolution.

For instance, stereo pairs imagery from Very High Resolution (VHR) satellites (e.g., WorldView-2, Pleiades, Geoeye-1) can achieve a pixel resolution below 1 m [51,57,58]. These data can be used to reconstruct glacier DEMs reaching submeter spatial resolution with a vertical accuracy of 0.5 m in the best conditions (Table 1.1); on the other hand, it requires a relatively high level of expertise to process the input data into a high-quality DEM [51].

Aerial images collected from aircrafts (airplanes, helicopters or unmanned aerial vehicles-UAV) are typically processed using SfM-MVS (Structure from Motion / Multi-View Stereo) algorithms, which will be discussed in detail in the following.

Airplanes and helicopters can cover vast areas and they are usually employed to acquire data to produce orthophotos or, if paired with ALS data, vectorized maps. Moreover, in the most recent applications these images have been employed to create digital twins of urban areas.

Drones, instead, are interesting to survey limited areas with an extension that usually do not exceed 1 km^2 for glacial and periglacial studies [59] but they can achieve more than a 15 km^2 survey [60] depending on the drone type (e.g. quadcopter or fixed wing) and characteristics. They are applied to produce orthophotos and high-resolution 3D models which allow to obtain DEMs with a resolution up to 0.05 m px^{-1} depending on the flight heights and the sensor quality. UAVs also improve timing and drastically reduce the costs compared to other approaches. Indeed, they allow to swiftly respond at geomorphic and hydrologic events and access steep or challenging areas where tripod-based surveying may not be possible [51]. Moreover, UAV data acquisition require relatively little training and is extremely inexpensive compared to satellite and aerial imaging acquisition [61].

On the other hand, major drawbacks regard the large errors that may occur if correct flight plans or lens calibration is not performed [62], and the limited extend that can be monitored with a single survey. It is exactly for the great trade-off between pros and cons that UAV-based SfM-MVS technique has been the main method applied in this thesis.

***Table 1.1**. High resolution technique and information reported in Passalacqua (2015)* [51].

Technique	Spatial extent (km^2)	Typical point density (pts/m^2)	Best georeferenced or measurement accuracy (vert/horiz) (m)	Smallest footprint (m)
ALS	10-100s	1-30	0.05/0.2-0.2/0.6	0.2
VHR stereo satellite imagery	100-15.000	0.1-1	0.5/0.5 with GCP >3-5 without GCP	0.5
SfM/MVS Aerial Imagery	0.1-100	1-1000	0.02-0.2 Georegef. set by GCP	0.05
TLS	0.1-10	1000-100.000	0.002-0.01 Georegef. set by GCP	0.003-0.01
rtkGPS	0.1-10	1-10	0.002-0.01 Georegef. set by GCP	0.003-0.01
Theodolite				

1.4 The Structure from Motion- Multi-View Stereo technique

The SfM-MVS technique represents the last evolution of photogrammetry, whose applications have seen a great increase in the last decade even for cryosphere monitoring and geodetic mass balance measurements (e.g. 46,63). Extensive description of SfM-MVS steps and algorithms are described in Carvirrick (2016) [64] and in Remondino (2016) [65] and hereinafter summarised.

The Structure from Motion approach is the first step of SfM-MVS and combines the Bundle Adjustment photogrammetric algorithm with automatic methods from computer vision (e.g., feature

detection algorithms). It allows to obtain automatically, or semi-automatically, 3D information of a photographed object based on a sequence of overlapping images captured even with non-metric cameras. Based on the homologous points found between the images (tie points), SfM applies the Bundle Adjustment algorithm on multiple images to simultaneously estimate the 3D geometry of the studied scene, camera orientation (extrinsic orientation) and calibration parameters (intrinsic orientation).

More in detail, the general SfM workflow starts with the detection of feature points (key points) in each image using, e.g., the "scale-invariant-feature-transformation" (SIFT, CIT [66]) object recognition system or one of its variants, that provides features invariant to rotations, scale changes and partially to illumination changes. SIFT computes for each feature extracted a group of vectors (descriptors), which describe the trend of the gradient in the neighbourhood of the point. Descriptors are then compared to those present in other images to find correspondences using a nearest-neighbour approach. Matched points are filtered to remove outliers and identify geometrically consistent matches. At this stage, valid matching points are available for pairs of images, and the found correspondences have to be propagated to the entire image set identifying the so-called tie points, in order to complete the phase of camera orientation. The obtained tie points are used as input for the Bundle Adjustment algorithm [67] which calculates the orientation of each camera minimising the re-projection error. Ground control points (GCPs) can be introduced in the process, i.e., points identified in the images, whose 3D coordinates are known in advance. They can be used as constraints in the Bundle Adjustment and allow to georeference and scale the resulting 3D model.

The SfM approach, strictly speaking, refers to the process described above and produces a 3D sparse point cloud in which relative distances between all the 3D tie points are consistent. The second component of the SfM-MVS, the Multi-View Stereo algorithms (MVS), is then used to densify the sparse point cloud using as input the collection of images and the corresponding intrinsic and extrinsic camera parameters, previously estimated. The result is a point cloud whose density is at least two orders of magnitude higher than the sparse one [64]. Since it operates at the individual pixel scale, the MVS is the most computationally intense step of the whole 3D reconstruction process [68]. A comprehensive review of high-density image matching algorithms is given in Remondino (2016), Scharstein and Szeliski (2002), Seitz et al. (2006), Remondino et al. (2013) and Ahmadabadian et al. (2013) [65,69–71].

1.5 Workflow for the evaluation of glacier mass balance using SfM-MVS

The SfM-MVS photogrammetric survey finalized at the reconstruction of the geodetic mass balance starts always with the acquisition phase, where aerial (or terrestrial) images and ground control points are collected. The image acquisition step usually requires to set up the UAV-flight plan (or the walking path) based on the needed ground sampling distance (GSD, i.e., the distance between the centres of two adjacent pixels measured on the ground) and image overlapping ratio. GCPs must be distributed homogeneously over the area of interest and their position is measured with a GNSS receiver or other topographic techniques (e.g., a total station). Determining the right amount of GCPs is a critical point to obtain a high-quality product, but there are no *a priori* methods for its estimation since surface morphology and patterns greatly influence this requirement. At the very least, a total of three GCPs is needed to georeference and scale the final model; however, some works suggest to use that no less than four GCPs every 100 photos should be used [72] for achieving sufficient accuracy. Finally, for acquisition over glaciated or snow-covered surfaces, stable cloudy conditions are usually preferred to clear-sky or scattered-cloud conditions, to avoid both sudden changes in light intensity and high contrast between shaded and sun-exposed areas.

The images and the GCPs are then used as input to produce high resolution 3D models. Various SfM-MVS commercial software can be used, for example 3DF Zephyr (www.3dflow.ne), pix4d (www.pix4d.com), MicMac (www.micmac.ensg.eu), PMVS (www.di.ens.fr/pmvs). In this thesis, Photoscan v 1.4.3.6488 and Metashape v 1.6.4.10928 (–Agisoft LLC, St. Petersburg, Russia) software were employed to process the acquired data due to the extremely wide spreads usage in the scientific community. In fact, they have highly automated and user-friendly procedures that result extremely useful during data processing, the cons are that they do not allow to select the MVS algorithms which are *de facto* black boxes for the user. The pipeline adopted in this thesis inside the aforementioned software is described below.

Firstly, a pre-processing step accounts for *i*) the removal of undesired features in the scene via manual image masking (e.g. people, clouds or portion of the sky), *ii*) pre-camera calibration and *iii*) marker identification for subsequent georeferencing. Pre-camera calibration consists in the estimation of the internal parameter of the camera using specific patterns (e.g. chessboard panels). This can minimise “doming” and “bowling” effect in the 3D model which may occur when using self-calibration camera with single-scale nadir imagery, which are particularly common in UAV surveys [73]. The last pre-processing step consists in the marker identification in which a 3D coordinate is assigned to a natural or artificial target within each image. This step can be performed

manually, semi-automatically or automatically. Semi-automatic procedure performs a preliminary image alignment to identify markers based on their local coordinates, while the automatic procedure is able to detect marker positions recognising specific patterns within the images.

After pre-processing, the SfM-MVS algorithms are applied to the image set in the following order: Camera orientation, a first Bundle Adjustment, an iteration of sparse point cloud filtering followed by Bundle Adjustment, and finally the dense cloud calculation. Camera orientation and Bundle Adjustment (which constitute together the standard SfM procedure) correspond to the "align" and "optimization" function in PhotoScan and Metashape. All SfM-MVS steps, except for sparse point cloud filtering, have already been detailed in Chapter 1.4, while the introduction of the sparse point cloud filtering is specific of the pipeline used in this thesis. This step removes tie points which are projected in less than three images, have a reprojection error higher than one pixel reprojection or have high reprojection uncertainty [74]. This process combined with a subsequent refinement via Bundle Adjustment increases the sparse point cloud and the camera orientation accuracy. Removing outliers and incorrect matches from the sparse point cloud is extremely important, in fact the clean process associated with additional cycle of optimization can improve the model accuracy up to an order of magnitude [75].

Finally, the last product of SfM-MVS (the dense point cloud) can be further cleaned, manually or using automatic filters, to remove noisy points before the creation of the final DEM. Various filters were used from different software: SOR filter CloudCompare (v2.9.1, http://www.cloudcompare.org/), TopCat filter in Geomorphic Change Detection plugin [76] or the point cloud decimation tool available in the JRC 3D Reconstructor software (v. 4.3.1, Gexcel, Cagliari, Italy). The cleaned pointcloud is transformed in Triangulated Irregular Network (TIN) and subsequently rasterized. The geodetic mass balance of a glacier can be calculated differencing DEMs of different periods, and converting volume changes to mass changes using estimated snow and ice densities [26]. In each mass balance calculation was used density data obtained in field (e.g. old snow and firn) or from literature (e.g. ice and fresh snow, or density assumption to estimate mass balance over timespan longer than five years) [12,26]. Spatial variability uncertainties were overcome using area-weighted mean density based on the spatial extent of different substrata observed in the two compared years [47].

1.6 Thesis aims and outline

This thesis aims to reconstruct recent and historical behaviour of the lowermost Italian glacier using state of the art, and high-resolution techniques particularly focusing on the application of SfM-MVS.

Firstly, the goodness of the technique was estimated under conditions similar to the Montasio Glacier. The response of the technique was analysed under different scenarios performing consecutive flights over three debris covered easy-to-access riverbeds. The effect on change detection analysis was tested considering different aspects influencing data acquisition and data processing steps. In particular were taken into account *i*) the study area morphology and patterns, *ii*) the camera sensor, *iii*) the number of GCPs, *vi*) the precision of GCPs and *v*) the flight mode (Chapter 2). The purpose was to highlight aspects which must be considered for reducing biases that may lead to wrong evaluations of the phenomena under study. In particular repeatability and reproducibility of SfM-MVS were tested to identify critical points which may affect change detection analyses, such those usually performed for geomorphic change detection on riverbed areas or glacier mass balance monitoring.

The study in Chapter 3 give insight on the Montasio Glacier behaviour during the last two decades using high resolution data mainly derive with SfM-MVS technique. Data were collected between 2006 and 2019 and the recent glacier development was studed via mass balance, horizontal displacements, and vertical displacements evaluation. Glacier response to weather conditions were inspected correlating annual mass balance changes with temperature and precipitation data using Spearman for different time lags (annual, ablation and accumulation seasons). Furthermore, cumulated mass balance of the Montasio Glacier was compared with the ones of the reference glaciers for the European Alps area to identify potentially anomalous behaviour.

Finally, in Chapter 4 we extended the analysis of Chapter 3 until 1920 in order to reconstruct the past behaviour of the glacier and to confirm the role of debris coverage in the current Montasio Glacier dynamics. Historical DEMs were reconstructed starting from several data sources and using different techniques (SfM-MVS, monoplotting and map reconstruction) for the time span 1920-2020. Glacier change analyses were performed similarly to Chapter 3 but were coupled with climatic trend, anomalies, and breakpoint analysis to understand how the glacier reached to its actual behaviour and to try to comprehend its possible future development.

REFERENCES

1. Houghton, J.T., Ding, Y., Griggs, D.J., Noguer, M., van der Linden. P.J., Xiaosu, D. Climate Change 2001: The Scientific Basis. Contribution of Working Group I to the Third Assessment Report of the Intergovernmental Panel on Climate Change. *Cambridge Univ. Press* **2001**, 881, doi:10.1256/004316502320517344.

2. Hock, R.; Huss, M. Glaciers and climate change. In *Climate Change*; Elsevier, 2021; pp. 157–176.

3. Rodell, M.; Famiglietti, J.S.; Wiese, D.N.; Reager, J.T.; Beaudoing, H.K.; Landerer, F.W.; Lo, M.-H. Emerging trends in global freshwater availability. *Nature* **2018**, *557*, 651–659, doi:10.1038/s41586-018-0123-1.

4. Kraaijenbrink, P.D.A.; Bierkens, M.F.P.; Lutz, A.F.; Immerzeel, W.W. Impact of a global temperature rise of 1.5 degrees Celsius on Asia's glaciers. *Nature* **2017**, *549*, 257–260, doi:10.1038/nature23878.

5. Huss, M.; Hock, R. Global-scale hydrological response to future glacier mass loss. *Nat. Clim. Chang.* **2018**, *8*, 135–140, doi:10.1038/s41558-017-0049-x.

6. Marzeion, B.; Jarosch, A.H.; Hofer, M. Past and future sea-level change from the surface mass balance of glaciers. *Cryosph.* **2012**, *6*, 1295–1322, doi:10.5194/tc-6-1295-2012.

7. IPCC *Climate Change 2013: The Physical Science Basis. Contribution of Working Group I to the Fifth Assessment Report of the Intergovernmental Panel on Climate Change*; Stocker, T.F., Qin, D., Plattner, G.-K., Tignor, M., Allen, S.K., Boschung, J., Nauels, A., Xia, Y., Bex, V., Midgley, P.M., Eds.; Cambridge University Press, Cambridge, United Kingdom and New York, NY, USA., 2013; ISBN 978-92-9169-138-8.

8. Zemp, M.; Nussbaumer, S.U.; Gärtner-Roer, I.; Bannwart, J.; Paul, F.; Hoelzle, M. *WGMS 2021. Global Glacier Change Bulletin No. 4 (2018–2019)*; World Glacier Monitoring Service, Zurich, Switzerland;

9. Zemp, M.; Huss, M.; Eckert, N.; Thibert, E.; Paul, F.; Nussbaumer, S.U.; Gärtner-Roer, I. Brief communication: Ad hoc estimation of glacier contributions to sea-level rise from the latest glaciological observations. *Cryosph.* **2020**, *14*, 1043–1050, doi:10.5194/tc-14-1043-2020.

10. Zemp, M.; Huss, M.; Thibert, E.; Eckert, N.; McNabb, R.; Huber, J.; Barandun, M.; Machguth, H.; Nussbaumer, S.U.; Gärtner-Roer, I.; et al. Global glacier mass changes and their contributions to sea-level rise from 1961 to 2016. *Nature* **2019**, *568*, 382–386, doi:10.1038/s41586-019-1071-0.

11. Oerlemans, J. Quantifying Global Warming from the Retreat of Glaciers Author. *Science (80-.).* **1994**, *264*, 243–245.

12. Benn, D.; Evans, D.J.A. *Glaciers and Glaciation, 2nd edition*; Education, H., Ed.; 2nd Editio.; Routledge: London, 2010; ISBN 9781444128390.

13. Østrem, G.; Brugman, M. *Mass Balance Measurements: A Manual for Field and Office Work*; Oslo, 1991;

14. Kaser, G.; Fountain, A.; Jansson, P. *A Manual for Monitoring the Mass Balance of Mountain Glaciers. International Hydrological Program – Technical Developments in Hydrology 59*; UNESCO, Paris, 2003;

15. Hubbard, B.; Glasser, N. *Field Techniques in Glaciology and Glacial Geomorphology*; Wiley, Ed.; Chichester;

16. Zemp, M.; Thibert, E.; Huss, M.; Stumm, D.; Rolstad Denby, C.; Nuth, C.; Nussbaumer, S.U.; Moholdt, G.; Mercer, A.; Mayer, C.; et al. Reanalysing glacier mass balance measurement series. *Cryosph.* **2013**, *7*, 1227–1245, doi:10.5194/tc-7-1227-2013.

17. Cogley, J.G. Methods of Mass Balance Measurements and Modelling. *Geogr. Ann. Ser. A, Phys. Geogr.* **1999**, *81*, 497–507.

18. Fountain, A.G.; Vecchia, A. How many stakes are required to measure the mass balance of a glacier? *Geogr. Ann.* **1999**, *81A*, 563–574.

19. Collins, D.N. Water and mass balance measurements in glacierized drainage basins. *Geogr. Ann.* **1984**, *66A*, 197–214.

20. Ribstein, P.; Titiau, E.; Francou, B.; Saravia, R. Tropical climate and glacier hydrology: a case study in Bolivia. *J. Hydrol.* **1995**, *165*, 221–234.

21. Kaser, G.; Juen, I.; Georgesa, C.; Gómezb, J.; Tamayob, W. The impact of glaciers on the runoff and the reconstruction of mass balance history from hydrological data in the tropical

Cordillera Blanca, Perú. *J. Hydrol.* **2003**, *282*, 130–144.

22. Barry, R.G. *Mountain Weather and Climate, 2nd edition*; 2nd ed.; Routledge: London, 1992;

23. Luthcke, S.B.; Arendt, A.A.; Rowlands, D.D.; McCarthy, J.J.; Larsen, C.F. Recent glacier mass changes in the Gulf of Alaska region from GRACE mascon solutions. *J. Glaciol.* **2008**, *54*, 767–777, doi:10.3189/002214308787779933.

24. Luthcke, S.B.; Zwally, H.J.; Abdalati, W.; Rowlands, D.D.; Ray, R.D.; Nerem, R.S.; Lemoine, F.G.; McCarthy, J.J.; Chinn, D.S. Recent Greenland Ice Mass Loss by Drainage System from Satellite Gravity Observations. *Science (80-.).* **2006**, *314*, 1286–1289, doi:10.1126/science.1130776.

25. Velicogna, I.; Wahr, J. Acceleration of Greenland ice mass loss in spring 2004. *Nature* **2006**, *443*, 329–331, doi:10.1038/nature05168.

26. Huss, M. Density assumptions for converting geodetic glacier volume change to mass change. *Cryosph.* **2013**, *7*, 877–887, doi:10.5194/tc-7-877-2013.

27. Cogley, J.G.; Hock, R.; Rasmussen, L.A.; Arendt, A.A.; Bauder, A.; Braithwaite, R.J.; Jansson, P.; Kaser, G.; Möller, M.; Nicholson, L.; et al. *Glossary of glacier mass balance and related terms, IHP-VII Technical Documents in Hydrology No.86, IACS Contribution No. 2*; UNESCO-IHP, Ed.; Paris, 2011;

28. Fischer, M. Understanding the response of very small glaciers in the Swiss Alps to climate change, University of Fribourg, Fribourg, 2018.

29. Colucci, R.R. Geomorphic influence on small glacier response to post-Little Ice Age climate warming: Julian Alps, Europe. *Earth Surf. Process. Landforms* **2016**, *41*, 1227–1240, doi:10.1002/esp.3908.

30. Huss, M.; Fischer, M. Sensitivity of Very Small Glaciers in the Swiss Alps to Future Climate Change. *Front. Earth Sci.* **2016**, *4*, 1–17, doi:10.3389/feart.2016.00034.

31. Paul, F.; Kääb, A.; Maisch, M.; Kellenberger, T.; Haeberli, W. Rapid disintegration of Alpine glaciers observed with satellite data. *Geophys. Res. Lett.* **2004**, *31*, n/a-n/a, doi:10.1029/2004GL020816.

32. Pfeffer, W.T.; Arendt, A.A.; Bliss, A.; Bolch, T.; Cogley, J.G.; Gardner, A.S.; Hagen, J.O.;

Hock, R.; Kaser, G.; Kienholz, C.; et al. The randolph glacier inventory: A globally complete inventory of glaciers. *J. Glaciol.* **2014**, *60*, 537–552, doi:10.3189/2014JoG13J176.

33. Huss, M. Present and future contribution of glacier storage change to runoff from macroscale drainage basins in Europe. *Water Resour. Res.* **2011**, doi:10.1029/2007WR010299.

34. Jost, G.; Moore, R.D.; Menounos, B.; Wheate, R. Quantifying the contribution of glacier runoff to streamflow in the upper Columbia River Basin, Canada. *Hydrol. Earth Syst. Sci.* **2012**, *16*, 849–860, doi:10.5194/hess-16-849-2012.

35. Barnett, T.P.; Adam, J.C.; Lettenmaier, D.P. Potential impacts of a warming climate on water availability in snow-dominated regions. *Nature* **2005**, *438*, 303–309, doi:10.1038/nature04141.

36. Rangecroft, S.; Harrison, S.; Anderson, K.; Magrath, J.; Castel, A.P.; Pacheco, P. Climate Change and Water Resources in Arid Mountains: An Example from the Bolivian Andes. *Ambio* **2013**, *42*, 852–863, doi:10.1007/s13280-013-0430-6.

37. DeBeer, C.M.; Sharp, M.J. Topographic influences on recent changes of very small glaciers in the Monashee Mountains, British Columbia, Canada. *J. Glaciol.* **2009**, *55*, 691–700, doi:10.3189/002214309789470851.

38. Demuth, M.; Pinard, V.; Pietroniro, A.; Luckman, B.; Hopkinson, C.; Dores, P.; Comeau, L. Recent and past-century variations in the glacier resources of the Canadian Rocky Mountains: Nelson River sys. *Tessa Glacialis* **2008**, *11*, 27–52.

39. Grudd, H. Small Glaciers as Sensitive Indicators of Climatic Fluctuations. *Geogr. Ann. Ser. A, Phys. Geogr.* **1990**, *72*, 119–123, doi:10.1080/04353676.1990.11880305.

40. Nesje, A.; Bakke, J.; Dahl, S.O.; Lie, Ø.; Matthews, J.A. Norwegian mountain glaciers in the past, present and future. *Glob. Planet. Change* **2008**, *60*, 10–27, doi:10.1016/j.gloplacha.2006.08.004.

41. Federici, P.R.; Pappalardo, M. Glacier retreat in the maritime alps area. *Geogr. Ann. Ser. A, Phys. Geogr.* **2010**, *92*, 361–373, doi:10.1111/j.1468-0459.2010.00401.x.

42. Leigh, J.R.; Stokes, C.R.; Carr, R.J.; Evans, I.S.; Andreassen, L.M.; Evans, D.J.A. Identifying and mapping very small (<0.5 km 2) mountain glaciers on coarse to high-resolution imagery. *J. Glaciol.* **2019**, *65*, 873–888, doi:10.1017/jog.2019.50.

43. Capt, M.; Bosson, J.-B.; Fischer, M.; Micheletti, N.; Lambiel, C. Decadal evolution of a very small heavily debris-covered glacier in an Alpine permafrost environment. *J. Glaciol.* **2016**, *62*, 535–551, doi:10.1017/jog.2016.56.

44. Jones, D.B.; Harrison, S.; Anderson, K.; Whalley, W.B. Rock glaciers and mountain hydrology: A review. *Earth-Science Rev.* **2019**, *193*, 66–90, doi:10.1016/j.earscirev.2019.04.001.

45. Carturan, L.; Baldassi, G.A.; Bondesan, A.; Calligaro, S.; Carton, A.; Cazorzi, F.; Dalla fontana, G.; Francese, R.; Guarnieri, A.; Milan, N.; et al. Current behaviour and dynamics of the lowermost italian glacier (montasio occidentale, julian alps). *Geogr. Ann. Ser. A, Phys. Geogr.* **2013**, *95*, 79–96, doi:10.1111/geoa.12002.

46. Piermattei, L.; Carturan, L.; Guarnieri, A. Use of terrestrial photogrammetry based on structure-from-motion for mass balance estimation of a small glacier in the Italian alps. *Earth Surf. Process. Landforms* **2015**, *40*, 1791–1802, doi:10.1002/esp.3756.

47. De Marco, J.; Carturan, L.; Piermattei, L.; Cucchiaro, S.; Moro, D.; Dalla Fontana, G.; Cazorzi, F. Minor Imbalance of the Lowermost Italian Glacier from 2006 to 2019. *Water* **2020**, *12*, 2503, doi:10.3390/w12092503.

48. Fischer, A.; Schwaizer, G.; Seiser, B.; Helfricht, K.; Stocker-Waldhuber, M. High-resolution inventory to capture glacier disintegration in the Austrian Silvretta. *Cryosph.* **2021**, *15*, 4637–4654, doi:10.5194/tc-15-4637-2021.

49. Denzinger, F.; Machguth, H.; Barandun, M.; Berthier, E.; Girod, L.; Kronenberg, M.; Usubaliev, R.; Hoelzle, M. Geodetic mass balance of Abramov Glacier from 1975 to 2015. *J. Glaciol.* **2021**, *67*, 331–342, doi:10.1017/jog.2020.108.

50. Cao, B.; Guan, W.; Li, K.; Pan, B.; Sun, X. High-Resolution Monitoring of Glacier Mass Balance and Dynamics with Unmanned Aerial Vehicles on the Ningchan No. 1 Glacier in the Qilian Mountains, China. *Remote Sens.* **2021**, *13*, 2735, doi:10.3390/rs13142735.

51. Passalacqua, P.; Belmont, P.; Staley, D.M.; Simley, J.D.; Arrowsmith, J.R.; Bode, C.A.; Crosby, C.; DeLong, S.B.; Glenn, N.F.; Kelly, S.A.; et al. Analyzing high resolution topography for advancing the understanding of mass and energy transfer through landscapes: A review. *Earth-Science Rev.* **2015**, *148*, 174–193, doi:10.1016/j.earscirev.2015.05.012.

52. Engeset, R. V.; Kohler, J.; Melvold, K.; Lundén, B. Change detection and monitoring of glacier mass balance and facies using ERS SAR winter images over Svalbard. *Int. J. Remote Sens.* **2002**, *23*, 2023–2050, doi:10.1080/01431160110075550.

53. Winsvold, S.H.; Kääb, A.; Nuth, C.; Andreassen, L.M.; van Pelt, W.J.J.; Schellenberger, T. Using SAR satellite data time series for regional glacier mapping. *Cryosph.* **2018**, *12*, 867–890, doi:10.5194/tc-12-867-2018.

54. Samsonov, S.; Tiampo, K.; Cassotto, R. SAR-derived flow velocity and its link to glacier surface elevation change and mass balance. *Remote Sens. Environ.* **2021**, *258*, 112343, doi:10.1016/j.rse.2021.112343.

55. Schellenberger, T.; Dunse, T.; Kääb, A.; Kohler, J.; Reijmer, C.H. Surface speed and frontal ablation of Kronebreen and Kongsbreen, NW Svalbard, from SAR offset tracking. *Cryosph.* **2015**, *9*, 2339–2355, doi:10.5194/tc-9-2339-2015.

56. Crosilla, F.; Beinat, A.; Fusiello, A.; Maset, E.; Visintini, D. Basics of Terrestrial Laser Scanning. In; 2019; pp. 87–97.

57. Fieber, K.D.; Mills, J.P.; Miller, P.E.; Clarke, L.; Ireland, L.; Fox, A.J. Rigorous 3D change determination in Antarctic Peninsula glaciers from stereo WorldView-2 and archival aerial imagery. *Remote Sens. Environ.* **2018**, *205*, 18–31, doi:10.1016/j.rse.2017.10.042.

58. Shean, D.E.; Bhushan, S.; Montesano, P.; Rounce, D.R.; Arendt, A.; Osmanoglu, B. A Systematic, Regional Assessment of High Mountain Asia Glacier Mass Balance. *Front. Earth Sci.* **2020**, *7*, doi:10.3389/feart.2019.00363.

59. Śledź, S.; Ewertowski, M.W.; Piekarczyk, J. Applications of unmanned aerial vehicle (UAV) surveys and Structure from Motion photogrammetry in glacial and periglacial geomorphology. *Geomorphology* **2021**, *378*, 107620, doi:10.1016/j.geomorph.2021.107620.

60. Dąbski, M.; Zmarz, A.; Rodzewicz, M.; Korczak-Abshire, M.; Karsznia, I.; Lach, K.; Rachlewicz, G.; Chwedorzewska, K. Mapping Glacier Forelands Based on UAV BVLOS Operation in Antarctica. *Remote Sens.* **2020**, *12*, 630, doi:10.3390/rs12040630.

61. Fonstad, M.A.; Dietrich, J.T.; Courville, B.C.; Jensen, J.L.; Carbonneau, P.E. Topographic structure from motion : a new development in photogrammetric measurement. **2013**, *430*, 421–430, doi:10.1002/esp.3366.

62. James, M.R.; Robson, S. Mitigating systematic error in topographic models derived from UAV and ground-based image networks. *Earth Surf. Process. Landforms* **2014**, *39*, 1413–1420, doi:10.1002/esp.3609.

63. Piermattei, L.; Carturan, L.; De Blasi, F.; Tarolli, P.; Dalla Fontana, G.; Vettore, A.; Pfeifer, N. Suitability of ground-based SfM-MVS for monitoring glacial and periglacial processes. *Earth Surf. Dyn.* **2016**, *4*, 425–443, doi:10.5194/esurf-4-425-2016.

64. Carrivick, J.L.; Smith, M.W.; Quincey, D.J. *Structure from Motion in the Geosciences*; John Wiley & Sons, Ltd: Chichester, UK, 2016; ISBN 9781118895818.

65. Remondino, F.; Spera, M.G.; Nocerino, E.; Menna, F.; Nex, F. State of the art in high density image matching. *Photogramm. Rec.* **2014**, *29*, 144–166, doi:10.1111/phor.12063.

66. Lowe, D.G. Distinctive Image Features from Scale-Invariant Keypoints. *Int. J. Comput. Vis.* **2004**, *60*, 91–110, doi:10.1023/B:VISI.0000029664.99615.94.

67. Triggs, B.; McLauchlan, P.F.; Hartley, R.I.; Fitzgibbon, A.W. Bundle Adjustment — A Modern Synthesis. In *Vision Algorithms: Theory and Practice*; Triggs, B., Zisserman, A., Szeliski, R., Eds.; IWVA 1999. Lecture Notes in Computer Science, vol 1883. Springer Berlin Heidelberg: Berlin, Heidelberg, 2000; pp. 298-372. doi: 10.1007/3-540-44480–7_21.

68. Seitz, S.M.; Curless, B.; Diebel, J.; Scharstein, D.; Szeliski, R. A comparison and evaluation of multi-view stereo reconstruction algorithms. In Computer vision and pattern recognition. In Proceedings of the IEEE Computer Society Conference; 2006.

69. Scharstein, D.; Szeliski, R. A taxonomy and evaluation of dense two-frame stereo correspondence algorithms. International journal of computer vision. **2002**.

70. Remondino, F.; Menna, F.; Koutsoudis, A.; Chamzas, C.; El-Hakim, S. Design and implement a reality-based 3D digitisation and modelling project. *Proc. Digit. Herit. Int. Congr.* **2013**, doi:978-1-4799-3169-9/13/$31.00.

71. Ahmadabadian, A.H.; Robson, S.; Boehm, J.; Shortis, M.; Wenzel, K.; Fritsch, D. A comparison of dense matching algorithms for scaled surface reconstruction using stereo camera rigs. *ISPRS J. Photogramm. Remote Sens.* **2013**, *78*, 157–167, doi:10.1016/j.isprsjprs.2013.01.015.

72. Sanz-Ablanedo, E.; Chandler, J.; Rodríguez-Pérez, J.; Ordóñez, C. Accuracy of Unmanned

Aerial Vehicle (UAV) and SfM Photogrammetry Survey as a Function of the Number and Location of Ground Control Points Used. *Remote Sens.* **2018**, *10*, 1606, doi:10.3390/rs10101606.

73. Griffiths, D.; Burningham, H. Comparison of pre- and self-calibrated camera calibration models for UAS-derived nadir imagery for a SfM application. *Prog. Phys. Geogr. Earth Environ.* **2019**, *43*, 215–235, doi:10.1177/0309133318788964.

74. James, M.R. *SfM-MVS PhotoScan image processing exercise*; 2017;

75. Javernick, L.; Brasington, J.; Caruso, B. Modeling the topography of shallow braided rivers using Structure-from-Motion photogrammetry. *Geomorphology* **2014**, *213*, 166–182, doi:10.1016/j.geomorph.2014.01.006.

76. Wheaton, J.M.; Brasington, J.; Darby, S.E.; Sear, D.A. Accounting for uncertainty in DEMs from repeat topographic surveys: Improved sediment budgets. *Earth Surf. Process. Landforms* **2010**, *35*, 136–156, doi:10.1002/esp.1886.

Chapter 2

Assessing Repeatability and Reproducibility of Structure-from-Motion Photogrammetry for 3D Terrain Mapping of Riverbeds

Jessica De Marco [1,2,†], Eleonora Maset [1,†], Sara Cucchiaro [1,*], Alberto Beinat [3] and Federico Cazorzi[1]

[1] Department of Agricultural, Food, Environmental and Animal Sciences (DI4A), University of Udine, Via Delle Scienze, 206, 33100 Udine, Italy;

[2] Department of Life Sciences, University of Trieste (DSV), Via E. Weiss, 2, 34128 Trieste, Italy

[3] Polytechnic Department of Engineering and Architecture (DPIA), University of Udine, Via Delle Scienze, 206, 33100 Udine, Italy;

* Corresponding author

† These authors contributed equally to this work.

Published as: De Marco, J.; Maset, E.; Cucchiaro, S.; Beinat, A.; Cazorzi, F. Assessing Repeatability and Reproducibility of Structure-from-Motion Photogrammetry for 3D Terrain Mapping of Riverbeds. *Remote Sens.* **2021**, *13*, 2572. https://doi.org/10.3390/rs13132572

2 Assessing Repeatability and Reproducibility of Structure-from-Motion Photogrammetry for 3D Terrain Mapping of Riverbeds

2.1 Abstract

Structure-from-Motion (SfM) photogrammetry is increasingly employed in geomorphological applications for change detection, but repeatability and reproducibility of this methodology are still insufficiently documented. This work aims to evaluate the influence of different survey acquisition and processing conditions, including the camera used for image collection, the number of Ground Control Points (GCPs) employed during Bundle Adjustment, GCP coordinate precision and Unmanned Aerial Vehicle flight mode. The investigation was carried out over three fluvial study areas characterized by distinct morphology, performing multiple flights consecutively and assessing possible differences among the resulting 3D models. We evaluated both residuals on check points and discrepancies between dense point clouds. Analyzing these metrics, we noticed high repeatability (Root Mean Square of signed cloud-to-cloud distances less than 2.1 cm) for surveys carried out under the same conditions. By varying the camera used, instead, contrasting results were obtained that appear to depend on the study site characteristics. In particular, lower reproducibility was highlighted for the surveys involving an area characterized by flat topography and homogeneous texturing. Moreover, this study confirms the importance of the number of GCPs entering in the processing workflow, with different impact depending on the camera used for the survey.

Keywords: SfM; point cloud; precision; repeatability; reproducibility; UAV; multi-temporal surveys

2.2 Introduction

Every measurement process, with any technology, is always affected by errors, which, if not properly considered, lead to inevitable biased or wrong evaluations of the phenomenon under study. This problem is particularly relevant in the context of Change Detection (CD), which aims at recognizing differences in the state of an object over time [1,2], allowing to quantify, e.g., the effects of natural or anthropogenic events on the environment morphology. Initially based only on 2D images, in the last decades, CD has been witnessing a revolution thanks to the increasing availability of very high resolution (VHR) 3D data, provided by efficient remote sensing techniques, such as photogrammetry, Light Detection and Ranging (LiDAR) or Interferometric Synthetic Aperture Radar (InSAR). Among them, Structure-from-Motion (SfM) photogrammetry coupled with the use of Unmanned Aerial Vehicles (also known as Uncrewed Aerial Vehicles—UAVs) proved to be one of the most efficient,

cost-effective technologies to generate high-quality surface reconstruction of a variety of environments [3,4].

Born from the combination of photogrammetric principles and computer vision algorithms, SfM is extensively employed for geomorphological applications, ranging from landslide [5,6] and glacier monitoring [7,8] to river channel morphology inspection [9,10] or archaeology 3D reconstructions [11,12], just to name a few. The growing use of this technique is due to several factors, including cost-effectiveness, high temporal frequency of the surveys, ease of use and automation of data processing [13]. Generating a 3D model of an area to capture its state at a certain time is often considered a simple task, that apparently requires only off-the-shelf instruments (i.e., commercial drones, consumer-grade cameras and fully automated photogrammetric software) and little training. However, to reliably detect and quantify temporal surface changes avoiding false positives [14], a deep knowledge of the data processing steps and of the uncertainties affecting the model is mandatory. To this end, several papers in the literature compared the SfM results with other VHR acquisition techniques, such as terrestrial or airborne laser scanning [3,15], or evaluated SfM accuracy on a discrete set of points, whose coordinates are measured through Global Navigation Satellite System (GNSS) [16,17]. These experiments showed centimeter to decimeter discrepancies of the SfM technique versus the compared technologies, depending on survey parameters (e.g., flight design, camera characteristics and georeferencing strategies). Moreover, some works highlighted also a dependency on the photogrammetic software used in image processing [10,18,19]. Comparing SfM results with regard to other (possibly more accurate) surveying techniques can provide an estimate of measurement accuracy and potential systematic errors, but it is not able to capture precision and repeatability [20]. The latter are fundamental aspects to quantify digital elevation model (DEM) uncertainties, which significantly affect surface change detection.

Two main approaches can be employed to estimate the precision of SfM photogrammetry. In recent years, the numerical method proposed in [21] has found extensive spread in geomorphology. It is based on Monte Carlo simulations to generate precision maps, i.e., repeated bundle adjustments are performed to evaluate the spatial variability of precision, which is influenced by photogrammetric and georeferencing conditions. This valuable tool enables the analytical assessment of error distribution for a specific survey, thus allowing to estimate the confidence intervals for detecting surface changes. However, the aforementioned simulation procedure could potentially neglect some influencing factors [20], leading to optimistic results [22]. The alternative approach is represented by the comparison of repeated surveys of the same area, performed under the same conditions during periods when no surface changes occur [20,23]. Although time-consuming, this methodology can

give a comprehensive insight into the features that affect the spatial variation of precision provided by SfM photogrammetry.

Leveraging on repeated UAV surveys, in this work, we perform an extensive evaluation of SfM repeatability, defined as the variation that can be expected when surveying the same area under similar conditions (i.e., same camera, flight path, illumination conditions) within a short time interval [20,24]. Moreover, we investigate SfM reproducibility, meaning measurement variation under different conditions, by performing image acquisitions with different cameras and UAVs. In the literature, several researches demonstrate the role of GCPs on accuracy and precision of DEMs derived from SfM photogrammetry [16,23,25]. In this study, the influence of GCPs is analyzed on the one hand using different number of GCPs, and, on the other hand, exploiting 3D ground coordinates characterized by different precision. Finally, different field sites are considered, in order to evaluate how the topographic characteristics of monitored surfaces can influence the survey precision.

2.3 Materials and Methods

2.3.1 Study Areas

Three reaches (Figure 2.1a,b) located in Friuli Venezia Giulia region (North-east Italy) were selected as study areas due to their different geomorphological characteristics The first site (Palar-P) comprises 0.50 ha of the Palar Torrent (Figure 2.1c-46°18′31.15″N, 13°3′11.03″E) and it is mainly characterised by gentle slope bed (0.5%) with homogeneous small granulometry (Figure 2.1d). The second area (Vegliato-V) covers 0.41 ha of the Vegliato Torrent (Figure 2.1e-46°17′15.50″N, 13°8′47.95″E). This site shows more heterogeneous morphologies due to the presence of torrent control works (i.e., three check dams), river banks and fluvial terraces (Figure 2.1f) and the reach has a slope of 16%. The third study site (Moscardo-M) is located within the Moscardo catchment (Figure 2.1g-46°33′50.53″N, 13°0′43.60″E) and has an extension of 0.12 ha with a slope of 12%. This last one presents high heterogeneity in terms of roughness pattern and granulometry, with size ranging from sand to gigantic boulders, as shown in Figure 2.1h. This is mainly due to debris-flow events which reach very frequently the study area [26]. These particular events influence the reach morphology and cause the presence of different sediment size, from clay particles to boulders (diameter > 1 m).

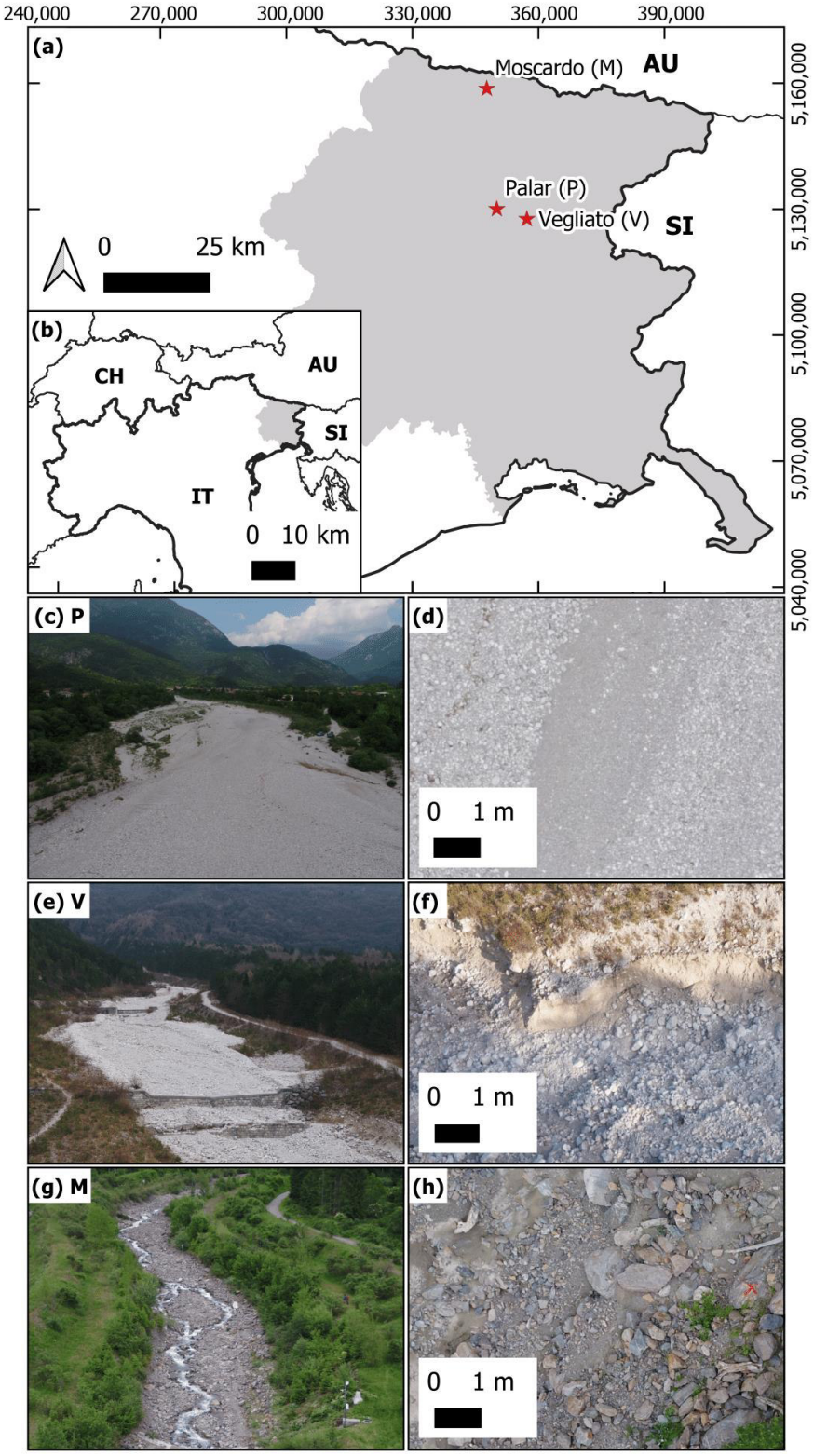

Figure 2.1 *(**a,b**) Geographic location of the study areas, (**c,d**) Palar study area and a detail of the grain size in the riverbed, (**e,f**) Vegliato area and a portion of the fluvial terraces, (**g,h**) Moscardo site and a detail of the heterogeneous granulomerty in the channel reach.*

2.3.2 Data Acquisition

Image data collection over the three study areas was carried out with two different cameras, whose characteristics are reported in Table 2.1.

Table 2.1 *Characteristics of the cameras employed for the surveys.*

Sensor Model	Company	Resolution [MP]	Sensor Dimension [mm]	Focal Length [mm]	Image Resolution [px]
α5000	SONY	20.0	15.4 × 23.2	20	5456 × 3632
X5S	DJI	20.8	17.3 × 13	25	5280 × 3956

Two different UAVs were used, each allowing different flight modes: (i) DJI Matrice210v2 quadcopter, which enables planned flight mode; and (ii) Neutech Airvision NT-4C octorotor (manual flight). The X5S camera is natively installed on the DJI Matrice210v2 quadcopter, while the Sony camera was attached to the gimbal holder using a dedicated aluminum bar specifically crafted. The same Sony camera was attached to the NT-4C octorotor using a two axis gimbal. The installations were made assuring the camera stability along with an elastic suppression of vibrations.

Nadir images were collected with an optimal overlap of 80% in flight direction and an overlap between adjacent flight-lines of 70%. All UAV surveys performed in the same day were conducted consecutively with an interval of at most 5 min, in order to guarantee the same illumination conditions. Features characterizing each survey are reported in Table 2.2.

Table 2.2 *Details of data acquisition. Study site: P = Palar; V = Vegliato; M = Moscardo. Camera: S = Sony α5000; X = X5S. Drone: MT = Matrice, NT4 = NT-4C. Flight mode: Mnl = Manual, Pln = Planned. The last four columns report the number of acquired images (Images), the number of Ground Control Points (GCPs) used in the Bundle Adjustment process, the number of Control Points (CPs) considered for results evaluation purposes and the design Ground Sampling Distance (GSD), respectively.*

Study Site	Camera	Dataset	Date	Drone	Flight Mode	Flight Altitude [m a.g.l.]	Images	GCPs	CPs	GSD [mm/px]
P	S	*P_S1*	13 June 2020	NT4	Mnl	25	167	15	17	7
	S	*P_S2*	13 June 2020	NT4	Mnl	25	150	15	17	7
	X	*P_X1*	13 June 2020	MT	Pln	25	161	15	17	5
	X	*P_X2*	13 June 2020	MT	Pln	25	169	15	17	5
V	S	*V_S1_2019*	16 December 2019	NT4	Mnl	35	217	15	15	10
	S	*V_S2_2019*	16 December 2019	NT4	Mnl	35	167	15	15	10
	S	*V_S1*	17 December 2020	MT	Pln	35	281	15	16	10
	S	*V_S2*	17 December 2020	MT	Pln	35	285	15	16	10
	X	*V_X1*	17 December 2020	MT	Pln	35	191	15	16	8
	X	*V_X2*	17 December 2020	MT	Pln	35	191	15	16	8
M	S	*M_S1*	10 June 2019	NT4	Mnl	25	155	14	12	7
	S	*M_S2*	10 June 2019	NT4	Mnl	25	142	14	12	7
	X	*M_X1*	12 June 2020	MT	Pln	25	197	15	14	5
	X	*M_X2*	12 June 2020	MT	Pln	25	199	15	14	5

In all study areas, Ground Control Points (GCPs) and Check Points (CPs) were measured with a geodetic class GNSS receiver (GS07, Leica, Heerbrugg, Switzerland) set to collect GPS (C/A, L2C, Z track on P2 codes, L1 and L2 phases), Glonass (C/A, P2 codes, L1C and L2P phases) and Galileo (E1, E5b codes and L1, L7 phases) signal observables. This ensured good satellite geometry conditions, in terms of low Dilution of Precision (DOP) parameters, also in the presence of significant sky obstructions. The GCP surveys were carried out in stop&go Post-Processed Kinematic (PPK) mode, paying attention to avoid complete losses of lock of the signal while moving around in the field, in order to guarantee an uninterrupted kinematic session linking the various GCPs. Point positions were also collected in Network Real-Time Kinematic (NRTK) mode for comparison and as a real time prediction of the achieved accuracy, while acquiring raw observations of codes and phases of visible satellites for post-processing purposes.

For every GCP the occupation time lasted from 45 to 150 s, with the antenna pole kept stable by an adjustable bipod, in order to obtain a 3D estimated precision better than 1 cm. The selected reference system for the datasets was RDN2008/UTM zone 33 (EPSG:6708). Both GCPs and CPs were uniformly distributed inside the study areas to prevent and mitigate systematic errors in the photogrammetric model [27].

2.3.3 Data Processing

In order to generate a 3D model for each survey, the Structure-from-Motion algorithm implemented in the Metashape software (v 1.6.4 build 10928, Agisoft LLC, St. Petersburg, Russia) was applied to process each set of collected images, simultaneously estimating exterior orientation parameters and camera calibration. In fact, no information related to interior parameters were available, and self-calibration was performed to compute, for each survey, focal length f, principal point position (c_x,c_y), affinity (b_1), non-orthogonality (b_2), radial (k_1,k_2,k_3,k_4) and tangential distortion parameters (p_1,p_2). The estimated SfM solution was then refined (and georeferenced) exploiting the surveyed GCPs, that were used as constraints in the final bundle adjustment step. The number of GCPs employed for each image set is shown in Table 2.2. GNSS raw data were processed in PPK mode using the Leica GeoOffice software (LGO v 8.4, Leica Geosystems, Switzerland) referring measures to a nearby Continuously Operating Reference Station (CORS), ZUOF, for the Moscardo site and to a virtual reference station inside the study area for the Vegliato and Palar cases. The reference station data were provided in RINEX format from the GNSS networks services operating in the Friuli Venezia Giulia Region (FVG Marussi, INOGS FredNet and HxGN SmartNet). In this way, the final GCP coordinates were estimated based primarily on the PPK solutions, obtaining GCP positions with

accuracy and precision of approximately 10 mm, significantly more reliable than those obtained in NRTK. We therefore used this value to set the "marker accuracy" parameter in Metashape, in order to assign proper weights to the GCP observations in the bundle adjustment [25].

A dense point cloud was then generated via the Multi-View Stereo algorithm of Metashape, exploiting the half-resolution version of the original images and applying mild filtering to remove noisy points. Furthermore, vegetation and wet surfaces were manually removed from the obtained dense point cloud to avoid biased results in the final comparisons.

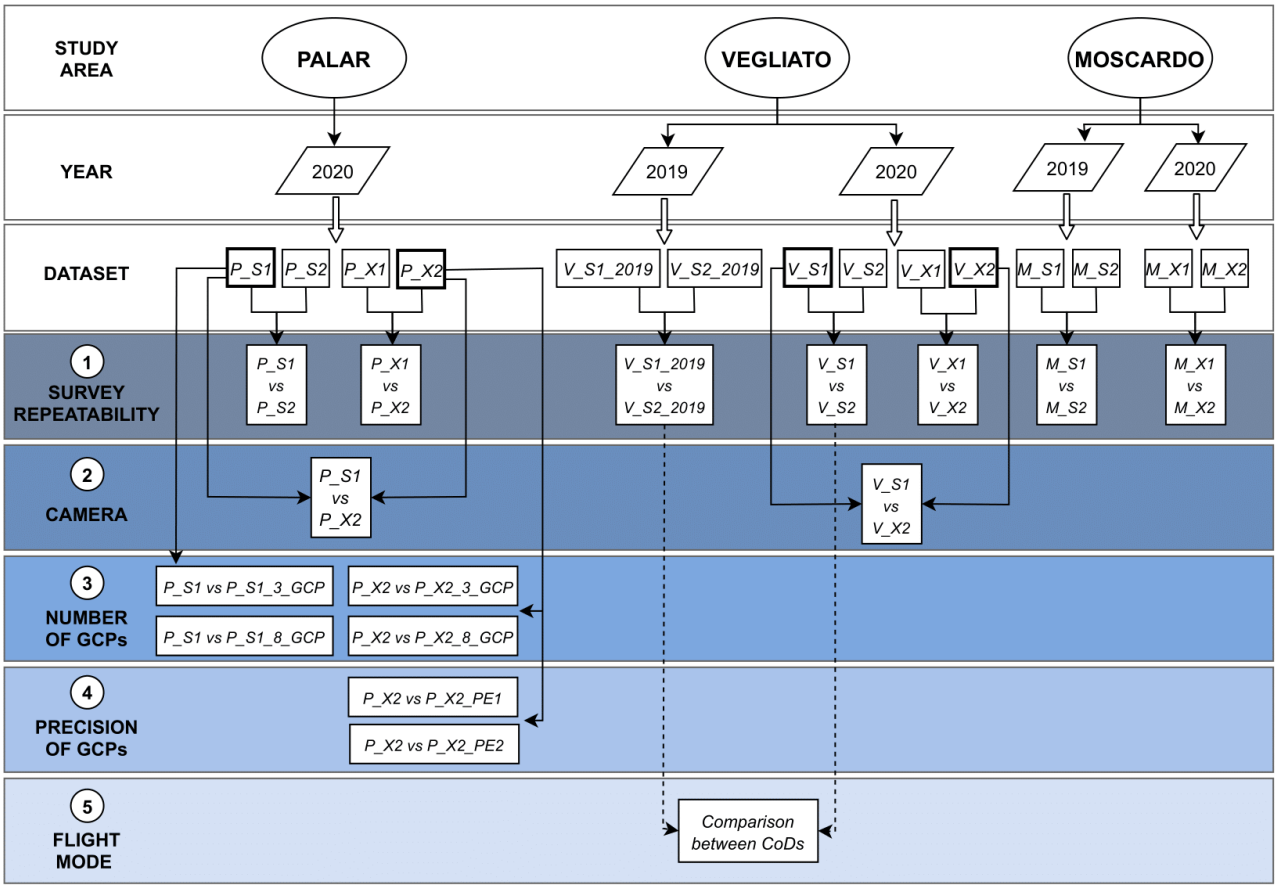

Figure 2.2 *Comparisons performed for the three study areas between consecutive surveys to test survey repeatability (1), different cameras (2), various number of GCPs employed in the bundle adjustment (3), different 3D coordinate precision of GCPs (4) and two flight modes (5). The comparisons are labelled according to the names of the used datasets. The dataset characteristics are reported in Table 2.2.*

For each study site, distances between point clouds generated from different image sets were computed using the M3C2 distance plugin (Multiscale Model to Model Cloud Comparison) [28] available in the Cloud Compare software (v. 2.9.1, GPL software, retrieved from http://www.cloudcompare.org, (accessed on 19 January 2021)). For each pair of compared clouds, the resulted CoD (Cloud of Difference) was rasterized at 0.02 m grid resolution for statistical analysis

and visualisation purposes. Surveys performed on the same day over the same study area were conducted consecutively within short time intervals; therefore, no surface changes occurred during data collection. Distances highlighted by the cloud-to-cloud comparisons can thus be ascribed to differences arising during the photogrammetric pipeline (including image collection). Figure 2.2 illustrates the analyses carried out for each study area.

As already mentioned in Section 2.2, survey repeatability was tested comparing the results provided by two data acquisitions performed consecutively with the same camera. Moreover, for the Palar and Vegliato areas, the SfM reproducibility was assessed based on repeated data collection with two distinct cameras (within short time interval) and analyzing the differences between the derived point clouds (Figure 2.2—block 2).

The effects of GCPs on the precision of the final model were instead evaluated choosing the Palar area as study case. In fact, due to its flat topography and homogeneous texture, this site potentially represents the most challenging scenario for SfM reconstruction, where the benefits provided by the use of GCPs could be more relevant. In particular, one image set acquired with the α5000 Sony camera and one collected with the Zenmuse X5S were considered and processed from scratch using two subsets of GCPs in the bundle adjustment (3 and 8 GCPs, respectively). The resulting point clouds (P_S1_3_GCP and P_S1_8_GCP for the Sony camera; P_X2_3_GCP and P_X2_8_GCP for the X5S camera) were compared with the corresponding reference ones (P_S1 and P_X2, respectively) obtained with 15 GCPs (Figure 2.2-block 3). The photogrammetric model can be influenced not only by the number of GCPs introduced as constraints in the bundle adjustment, but also by the GCP coordinate precision. To test this aspect, we synthetically generated two more cases for the P_X2 dataset, in which the GNSS coordinates of the 15 GCPs were perturbed by adding random Gaussian noise of zero mean and standard deviation σ. In the first one (P_X2_PE1), σ_{xy}=1 cm and σ_z=2 cm were employed for the planimetric and altimetric components, respectively, while in the latter (P_X2_PE2) σ_{xy}=2 cm and σ_z=4 cm were selected (Figure 2.2-block 4).

Finally, the impact of UAV flight mode was analyzed for the Vegliato study area comparing two CoDs resulting from the surveys conducted in 2019 and 2020 (Figure 2.2-block 5). The models and the corresponding CoDs were derived from datasets acquired with the same camera (Sony) and at the same flight altitude (35 m agl). However, the 2019 surveys (dubbed V_S1_2019 and V_S2_2019) were performed with the NT-4C octorotor in manual flight mode, whereas the images acquired in 2020 were captured using the planned flight mode provided by the DJI Matrice210v2 quadcopter. We highlight that, for this test, only an indirect analysis on the CoDs was possible. In fact, a direct

comparison between models deriving from different flight modes was impractical due to surface changes that occurred between the 2019 and 2020 data collections.

2.4 Results

Hereinafter, the results for each dataset and the comparisons among the obtained models are reported in detail. Table 2.3 summarizes the computed camera parameter values, that were estimated via self-calibration as previously described. It is possible to notice the variability of the focal length f estimated for consecutive surveys performed with the same camera, that reaches 74 pixels (1.7%) for the X5S datasets over the Palar area. We reported also the mean GSD computed for each image set after the SfM process. This can differ from the nominal value (Table 2.2) for two main reasons. Image acquisitions with the NT-4C octorotor, in fact, were performed in manual flight mode, which made it difficult to meet the design flight altitude. For the planned flights, instead, a constant altitude (above see level) had to be set in the UAV control unit, preventing the design flight altitude (above ground level) from being respected for the whole surveyed area.

Table 2.3 *Estimated camera parameter values for all datasets. In the last column the actual mean GSD is reported, computed after the image orientation stage.*

Study Site	Dataset	f [px]	c_x [px]	c_y [px]	b_1 [–]	b_2 [–]	k_1 [$\cdot 10^{-2}$]	k_2 [$\cdot 10^{-2}$]	k_3 [$\cdot 10^{-2}$]	k_4 [$\cdot 10^{-2}$]	p_1 [$\cdot 10^{-3}$]	p_2 [$\cdot 10^{-3}$]	Reprj. err. [px]	GSD [mm/px]
P	*P_S1*	4780.6	−24.0	2.7	−0.28	−0.23	−15.2	11.4	5.1	−3.6	−0.8	0.7	0.66	9
	P_S1_8_GCP	4791.4	−24.0	2.5	−0.28	−0.19	−15.2	11.6	5.1	−3.6	−0.8	0.7	0.67	9
	P_S1_3_GCP	4791.2	−24.0	2.5	−0.28	−0.19	−15.2	11.6	5.1	−3.6	−0.8	0.7	0.67	9
	P_S2	4818.8	−24.2	0.3	−0.28	0.83	−15.5	11.7	5.6	−3.7	−0.2	1.2	0.72	10
	P_X1	4459.0	46.7	18.9	−6.66	0.3	0.6	−4.5	12.9	−10.9	2.3	1.0	0.85	5
	P_X2	4385.1	50.4	18.9	−6.93	0.44	0.5	−3.9	10.9	−9.1	2.2	0.9	0.82	5
	P_X2_8_GCP	4378.1	49.8	18.9	−7.31	0.46	0.6	−4.5	12.4	−10.3	2.2	0.9	0.76	5
	P_X2_3_GCP	4383.5	49.6	18.8	−7.42	0.46	0.8	−4.5	12.6	−10.5	2.2	0.9	0.76	5
	P_X2_PE1	4396.9	49.3	18.7	−7.42	0.48	0.6	−4.5	12.7	−10.6	2.2	0.9	0.76	5
	P_X2_PE2	4400.5	49.2	18.6	−7.42	0.48	0.6	−4.6	12.8	−10.7	2.2	0.9	0.76	5
V	*V_S1_2019*	4814.8	−12.6	3.9	−0.28	1.08	−15.8	13.3	1.6	0.1	−0.7	1.1	0.70	7
	V_S2_2019	4809.9	−11.2	3.4	−0.28	0.27	−15.4	11.4	7.1	−5.7	−0.4	1.5	0.69	8
	V_S1	4801.7	−25.6	7.3	−0.28	−0.33	−15.4	11.3	6.8	−5.3	−0.6	1.1	0.69	7
	V_S2	4781.6	−33.7	−19.8	−0.28	0.83	−15.2	11.0	7.0	−5.5	−0.6	1.1	0.69	7
	V_X1	4526.2	43.8	4.6	−7.06	−0.17	−0.2	−0.2	2.1	−1.0	2.3	0.4	0.91	7
	V_X2	4578.9	39.9	5.2	−7.72	0.47	−0.5	0.2	0.6	0.9	2.1	0.4	0.87	7
M	*M_S1*	4812.5	−25.0	4.9	−0.28	0.83	−15.5	13.2	1.3	0.1	−0.8	1.0	1.22	8
	M_S2	4808.4	−26.2	12.7	−0.28	0.83	−15.7	13.7	0.5	0.1	−0.7	0.4	1.24	7
	M_X1	4543.2	42.8	15.0	−5.52	−1.93	−0.03	−1.3	5.0	−4.3	2.2	0.9	0.92	6
	M_X2	4541.2	43.1	14.4	−6.54	−1.47	−0.1	−0.3	1.1	0.3	2.2	0.8	0.88	6

The model accuracy was investigated analyzing at first the residuals on the CPs (i.e., the differences between GNSS-measured coordinates and photogrammetric ones), that give an indication also on possible georeferencing errors. In Table 2.4, the mean value μ and standard deviation σ for CP residuals are reported for each dataset, showing both the signed residuals for the three components (*X,Y,Z*) and the total 3D error. For the latter, the statistics are expressed also as a function of the

average GSD. In the following sections, we will discuss in detail the results on CP residuals reported in Table 2.4.

Table 2.4 *Residuals on Check Points (in cm). Mean value μ and standard deviation σ are reported for each component (X,Y,Z) and for the total 3D error. For the latter, mean and standard deviation are reported also as a function of the average GSD.*

Study Site	Dataset	μ_X [cm]	σ_X [cm]	μ_Y [cm]	σ_Y [cm]	μ_Z [cm]	σ_Z [cm]	μ_{3D} [cm]	σ_{3D} [cm]	μ_{3D} [GSD]	σ_{3D} [GSD]
P	*P_S1*	0.2	1.1	−0.5	1.5	0.0	1.3	2.1	0.8	2.4	1.0
	P_S1_8_GCP	0.3	1.0	−0.6	1.4	−0.1	1.2	2.0	0.8	2.3	1.0
	P_S1_3_GCP	−0.2	0.6	−0.5	2.0	0.5	1.2	2.2	0.9	2.5	1.1
	P_S2	0.4	1.2	−0.5	1.8	0.0	1.0	2.3	0.7	2.2	0.6
	P_X1	0.0	2.3	−0.2	2.5	−0.3	2.8	4.0	1.5	7.1	2.7
	P_X2	0.3	2.2	−0.1	2.6	0.4	2.8	4.0	1.8	7.7	3.5
	P_X2_8_GCP	−0.5	2.5	−0.2	2.0	−0.6	3.4	4.3	1.8	8.3	3.6
	P_X2_3_GCP	0.5	2.3	−0.4	2.3	−5.0	6.6	7.3	5.0	14.1	9.8
	P_X2_PE1	0.2	2.3	−0.1	2.4	0.1	3.0	4.0	1.7	7.8	3.3
	P_X2_PE2	0.4	2.3	−0.3	2.3	0.2	2.9	4.0	1.6	7.7	3.2
V	*V_S1_2019*	−0.1	1.1	0.0	1.3	0.4	1.1	1.8	0.8	2.7	1.3
	V_S2_2019	−0.6	2.0	−0.1	1.4	0.3	1.2	2.5	1.0	3.1	1.3
	V_S1	−0.1	0.8	−0.1	0.6	−0.7	1.4	1.5	1.0	2.1	1.5
	V_S2	0.0	0.8	−0.2	0.6	−0.2	0.9	1.2	0.6	1.8	0.9
	V_X1	0.3	1.6	−0.2	0.9	0.1	1.7	2.0	1.6	2.7	2.1
	V_X2	−0.1	1.0	−0.1	0.9	−0.9	1.8	2.1	0.9	2.9	1.3
M	*M_S1*	0.6	0.8	−0.3	0.6	0.2	1.5	1.8	0.5	2.2	0.6
	M_S2	0.4	0.7	−0.4	0.7	0.9	1.6	1.9	0.9	2.8	1.3
	M_X1	0.5	0.9	−0.3	0.5	−0.3	1.9	1.9	1.2	3.2	2.1
	M_X2	0.4	0.8	−0.3	0.5	−0.1	1.8	1.7	1.1	2.8	1.8

As further figure of merit, we evaluated the distances between dense point clouds (CoDs) for precision assessment. Figure 2.3, Figure 2.4 and Figure 2.5 illustrate the M3C2 distance between pairs of models for the three study areas, while Table 2.5 shows the corresponding statistics.

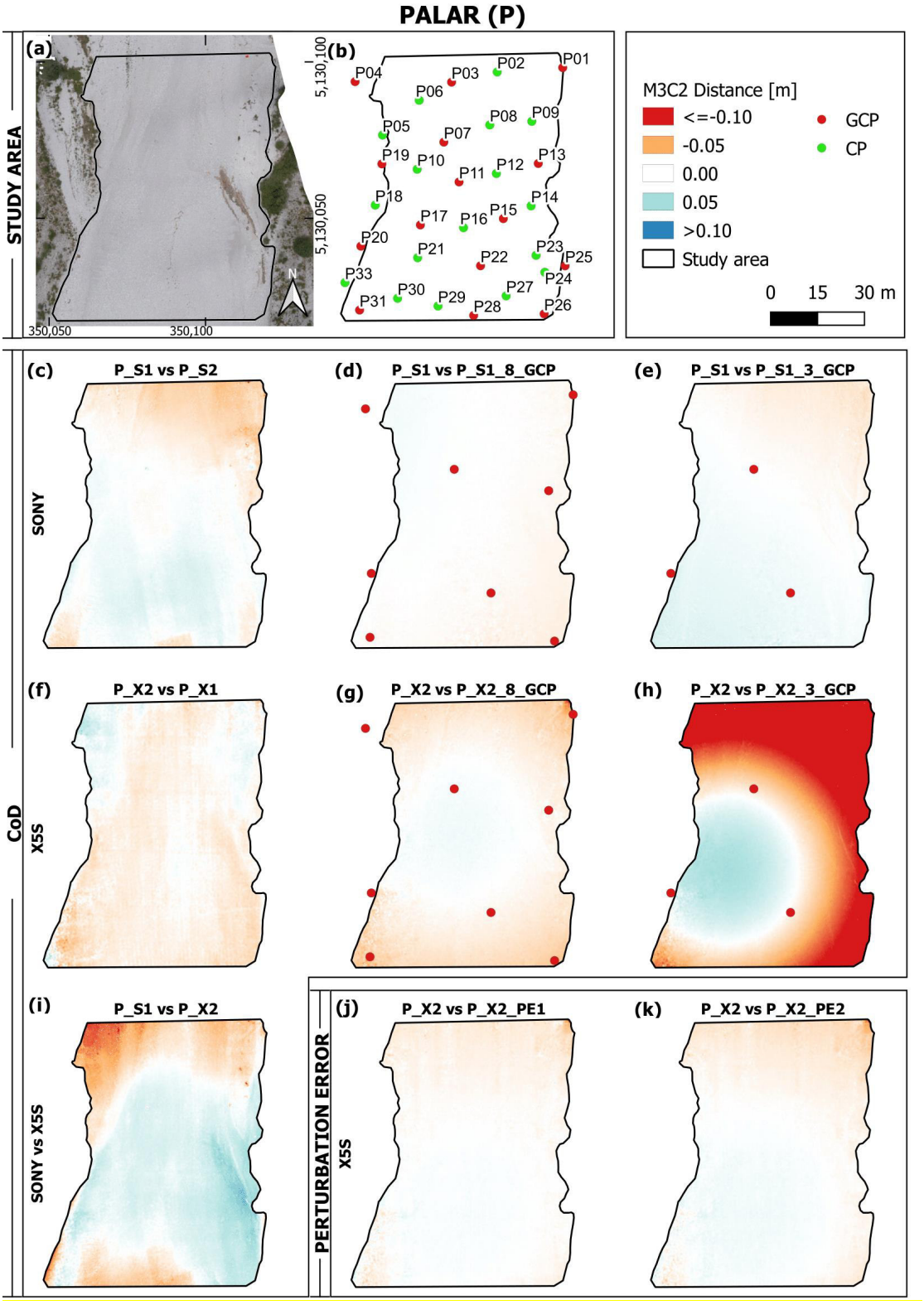

Figure 2.3 *CoDs of Palar models obtained using different cameras, different number of GCPs and varying GCP coordinate precision. (**a**) Study area. (**b**) GCPs (red) and CPs (green) positions. (**c,f,i**) CoDs derived from Sony and X5S point clouds, exploiting all available GCPs in the bundle adjustment. Comparisons between the reference point cloud and those obtained with 8 and 3 GCPs are reported in (**d,e**) for Sony image set and (**g,h**) for X5S camera. In (**j,k**) the effect of two levels of perturbation error introduced in the GCP coordinates are shown for X5S camera. Distance values are pictured with a red-to-blue gradient.*

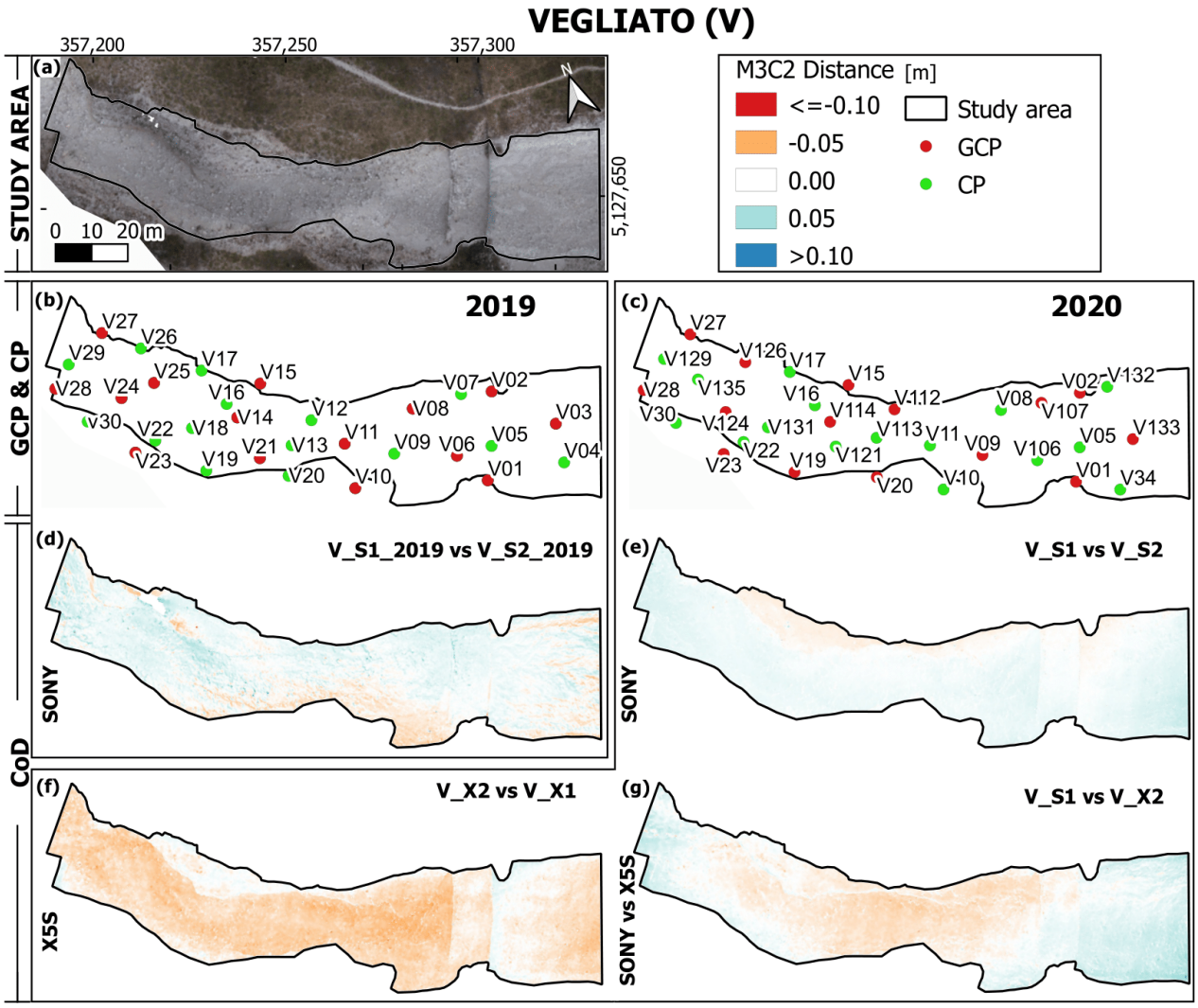

Figure 2.4 *CoDs of Vegliato datasets collected in different years using different cameras. (**a**) Study area. (**b,c**) GCPs (red) and CPs (green) positions for 2019 and 2020 surveys. (**d,e**) CoDs derived from Sony datasets for 2019 and 2020, respectively, and (**f**) the one from X5S. The CoD in (**g**) represents the comparison between the point clouds derived from different cameras (V_S1 vs V_X2). Distance values are pictured with a red-to-blue gradient.*

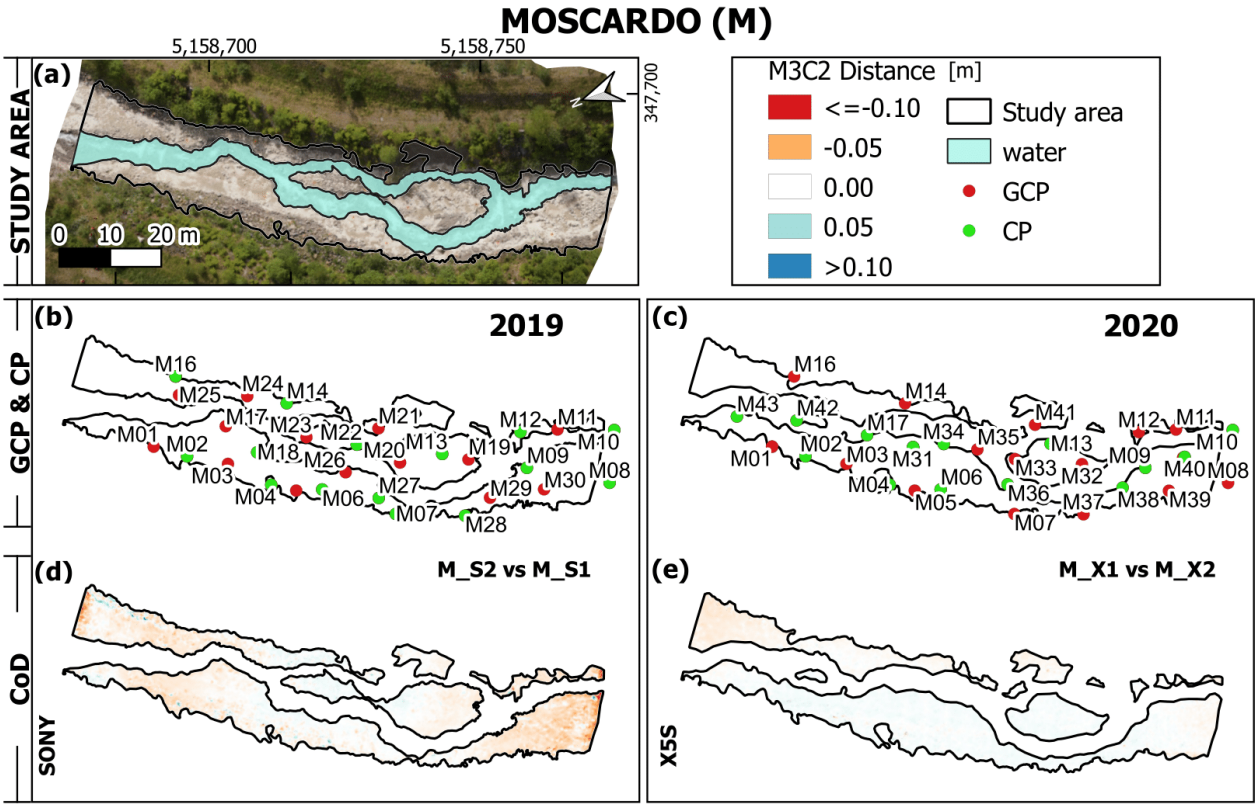

Figure 2.5 *CoDs of Moscardo models. Evaluated datasets were collected in different years using different cameras. (**a**) Study area (water have been removed to avoid biased comparisons). (**b,c**) GCPs (red) and CPs (green) positions for 2019 and 2020 surveys. (**d**) CoD derived from the comparison between M_S1 and M_S2. (**f**) CoD computed between X5S surveys (M_X1 vs M_X2). Distance values are pictured with a red-to-blue gradient.*

Table 2.5 *Summary statistics of M3C2 distance values for all the compared point clouds. Mean ± standard deviation and RMS are reported (in cm).*

Study Site	Reference Set	Compared Set	$\mu \pm \sigma$ [cm]	RMS [cm]
P	*P_S1*	*P_S2*	-0.1 ± 1.3	1.3
	P_X2	P_X1	-0.6 ± 0.8	1.0
	P_S1	*P_X2*	0.4 ± 2.6	2.6
	P_S1	*P_S1_3_GCP*	0.3 ± 0.8	0.9
	P_S1	*P_S1_8_GCP*	-0.1 ± 0.3	0.3
	P_X2	*P_X2_3_GCP*	-6.0 ± 8.3	10.3
	P_X2	*P_X2_8_GCP*	-0.7 ± 1.0	1.2
	P_X2	*P_X2_PE1*	-0.2 ± 0.5	0.6
	P_X2	*P_X2_PE2*	-0.2 ± 0.8	0.8
V	*V_S1_2019*	*V_S2_2019*	0.5 ± 1.2	1.3
	V_S1	*V_S2*	0.6 ± 0.7	1.0
	V_X1	*V_X2*	-1.7 ± 1.3	2.1
	V_S1	*V_X2*	0.2 ± 1.5	1.5
M	*M_S1*	*M_S2*	-0.6 ± 1.2	1.4
	M_X1	*M_X2*	0.1 ± 0.5	0.5

The outcomes are detailed in the following describing separately (i) survey repeatability and the use of different cameras, (ii) different number of GCPs and varying GCP coordinate precision, and (iii) different flight modes.

2.4.1 Assessment of Survey Repeatability and Camera Influence

At first, replicas of the same survey (i.e., performed with the same camera under similar conditions and processed with all available GCPs) are taken into account. As shown by the summary values of Table 2.4 and further highlighted by the boxplots of the CP residuals reported in Figure 2.6, for all three study areas datasets acquired with the same equipment lead to equivalent accuracy. For example, for the Palar site the mean 3D error on CPs is 2.1 cm (σ = 0.8 cm) for P_S1 and 2.3 ± 0.7 mm for P_S2, respectively, while for the Vegliato area we obtained an average 3D residual of 1.5 ± 1.0 cm for V_S1 and 1.2 ± 0.6 mm for V_S2. Similar behaviour can be appreciated also for the surveys performed with the X5S camera. For instance, the mean absolute error on CPs for the Moscardo area is 1.9 ± 1.2 cm for M_X1 and 1.7 ± 1.1 cm for M_X2. Analogous conclusion can be drawn also considering the residuals expressed as a function of the average GSD: the highest difference can be found between the surveys M_S1 and M_S2, characterized by an average 3D residual on the CPs of 2.2 GSD and 2.8 GSD, respectively.

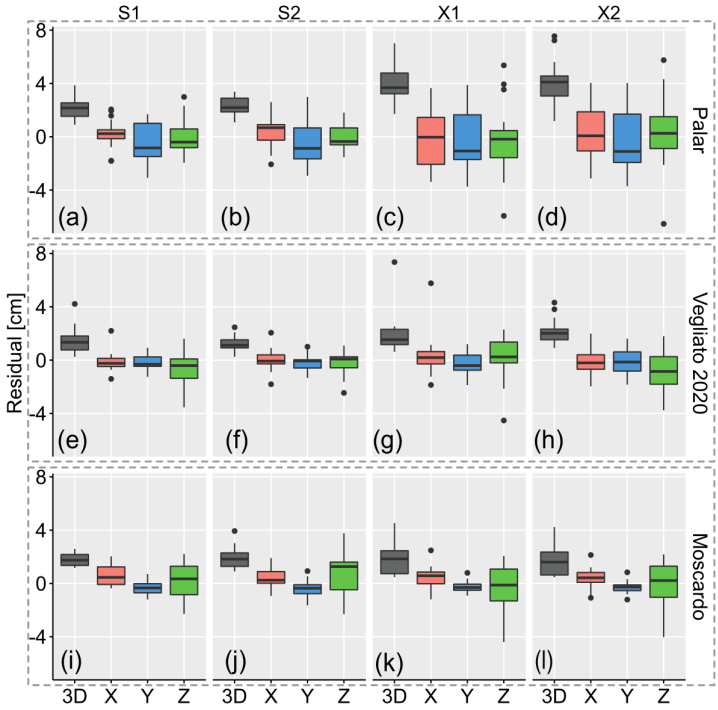

Figure 2.6 *Comparison of CP residuals obtained from different surveys and study areas. (**a–d**) Palar, (**e–h**) Vegliato 2020, (**i–l**) Moscardo. 'S' were surveys performed with the Sony camera, whereas 'X' referes to X5S datasets. The 3D total error is reported in grey, while pink, blue and green represents residuals in the X, Y and Z direction, respectively. These results were obtained using all available GCPs for each study area.*

High coherence between repeated surveys is demonstrated also by the CoDs shown in Figure 2.3c,f, Figure 2.4d–f and Figure 2.5d,f. From the comparisons among dense point clouds, only for the Vegliato study area we notice a mean value of the M3C2 distance that exceeds 1 cm, between V_X1

and V_X2 datasets (−1.7 ± 1.3 cm, see Table 2.5). In all other cases, repeating the survey with the same camera and using well-distributed GCPs led to average signed distances less than 1 cm and Root Mean Square (RMS) values less than 1.4 cm.

When comparing the results provided by different cameras over the same study area, millimetre differences in terms of average CP residuals can be noticed, except for the Palar study area. In this case, indeed, for the X5S datasets mean and standard deviation are twice the values computed for the Sony image sets. As can be seen from Table 2.4, the errors grow from 2.1 ± 0.8 cm for P_S1 and 2.3 ± 0.7 cm for P_S2 to 4.0 ± 1.5 cm and 4.0 ± 1.8 cm for the X5S datasets. These discrepancies on CP errors can be noticed also in Figure 2.6c,d, with the boxplots related to the P_X1 and P_X2 datasets reaching a mean value of 4.0 cm for the 3D residuals, showing high variability both in the XY-plane as well as in the altitude component. The lower accuracy that characterises these datasets is revealed also by the average 3D error expressed as a function of the GSD, which reaches 7.7 times the GSD (in the other case studies it is between 2 and 3 times the GSD, see Table 2.4). To further investigate these outcomes, we divided the CPs according to their location, and computed error statistics for the three subareas considered (Figure 2.7). The southern region shows greater CP residual values for the X5S datasets, with higher dispersion especially in the Z direction. Analysing the distances between P_S1 and P_X2 point clouds (Figure 2.3i), instead, it could be noticed that the P_X2 one exhibits a dome-like shape, with positive distances with regard to the P_S1 in the central part of the study sites, and negative values on the boundaries. The RMS for the computed distance is equal to 2.6 cm (Table 2.5), which represents also the maximum RMS value among all the comparisons made between datasets processed with proper GCP number. These considerations suggest lower accuracy and precision for the P_X1 and P_X2 models.

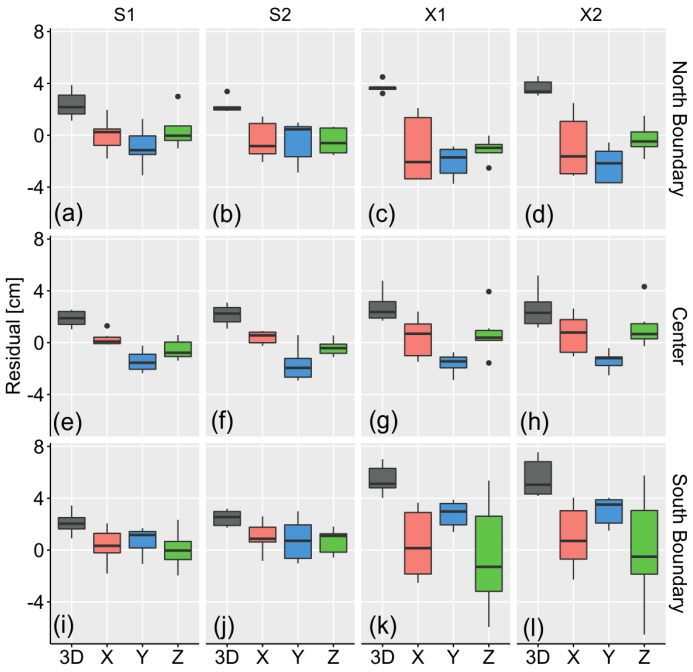

Figure 2.7 *Comparison of CPs residuals for Palar study area. Statistics are computed diving the CPs according to their location (Figure 2.3b) into three areas: (**a–d**) North boundary (including check points P02, P06, P05, P09 and P18), (**e–h**) Center (P08, P10, P12, P16, P14 and P21) and (**i–l**) South boundary (P23, P24, P27, P29, P30 and P33). 'S' surveys were performed with the Sony camera, whereas 'X' refers to X5S datasets. The 3D total error is reported in gray, while pink, blue and green represents residuals in the X, Y and Z direction, respectively. These results were obtained using all available GCPs.*

2.4.2 Assessment of the Effect of the Number and Coordinate Precision of GCPs

As already mentioned in Section 2.3.2, the influence of the number of GCPs employed in the bundle adjustment was tested in the Palar study site, evaluating the results retrieved with 15, 8 and 3 GCPs. With respect to CP residuals (Figure 2.8), models generated from the Sony camera dataset show similar behaviour regardless of the number of GCPs, with an average 3D error of 2.1, 2.0 and 2.2 cm for the three cases (15, 8 and 3 GCPs), and a standard deviation of less than 1 cm (see Table 2.4). Moreover, no significant differences can be noticed in the CoD when comparing the point clouds obtained with 8 GCPs and 15 GCPs (Figure 2.3d). In fact, the corresponding M3C2 distance is equal to -0.1 ± 0.3 cm, with a RMS of 0.3 cm (Table 2.5). Analysing the CoD computed from P_S1 and P_S1_3_GCP (Figure 2.3e), a relative rotation between the two point clouds is slightly visible, which can be due to inaccurate georeferencing of the P_S1_3_GCP model. However, there are still no relevant distances (0.3 ± 0.8 cm on average, RMS is equal to 0.9 cm).

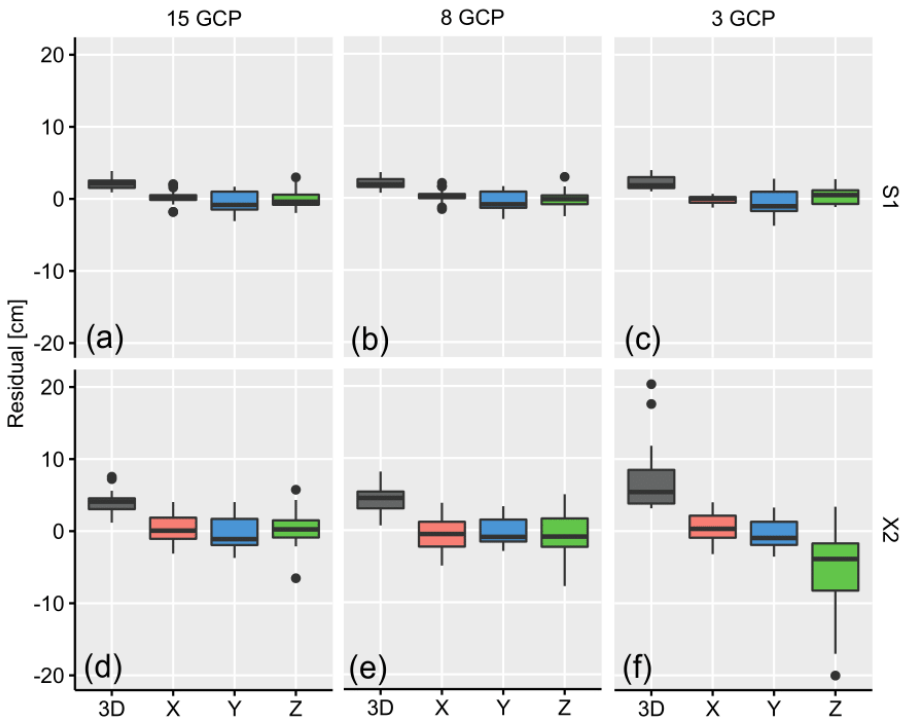

Figure 2.8 *Comparison of CPs residuals for Palar study area using different cameras and different number of GCPs (3, 8 and 15 GCPs). 'S' surveys were performed with the Sony camera (**a–c**), whereas 'X' refers to X5S datasets (**d–f**). The 3D total error is reported in grey, while pink, blue and green represents residuals in the X, Y and Z direction, respectively.*

Conversely, GCP density seems to significantly affect the results obtained from the X5S datasets. In the case of 8 GCPs, a small increase in the error affecting all the components can be noticed (from an average 3D residual of 4.0 cm with 15 GCPs to 4.3 cm with 8 GCPs), whereas with only 3 GCPs (that in our case where also not properly distributed) the average residual on the CPs reaches 7.3 ± 5.0 cm, with maximum differences between GNSS and photogrammetric coordinates of 20 cm. Table 2.4 and Figure 2.8e also show a large increase of the error in the Z direction, that reaches a mean value of −5.0 cm and a standard deviation of 6.6 cm. The influence of the number of GCPs for the X5S datasets in further highlighted by the comparison between dense point clouds. Figure 2.3h, in fact, clearly displays decimetre differences (RMS is 10.3 cm) between P_X2 and P_X2_3_GCP, with the model retrieved with only 3 GCPs showing a domed shape. Although to a lesser extent, this behaviour is also visible in the P_X2_8_GCP point cloud. Of course, varying the location and distribution of the 3 GCPs could have significantly changed the results and the error distribution. However, the main goal of this test was to confirm that the minimum number of constraints is usually not sufficient to produce a reliable model.

After having assessed the dependence of the results on the GCP number, it is interesting to verify the influence of the precision of GCP measurements. As explained in Section 2.3.2, the GNSS

coordinates were perturbed adding two different level of Gaussian noise. The consequences are not so relevant: in fact, the 3D residual on the CPs is constant for the three cases (4.0 ± 1.5 cm for P_X2, 4.0 ± 1.6 cm for P_X2_PE1 and 4.0 ± 1.7 cm for P_X2_PE2, see Table 2.4). Only for the case P_X2_PE2 (Z component perturbed with σ_Z=4 cm) minor distortions in the final model are evident in the form of a dome effect, slightly visible in Figure 2.3k.

A significant reduction of the model accuracy is instead produced by changing the 'marker accuracy' parameter in the bundle adjustment step. We evaluated the results obtained when using the original GCP coordinates but setting this value to 6 cm, noticing also in this case a final model affected by the doming effect. In this situation, the software employs the GCPs as softer constraints, reducing their positive effect on the final bundle adjustment solution.

2.4.3 Assessment of UAV Flight Mode Impact

To investigate the impact of manual and planned flights, in the Vegliato study area, we compared the results obtained for the Sony datasets acquired with the NT-4C UAV in 2019 and with the DJI Matrice in 2020. The flight missions were performed at the same altitude and using the same camera settings. Focusing on the CPs residuals, one can notice slightly higher 3D error variability for the datasets acquired in manual mode (Figure 2.9), with mean values of 1.8 ± 0.8 cm and 2.5 ± 1.0 cm (corresponding to 2.7 ± 1.3 GSD and 3.1 ± 1.3 GSD) for V_S1_2019 and V_S2_2019, respectively. The average 3D residual decreases to 1.5 ± 1.0 cm and 1.2 ± 0.6 cm (corresponding to 2.1 ± 1.5 GSD and 1.8 ± 0.9 GSD) for the two image sets collected in planned mode, as shown in Table 2.4. An indirect comparison can be performed also analyzing the CoDs obtained from the two pairs of flights. In the CoD computed from V_S1_2019 and V_S2_2019 models (Figure 2.4d) higher distances are visible all over the study area, whereas for the planned flights (Figure 2.4e) major differences between the two replicas are localised out of the GCP perimeter and downstream of the check dams.

To give further insights on how the flight mode can influence the result, in Figure 2.10 we show image locations for flights V_S2_2019 (manual flight, Figure 2.10a) and V_S2 (planned flight, Figure 2.10b). It is easy to notice the more regular image distribution that characterizes the planned flight, which guarantees uniform overlap and sidelap. Although the average tie-point multiplicity (i.e., the ratio between the total number of projections and the number of tracks) is equivalent for both flight modes (3.94 for the manual and 3.80 for the planned flight), the nonuniform coverage of the area of interest could justify the lower accuracy (see CP residuals, Figure 2.9) and precision (see the

corresponding CoDs, Figure 2.4d for the manual flights and Figure 2.4e for the planned mode) that affects the models obtained from manual flights.

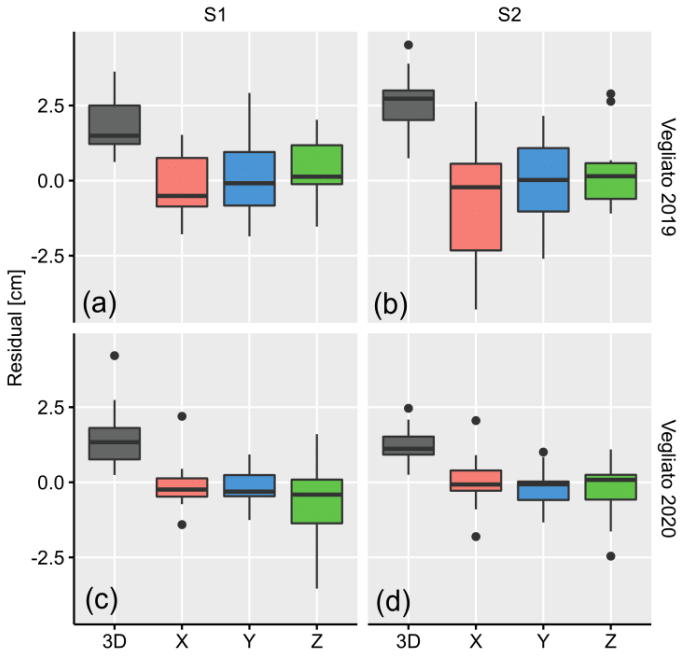

Figure 2.9 *Comparison of CPs residuals for Vegliato study area using manual (**a,b**) or programmed (**c,d**) flight mode. Sony camera was employed for data acquisitions. The 3D total error is reported in gray, while pink, blue and green represents residuals in the X, Y and Z direction, respectively.*

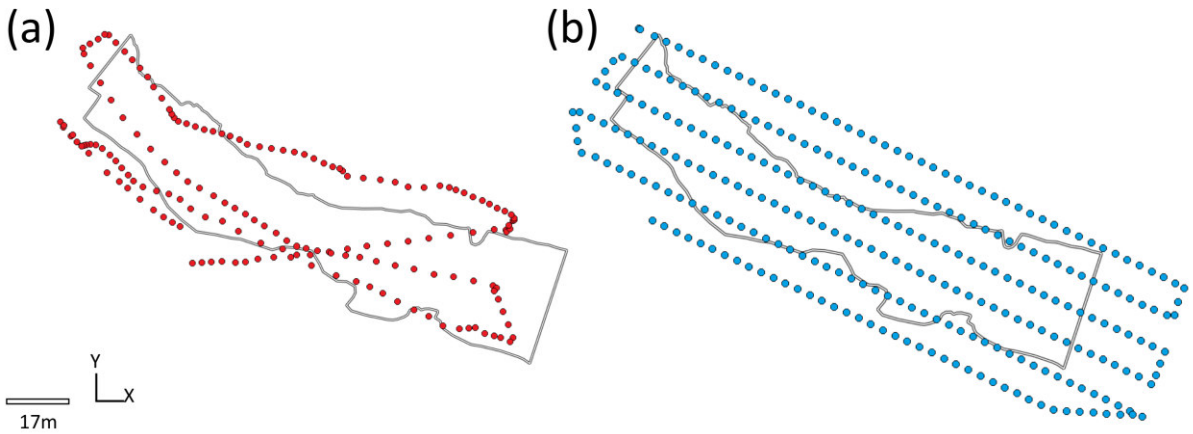

Figure 2.10 *Image locations for flights (**a**) V_S2_2019 (manual flight) and (**b**)V_S2 (planned flight). Please note the more regular image distribution that characterizes the planned flight.*

2.5 Discussion

Performing repeated surveys under the same conditions can give an insight on SfM precision. This turns out to be essential when estimating surface changes by means of photogrammetric surveys, in order to avoid false positives or to overestimate changes.

Overall, results reported in Section 2.4.1 show very good survey repeatability, with minor differences (RMS $\leq$ 2.1 cm) between the point clouds produced with images acquired with the same camera under similar conditions. Moreover, CoDs do not show spatial patterns that could be ascribed to systematic errors. Most of the analyzed surveys performed on different study areas are characterized by similar accuracy, measured in terms of CP residuals. To avoid biased comparisons due to the different GSD associated to each image set, 3D errors were also expressed as a function of the GSD, resulting in a mean 3D residual ranging from 1.8 to 3.1 times the GSD. The only exception is represented by the surveys carried out with the X5S camera over the Palar site. In these cases, CP errors are slightly higher, reaching an average value of 4.0 ± 1.8 cm for the P_X2 case, that corresponds to 7.7 times the GSD.

This case study also highlights the dependence of the results on the camera used. For the Palar surveys, in fact, models derived from the Sony datasets are more accurate, despite the higher GSD that characterizes these image sets. A possible explanation for such behaviour could be found in the different size of the sensors (357 mm^2 for the Sony and 225 mm^2 for the X5S camera, respectively), with the Sony camera producing sharper photos. However, it should also be underlined that the differences between models produced with the two cameras are not so significant for the other sites: the roughness that characterizes the surveyed area can therefore, can play an important role in the final accuracy and precision.

In accordance with the outcomes that can be found in several papers [16,23,29,30], the experiments reported in Section 2.4.2 clearly demonstrate that another factor that can influence SfM accuracy and precision is the number of GCPs employed in the bundle adjustment. A reliable model, indeed, can be obtained when processing the datasets with proper GCP density and distribution, with GCPs placed also on the boundaries or even outside the study reach [9,31,32]. For the cases previously discussed, using all available GCPs resulted in a density of 5 to 10 GCPs per 100 photos, that respects the suggestion given in [16], according to which more than 3 GCPs per 100 photos should be considered to reach high accuracy. When using a smaller number of GCPs (1.8 GCP per 100 photos in our tests) the model retrieved by the SfM algorithm can reveal local distortions or georeferencing inaccuracies, as shown by P_X2_3_GCP and P_S1_3_GCP, respectively (regardless of the choice of the GCP location). Even for this test, the X5S dataset seems to be more affected by the number of GCPs

employed than the Sony images. In particular, the P_X2_3_GCP model shows the well-known dome shape, frequently discussed in the literature [22,33]. The dome effect could have also been mitigated by adding oblique images (20–35° camera angle) or two orthogonal strips [29,34].

We would like to underline that, even in the cases where CP residuals are high and the model presents significant distortion (i.e., P_X2_3_GCP), the reprojection error does not increase (0.76 pixel, see Table 2.3). As already assessed in other works [20,35], this is a further proof that image-space error is not a reliable indicator of the model accuracy.

The uncertainty and inherent variability of the GNSS measurements, acquired with the PPK technique, do not show a significant impact as demonstrated by the results of the tests performed by perturbing the coordinate of the GCPs. This naturally applies as long as the accuracy of the GCPs is better than or equal to the accuracy of the model.

Finally, regarding the influence of the flight mode, experimental evaluation shows slightly higher accuracy for the model retrieved from planned flights with respect to manual ones (using the same camera for image collection). The former mode, in fact, allows to strictly respect design image overlap and to ensure a more homogeneous coverage of the surveyed area (Figure 2.10), avoiding that some areas are covered by a few frames, which could negatively affect tie-point visibility and the whole SfM process. Nevertheless, commercial drones without a DEM support can only fly in planned mode at a specific altitude above see level, that causes differences in GSD in steep slope areas.

2.6 Conclusions

Performing multiple UAV surveys under similar conditions within short time intervals and over several study areas allowed to enhance our understanding of SfM precision. The SfM technique showed high repeatability, whereas significant distances on the resulting 3D model can be appreciated when different cameras are used to survey challenging scenarios (i.e., flat surfaces with homogeneous texture). The SfM reproducibility can therefore be a crucial factor that must be taken into account in change detection applications. When high-precision point cloud data are required, we recommend to test model reproducibility (and in particular the effect of adopting different cameras) over different scenarios, since generalizing the results retrieved over a specific study area could be misleading. GCPs remain essential to generate accurate models, and an independent set of CPs should always be measured to objectively assess the quality of the obtained results.

Geomorphological studies and sediment dynamic analyses require periodic data acquisitions for a considerable time; changing instrumentation (e.g., cameras and GNSS receiver) and protocols (e.g.,

GCP density or flight mode) during a long evaluation period is thus very likely and it could lead to inconsistent results in data comparison. The method employed in this paper, based on repeated surveys, could be valuable to address these issues.

In a future work, we will investigate how SfM accuracy and precision can affect the volume estimate, computed from multi-temporal surveys over areas characterized by surface changes.

AUTHOR CONTRIBUTIONS

Conceptualization A.B., F.C., S.C., J.D.M. and E.M.; Data curation A.B., F.C., S.C., J.D.M. and E.M.; Formal analysis A.B., J.D.M.; Funding acquisition F.C.; Investigation A.B., F.C., S.C., J.D.M. and E.M.; Methodology A.B., F.C., S.C., J.D.M. and E.M.; Supervision A.B. and F.C.; Visualization J.D.M. and E.M.; Writing—original draft J.D.M. and E.M.; Writing—review & editing A.B., F.C., S.C., J.D.M. and E.M. All authors have read and agreed to the published version of the manuscript.

FUNDING

This study was carried out in the framework of a PhD studentship funded by the Universities of Udine and Trieste (Department of Agricultural, Food, Environmental and Animal Sciences—DI4A and Department of Life Sciences—DSV). Moreover, this research was founded by INTERREG IT-AUT 2014–2020 project INADEF "Innovative early-warning system for debris flow based on nowcasting and events" (ITAT3035).

ACKNOWLEDGMENTS

The authors would like to thank Riccardo De Infanti for his help during field activities.

Conflicts of Interest: The authors declare no conflict of interest.

ABBREVIATIONS

The following abbreviations are used in this manuscript:

CD Change Detection

CoD Cloud of Difference

CORS Continuously Operating Reference Station

CP Check Point

DEM Digital Elevation Model

GSD Ground Sampling Distance

GCP Ground Control Point

GNSS Global Navigation Satellite System

InSAR Interferometric Synthetic Aperture Radar

LiDAR Light Detection and Ranging

M3C2 Multiscale Model to Model Cloud Comparison

NRTK Network Real-Time Kinematic

PPK Post-Processed Kinematic

SfM Structure-from-Motion

UAV Unmanned Aerial Vehicle (also known as Uncrewed Aerial Vehicle)

VHR Very High Resolution

REFERENCES

1. Singh, A. Review article digital change detection techniques using remotely-sensed data. *Int. J. Remote Sens.* **1989**, *10*, 989–1003, doi:10.1080/01431168908903939.
2. Qin, R.; Tian, J.; Reinartz, P. 3D change detection—Approaches and applications. *ISPRS J. Photogramm. Remote Sens.* **2016**, *122*, 41–56, doi:10.1016/j.isprsjprs.2016.09.013.
3. Westoby, M.J.; Brasington, J.; Glasser, N.F.; Hambrey, M.J.; Reynolds, J.M. Structure-from-Motion photogrammetry: A low-cost, effective tool for geoscience applications. *Geomorphology* **2012**, *179*, 300–314, doi:10.1016/j.geomorph.2012.08.021.
4. Carrivick, J.L.; Smith, M.W.; Quincey, D.J. *Structure from Motion in the Geosciences*; John Wiley & Sons: West Sussex, UK, 2016; ISBN 9781118895818.
5. Turner, D.; Lucieer, A.; De Jong, S.M. Time series analysis of landslide dynamics using an unmanned aerial vehicle (UAV). *Remote Sens.* **2015**, *7*, 1736–1757, doi: 10.3390/rs70201736.
6. Gomez, C.; Allouis, T.; Lissak, C.; Hotta, N.; Shinohara, Y.; Hadmoko, D.; Vilimek, V.; Wassmer, P.; Lavigne, F.; Setiawan, A.; et al. High-Resolution Point-Cloud for Landslides in the 21st Century: From Data Acquisition to New Processing Concepts. In *Workshop on World Landslide Forum*; Springer Nature Switzerland AG: Cham, Switzerland, 2020; pp. 199–213.
7. Piermattei, L.; Carturan, L.; Blasi, F.d.; Tarolli, P.; Dalla Fontana, G.; Vettore, A.; Pfeifer, N. Suitability of ground-based SfM–MVS for monitoring glacial and periglacial processes. *Earth Surf. Dyn.* **2016**, *4*, 425–443, doi: 10.5194/esurf-4-425-2016.
8. De Marco, J.; Carturan, L.; Piermattei, L.; Cucchiaro, S.; Moro, D.; Dalla Fontana, G.; Cazorzi, F. Minor Imbalance of the Lowermost Italian Glacier from 2006 to 2019. *Water* **2020**, *12*, 2503. doi:10.3390/w12092503.
9. Cucchiaro, S.; Cavalli, M.; Vericat, D.; Crema, S.; Llena, M.; Beinat, A.; Marchi, L.; Cazorzi, F. Monitoring topographic changes through 4D-structure-from-motion photogrammetry: Application to a debris-flow channel. *Environ. Earth Sci.* **2018**, *77*, 1–21, doi: 10.1007/s12665-018-7817-4.
10. Backes, D.; Smigaj, M.; Schimka, M.; Zahs, V.; Grznárová, A.; Scaioni, M. River Morphology Monitoring of a Small-Scale Alpine Riverbed Using Drone Photogrammetry and LIDAR. *Int. Arch. Photogramm. Remote Sens. Spat. Inf. Sci.* **2020**, *43*, 1017–1024, doi: 10.5194/isprs-archives-XLIII-B2-2020-1017-2020.
11. López, J.B.; Jiménez, G.A.; Romero, M.S.; García, E.A.; Martín, S.F.; Medina, A.L.; Guerrero, J.E. 3D modelling in archaeology: The application of Structure from Motion methods to the study of the megalithic necropolis of Panoria (Granada, Spain). *J. Archaeol. Sci. Rep.* **2016**, *10*, 495–506, doi:10.1016/j.jasrep.2016.11.022.
12. Cucchiaro, S.; Fallu, D.J.; Zhao, P.; Waddington, C.; Cockcroft, D.; Tarolli, P.; Brown, A.G. SfM photogrammetry for GeoArchaeology. In *Developments in Earth Surface Processes*; Elsevier: Amsterdam, The Netherlands, 2020; Volume 23, pp. 183–205.
13. Eltner, A.; Sofia, G. Structure from motion photogrammetric technique. In *Developments in Earth Surface Processes*; Elsevier: Amsterdam, The Netherlands, 2020; Volume 23, pp. 1–24.
14. Cucchiaro, S.; Maset, E.; Cavalli, M.; Crema, S.; Marchi, L.; Beinat, A.; Cazorzi, F. How does co-registration affect geomorphic change estimates in multi-temporal surveys? *GIScience Remote Sens.* **2020**, *57*, 611–632, doi: 10.1080/15481603.2020.1763048.

15. Fonstad, M.A.; Dietrich, J.T.; Courville, B.C.; Jensen, J.L.; Carbonneau, P.E. Topographic structure from motion: A new development in photogrammetric measurement. *Earth Surf. Process. Landf.* **2013**, *38*, 421–430, doi: 10.1002/esp.3366.

16. Sanz-Ablanedo, E.; Chandler, J.H.; Rodríguez-Pérez, J.R.; Ordóñez, C. Accuracy of unmanned aerial vehicle (UAV) and SfM photogrammetry survey as a function of the number and location of ground control points used. *Remote Sens.* **2018**, *10*, 1606, doi: 10.3390/rs10101606.

17. Meinen, B.U.; Robinson, D.T. Mapping erosion and deposition in an agricultural landscape: Optimization of UAV image acquisition schemes for SfM-MVS. *Remote Sens. Environ.* **2020**, *239*, 111666, doi: 10.1016/j.rse.2020.111666.

18. Remondino, F.; Nocerino, E.; Toschi, I.; Menna, F. A critical review of automated photogrammetric processing of large datasets. *Int. Arch. Photogramm. Remote Sens. Spat. Inf. Sci.* **2017**, *42*, 591–599, doi:10.5194/isprs-archives-XLII-2-W5-591-2017.

19. Cucchiaro, S.; Maset, E.; Fusiello, A.; Cazorzi, F. 4D-SFM photogrammetry for monitoring sediment dynamics in a debris-flow catchment: Software testing and results comparison. *Int. Arch. Photogramm. Remote Sens. Spat. Inf. Sci.* **2018**, *42*, 281–288, doi: 10.5194/isprs-archives-XLII-2-281-2018.

20. Goetz, J.; Brenning, A.; Marcer, M.; Bodin, X. Modeling the precision of structure-from-motion multi-view stereo digital elevation models from repeated close-range aerial surveys. *Remote Sens. Environ.* **2018**, *210*, 208–216, doi: 10.1016/j.rse.2018.03.013.

21. James, M.R.; Robson, S.; Smith, M.W. 3-D uncertainty-based topographic change detection with structure-from-motion photogrammetry: Precision maps for ground control and directly georeferenced surveys. *Earth Surf. Process. Landf.* **2017**, *42*, 1769–1788, doi:10.1002/esp.4125.

22. James, M.R.; Antoniazza, G.; Robson, S.; Lane, S.N. Mitigating systematic error in topographic models for geomorphic change detection: Accuracy, precision and considerations beyond off-nadir imagery. *Earth Surf. Process. Landf.* **2020**, *45*, 2251–2271, doi: 10.1002/esp.4878.

23. Clapuyt, F.; Vanacker, V.; Van Oost, K. Reproducibility of UAV-based earth topography reconstructions based on Structure-from-Motion algorithms. *Geomorphology* **2016**, *260*, 4–15. doi: 10.1016/j.geomorph.2015.05.011.

24. Bartlett, J.; Frost, C. Reliability, repeatability and reproducibility: Analysis of measurement errors in continuous variables. *Ultrasound Obstet. Gynecol. Off. J. Int. Soc. Ultrasound Obstet. Gynecol.* **2008**, *31*, 466–475, doi: 10.1002/uog.5256.

25. James, M.R.; Robson, S.; d'Oleire Oltmanns, S.; Niethammer, U. Optimising UAV topographic surveys processed with structure-from-motion: Ground control quality, quantity and bundle adjustment. *Geomorphology* **2017**, *280*, 51–66, doi: 10.1016/j.geomorph.2016.11.021.

26. Marchi, L.; Cazorzi, F.; Arattano, M.; Cucchiaro, S.; Cavalli, M.; Crema, S. Debris flows recorded in the Moscardo catchment (Italian Alps) between 1990 and 2019. *Nat. Hazards Earth Syst. Sci.* **2021**, *21*, 87–97, doi: 10.5194/nhess-21-87-2021.

27. Piermattei, L.; Carturan, L.; Guarnieri, A. Use of terrestrial photogrammetry based on structure-from-motion for mass balance estimation of a small glacier in the Italian alps. *Earth Surf. Process. Landf.* **2015**, *40*, 1791–1802, doi: 10.1002/esp.3756.

28. Lague, D.; Brodu, N.; Leroux, J. Accurate 3D comparison of complex topography with terrestrial laser scanner: Application to the Rangitikei canyon (NZ). *ISPRS J. Photogramm. Remote Sens.* **2013**, *82*, 10–26, doi: 10.1016/j.isprsjprs.2013.04.009.

29. Manfreda, S.; Dvorak, P.; Mullerova, J.; Herban, S.; Vuono, P.; Arranz Justel, J.J.; Perks, M. Assessing the Accuracy of Digital Surface Models Derived from Optical Imagery Acquired with Unmanned Aerial Systems. *Drones* **2019**, *3*, 15, doi: 10.3390/drones3010015.

30. Oniga, V.E.; Breaban, A.I.; Pfeifer, N.; Chirila, C. Determining the suitable number of ground control points for UAS images georeferencing by varying number and spatial distribution. *Remote Sens.* **2020**, *12*, 876, doi:10.3390/rs12050876.

31. James, M.R.; Robson, S. Straightforward reconstruction of 3D surfaces and topography with a camera: Accuracy and geoscience application. *J. Geophys. Res. Earth Surf.* **2012**, *117*, doi 10.1029/2011JF002289.

32. Eltner, A.; Kaiser, A.; Castillo, C.; Rock, G.; Neugirg, F.; Abellán, A. Image-based surface reconstruction in geomorphometry—merits, limits and developments. *Earth Surf. Dyn.* **2016**, *4*, 359–389, doi: 10.5194/esurf-4-359-2016.

33. James, M.R.; Robson, S. Mitigating systematic error in topographic models derived from UAV and ground-based image networks. *Earth Surf. Process. Landf.* **2014**, *39*, 1413–1420, doi: 10.1002/esp.3609.

34. Nesbit, P.R.; Hugenholtz, C.H. Enhancing UAV–SfM 3D Model Accuracy in High-Relief Landscapes by Incorporating Oblique Images. *Remote Sens.* **2019**, *11*, 239, doi: 10.3390/rs11030239.

35. Maset, E.; Magri, L.; Toschi, I.; Fusiello, A. Bundle Block Adjustment with Constrained Relative Orientations. *ISPRS Ann. Photogramm. Remote Sens. Spat. Inf. Sci.* **2020**, *2*, 49–55, doi: 10.5194/isprs-annals-V-2-2020-49-2020

Chapter 3

Minor Imbalance of the Lowermost Italian Glacier from 2006 to 2019

Jessica De Marco [1,2,*], Luca Carturan [3,4], Livia Piermattei[5], Sara Cucchiaro [1,3], Daniele Moro [6], Giancarlo Dalla Fontana[3] and Federico Cazorzi[1]

[1] Department of Agricultural, Food, Environmental and Animal Sciences (DI4A), University of Udine, Via Delle Scienze, 206, 33100 Udine, Italy

[2] Department of Life Sciences, University of Trieste (DSV), Via E. Weiss, 2, 34128 Trieste, Italy

[3] Department of Land, Environment, Agriculture and Forestry (TESAF), University of Padova, Viale dell'Università, 16, 35020 Legnaro (Padova)

[4] Department of Geosciences, University of Padova, Via Gradenigo, 206, 35131 Padova, Italy

[5] Chair of Physical Geography, Catholic University Eichstaett-Ingolstadt, 85072 Eichstaett, Germany

[6] Autonomous Region Friuli-Venezia Giulia, Direzione Centrale Risorse Agroalimentari, Forestali e Ittiche, Servizio Foreste e Corpo Forestale, Struttura Stabile Centrale per L'attività di Prevenzione del Rischio da Valanga, 33100 Udine, Italy

* Corresponding author

Published as: De Marco, J.; Carturan, L.; Piermattei, L.; Cucchiaro, S.; Moro, D.; Dalla Fontana, G.; Cazorzi, F. Minor Imbalance of the Lowermost Italian Glacier from 2006 to 2019. *Water* **2020**, *12*, 2503. https://doi.org/10.3390/w12092503

3 Minor Imbalance of the Lowermost Italian Glacier from 2006 to 2019

3.1 Abstract

The response of very small glaciers to climate changes is highly scattered and little known in comparison with larger ice bodies. In particular, small avalanche-fed and debris-covered glaciers lack mass balance series of sufficient length. In this paper we present 13 years of high-resolution observations over the Occidentale del Montasio Glacier, collected using Airborne Laser Scanning, Terrestrial Laser Scanning, and Structure from Motion Multi-View Stereo techniques for monitoring its geodetic mass balance and surface dynamics. The results have been analyzed jointly with meteorological variables, and compared to a sample of "reference" glaciers for the European Alps. From 2006 to 2019 the mass balance showed high interannual variability and an average rate much closer to zero than the average of the Alpine reference glaciers (−0.09 vs. −1.42 m water equivalent per year, respectively). This behavior can be explained by the high correlation between annual balance and solid precipitation, which displayed recent peaks. The air temperature is not significantly correlated with the mass balance, which is main controlled by avalanche activity, shadowing and debris cover. However, its rapid increase is progressively reducing the fraction of solid precipitation, and increasing the length of the ablation season.

Keywords: glacier mass balance; glacier dynamics; very small glaciers; debris-covered glaciers; climate change; geodetic method; Structure from Motion (SfM); Terrestrial Laser Scanning (TLS)

3.2 Introduction

In mid- and low-latitude alpine ranges, very-small glaciers (<0.5 km^2) account for 80–90% of the total glacier number [1–3]. Their response to the current atmospheric warming is highly scattered in comparison with larger glaciers [4–9], because the influence of local topo-climatic factors tends to be greater during times of warmer climate [10,11] and with decreasing glacier size [12–14]. For the same reason, and owing to the lack of long enough observation series, their current behavior and response mechanisms are still little known and deserve investigation.

Small perennial ice bodies located hundreds of meters below the regional Equilibrium Line Altitude (ELA) are a common feature in mountain regions characterized by steep rock walls, such as the Dolomites, in the Eastern Italian Alps. These ice bodies were generated by large amounts of snow deposited at the base of rock walls by avalanches, leading to conspicuous net accumulation in the past centuries and decades, and generating perennial ice bodies that still persist today. In addition to

snow, the rock walls release debris that are entrained in these ice bodies and tend to accumulate over their surface when/where ablation prevails over accumulation [15,16]. The direct consequence of this is the build-up of a debris cover that is generally thickest towards the front, and which tends to expand and thicken in periods of negative mass balance.

The mass balance of these ice bodies is highly variable in space, due to the existence of strong lateral gradients of accumulation and ablation, caused by an uneven deposition of avalanche snow, thickness of debris cover, and terrain shadowing. There is also a considerable inter-annual variability in mass balance, which is generally affected by winter precipitation, but is also controlled by the widening or shrinking of the firn area and of the debris-covered area. For example, Carturan et al. (2013) [17] highlighted how the mass balance sensitivity to temperature fluctuations of the Occidentale del Montasio Glacier (Julian Alps, Eastern Italian Alps) is closely related to the extent of firn and debris-covered areas, subject to rapid year-to-year modifications.

General assumptions concerning ELA or Accumulation Area Ratio (AAR) relationships with mass balance are not valid in these environments. In particular, the balanced-budget AAR can be considerably lower than 0.5–0.6, which is the range normally assumed to be valid for non-calving and non-tropical glaciers [18–20]. In addition, the evolution of these ice bodies is also frequently influenced by their interaction with paraglacial and periglacial processes. In particular, when the local topo-climatic conditions are favorable, there is a tendency for glacier remnants to evolve under permafrost conditions and generate rock glaciers [21] or glacial-permafrost composite landforms [22,23].

The overlap of different processes and feedbacks (e.g., the albedo and debris cover), combined with the peculiar response to atmospheric changes and the impossibility of using “traditional” field techniques (e.g., the glaciological method) make it difficult to study and outline the evolution of these small glaciers, even in the near future. Overall, the existing literature suggests that they have a lower sensitivity to air temperature fluctuations, and a higher sensitivity to precipitation variability, compared to glaciers and glacierets unaffected by a large accumulation of avalanched snow and debris [17,24–26]. However, there is the need for improved process-oriented studies at key selected sites, which require observation series of sufficient length and detail.

New opportunities have emerged in the last two decades enabling high-frequency and high-resolution topographic surveys in areas that are otherwise inaccessible, or too dangerous to be surveyed using traditional field techniques. These opportunities are represented by the fast-evolving field of High-Resolution Topography (HRT) techniques. Among these techniques, terrestrial and

airborne laser scanning (TLS and ALS) and Structure from Motion Multi-View Stereo (SfM-MVS, hereafter SfM) have proven to be effective and flexible, at various spatial and temporal scales [27,28] revolutionizing digital elevation models (DEMs) resolution [29,30] and data acquisition in mountain cryosphere investigations [23,31,32]. In particular, SfM has evolved into a valuable, safe, and cost-efficient technique to derive annual geodetic mass changes of small glaciers of similar quality compared to TLS or ALS techniques [32,33]. Moreover, terrestrial and aerial SfM surveys can be combined to overcome the main limits of both techniques [34]. In fact, the terrestrial approach can provide an accurate representation of complex surfaces [35] but its use is limited to small areas and it may poorly represent a homogeneous terrain. On the contrary, aerial surveys (e.g., using Unmanned Aerial Veicles—UAV) can cover wide areas quickly [36], but aerial-derived DEMs are not optimal in cases of steep or vertical terrains [37].

In this work, we present the results of a 13-year time series of high-resolution observations carried out on the Occidentale del Montasio Glacier, in the period from 2006 to 2019. The investigations were aimed at studying the behavior and climatic response of small glaciers fed by avalanches and covered by debris in their ablation area, in the context of Alpine glacier mass balance observations. The geodetic mass balance, surface dynamics and morphological adjustment have been determined by comparing multi-temporal sub-meter resolution DEMs surveyed by means of ALS, TLS, and ground- and UAV-based SfM techniques.

3.3 The Occidentale del Montasio Glacier

The Occidentale del Montasio Glacier (called the "Montasio Glacier" hereinafter) is inventoried as IT4L00003005 in the World Glacier Inventory-WGI [38,39]. It is located in the Eastern European Alps (Italian Julian Alps), close to the border with Austria and Slovenia (Figure 3.1), where it lies at the base of the vertical northern walls of the Mount Jôf di Montasio (2754 m a.s.l.). It covers an area of 0.066 km^2 (length 350 m; maximum width 280 m) and it is the lowermost Italian glacier (elevation ranging from 1860 to 2050 m a.s.l., median elevation at 1900 m a.s.l. and mean elevation at 1910 m a.s.l.).

The glacier is characterized by a steep cone-shaped accumulation area, which is mainly nourished by winter avalanches, whereas the ablation area consists of a more gently sloped surface, entirely covered by a debris layer (Figure 3.2). The terminus is delimited by a moraine complex composed of juxtaposed ridges, built in different periods. The oldest ridge is dated to the Little Ice Age (LIA)

maximum glacier expansion, whereas its inner ridges have been attributed to the beginning of the 20th century [17].

A geophysical survey conducted in September 2010 pointed out that the average ice thickness along a longitudinal and a lower-transverse profile were 15 m and 8.5 m, respectively, with maximum values of 22–24 m in the middle area [17]. The survey showed a heterogeneous layer composed by glacier ice, clasts, till, and flowing melt water at the glacier bed, and an average thickness of ~2.5 m of the debris layer in the lower half of the glacier.

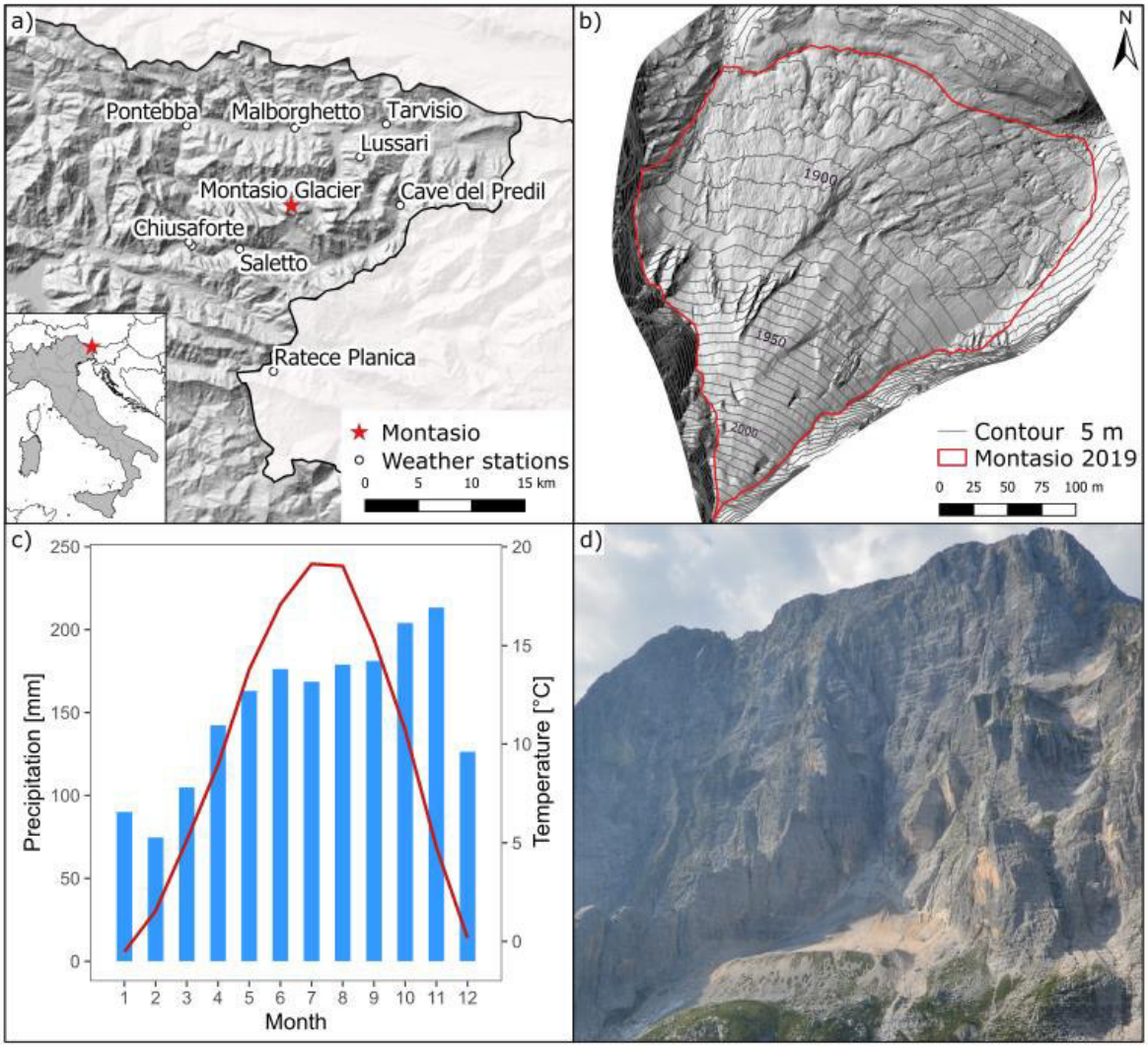

Figure 3.1 *(**a**) Geographic setting of the Montasio Glacier and of the weather stations in the study area; (**b**) glacier topography over the shaded relief map of the high-resolution 2019 SfM survey; (**c**) monthly temperature and precipitation climatology in the period from 1960 to 2009 at the Pontebba weather station; (**d**) photo of the glacier and northern walls of the Mount Jôf di Montasio (Photo F. Cazorzi, 16 August 2012).*

The 1960–2009 climatology at the Pontebba weather station (561 m a.s.l., 12 km north-east of the glacier) is characterized by a mean annual temperature of 9.9 °C. The coldest month is January with

a mean temperature of −0.5 °C, and the warmest month is July with a mean temperature of 19.1 °C. At the glacier's mean elevation, the annual temperature is 1.6 °C. The mean annual precipitation is 1814 mm, with a monthly regime that shows a distinct winter minimum in February (75 mm) and a maximum in November (213 mm, Figure 3.1).

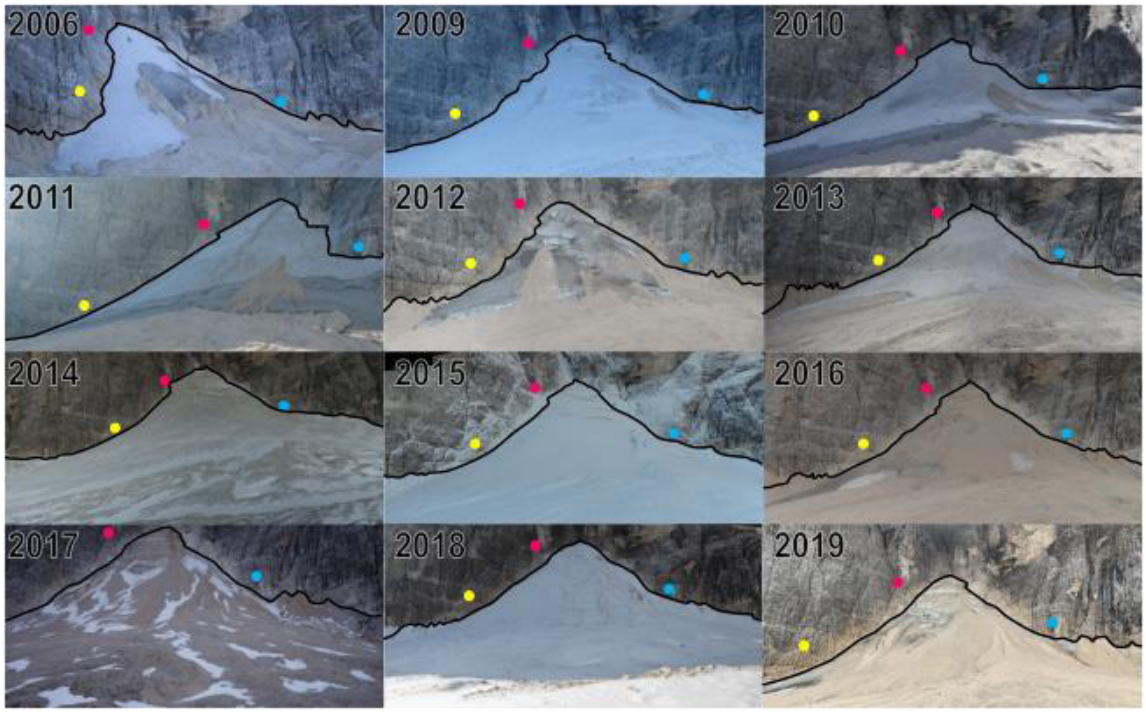

Figure 3.2 *Photos of the Montasio Glacier taken from 2006 to 2019 at the end of the ablation season. Colored dots indicate reference points visible on the rock walls; the black line indicates the upper edge of the glacier.*

3.4 Methods

The mass balance and dynamics of the Montasio Glacier were investigated by means of high-resolution topographic surveys, performed on the glacier and its surroundings over a period from 2006 to 2019. The results have been successively analyzed in comparison with time series of meteorological variables related to glacier mass balance.

3.4.1 Topographic Surveys

Data Acquisition

Topographic surveys were performed at annual intervals from 2010 to 2019, during the second half of September or in October (Table 3.1). Topographic data were acquired using TLS from 2010 to

2013, and SfM from 2014 to 2019. The two techniques were applied jointly in 2012 and 2013 for evaluating and confirming their interchangeability [32].

The TLS surveys were performed using a Riegl LMS-Z620 from two scan positions located over the LIA terminal moraine as reported in Carturan et al. (2013) and in Piermattei et al. (2015) [17,32]. A GNSS (Global Navigation Satellite System) network has been set up with dual-frequency GPS/GLONASS receivers (Topcon HiPer PRO - Topcon Positioning Italy Srl, Ancona, Italy) to geo-reference the TLS surveys in the WGS84/UTM zone 33N (EPSG: 32633) reference system.

Photogrammetric survey methods evolved over the years, as well as cameras and GNSS used in surveys, in order to increase both the survey's quality and efficiency. The ground-based SfM surveys have been integrated with UAV aerial surveys since 2017 (Table 3.1). The georeferentiation and scaling of SfM models were based exclusively on natural targets identified from a TLS point cloud [32], and located over stable areas outside the glacier. In addition to these, artificial Ground Control Points (GCPs) were positioned on the glacier surface and surveyed using GNSS (Leica Zeno20) since 2017.

In order to extend the observation period before 2010, we included the ALS regional survey performed in September 2006 and made available by the Civil Protection Department of the Friuli Venezia Giulia Region.

Table 3.1 *Main characteristics of topographic surveys used in this study. Survey technology: ALS = Aerial Laser Scanning, TLS = Terrestrial Laser Scanning, SfM = Structure from Motion. Platform: T = terrestrial, A = aerial. Camera type: C = Canon EOS 5D Mark III, N = NIKON D5100, S = Sony Alpha 5000.*

Year	2006	2010	2011	2012	2013	2014	2015	2016	2017	2018	2019
Date	13/09	23/09	29/09	05/10	26/09	26/10	20/10	04/10	10/10	03/10	01/10
Technology	ALS	TLS	TLS	TLS	TLS	SfM	SfM	SfM	SfM	SfM	SfM
Platform	A	T	T	T	T	T	T	T	T-A	T-A	T-A
Camera	-	-	-	-	-	C	N	N	S	S	S
DEM resolution [m]	1.00	0.20	0.20	0.20	0.20	0.20	0.20	0.20	0.20	0.20	0.20

Data Processing and DEM Generation

The raw point clouds collected with TLS were processed using the RiSCAN PRO (Riegl) and ArcGIS (ESRI) software in order to obtain georeferenced point clouds, which had a point density ranging between 50 and 60 pts m^{-2}.

The 2006 ALS point cloud had a significantly lower point density (1.63 pts m^{-2} on average) because it was acquired from an aerial platform located at a high distance above the glacier. We co-registered the ALS point cloud to the 2013 TLS point cloud, to optimize accuracy in glacier-change detection. We selected the 2013 TLS survey as a reference, among the four acquired using TLS, because of its highest quality. Stable areas outside the glacier were used as benchmarks for co-registration, which was carried out using the GRD-CoReg free software [40].

The SfM surveys were processed using the computer vision-based software PhotoScan (v. 1.4.3.6488 [41] – Agisoft LLC, St. Petersburg, Russia). The workflow for the generation of the dense point clouds is described in detail in [32,33,36]. The generated point clouds had a mean density of 100 pts m^{-2} and were co-registered to stable areas outside the glacier in the 2013 TLS survey, using the Iterative Closest Point (ICP) algorithm implemented in the OPALS software [42]. Co-registration was required to minimize the residual misalignment between point clouds generated in PhotoScan.

Each ALS, TLS, and SfM point cloud was then converted to a Triangular Irregular Network (TIN) in ArcGIS, and finally transformed into DEMs with 0.2 m spatial resolution. Due to the lower point density, the 2006 ALS point cloud was transformed into a DEM with 1 m spatial resolution.

3.4.2 Mass Balance Measurements and Calculations

The geodetic mass balance was calculated annually differencing DEMs, and accounting for areal variations in glacier extent and different substrata (residual snow, firn, debris-covered ice). Owing to the ample interannual variations in the spatial coverage of these substrata, we could not assume an unchanged density structure of the glacier among consecutive surveys (i.e., Sorge's law [43]) as previously done by Carturan et al. (2013) [17] for the 2010–2011 balance year. Instead, we calculated an area-weighted mean density based on the spatial extent of different substrata, which was used for converting elevation changes obtained from DEMs into depths of water equivalent. In weighted mean density calculations, we used 0.650 kg m^{-3} for residual snow and 0.700 kg m^{-3} for firn, as obtained from direct snow pit measurements. We assigned a density of 0.900 kg m^{-3} to the debris-covered ice.

The annual extent of the substrata was mapped manually using oblique terrestrial and UAV photos, hill-shaded DEMs and DoDs (DEM of Differences). In the upper, debris-free area, the glacier perimeter was updated annually in a similar manner, whereas it was assumed to be unchanged in the

lower part, due to the thick layer of debris that prevents the recognition of short-term fluctuations in glacier margins.

The AAR has been estimated as the ratio between the area covered by residual snow at the end of the ablation season and the total glacier area. It was not possible to calculate the ELA because the geodetic method does not provide the mass balance variation as a function of altitude, and therefore it was not possible to assess the mean elevation corresponding with zero mass balance.

3.4.3 Glacier Dynamics

Vertical and horizontal displacement rates were estimated using hill-shaded DEMs collected in 2010, 2013, 2017, and 2019, which were selected due to their highest quality among all the available surveys. The horizontal displacement was assessed by visual recognition of selected features in the debris-covered area of the glacier.

Horizontal displacement rates in meters per year were calculated using the formula reported in Ai et al. (2019) [44]:

$$Hh = 365.25 \frac{\sqrt{(x_e - x_i)^2 + (y_e - y_i)^2}}{\Delta t} \quad (1)$$

where x_i and y_i are the coordinates of the first observation, x_e and y_e are the coordinates of the second observation, and Δt is the time span in days intercurred.

Vertical displacement rates in meters per year were calculated as:

$$Vh = 365.25 \frac{dZ - dZ_{exp}}{\Delta t} \quad (2)$$

where dZ is the total elevation change between the two surveys ($\bar{z}_e - \bar{z}_i$) and dZ_{exp} is the expected vertical movements calculated based on mean slope angle (for a schematic representation of the displacement components see Bosson and Lambiel (2016) [22]). The mean slope angle was calculated for each investigated point using the initial DEM and averaging the slope within a radius of 5 m. Similarly, the initial mean elevation ($\bar{z}_i$) and ending mean elevation ($\bar{z}_e$) were estimated averaging the DEM elevation with a radius of 5 m.

3.4.4 Meteorological Data Series

The meteorological conditions in the analyzed period were compared to longer time series of meteorological variables related to glacier mass balance, for calculating anomalies and highlighting possible long-term trends. We analyzed air temperature, precipitation, and fraction of solid precipitation (i.e., the nivometric coefficient) in the ablation (May to October) and the accumulation (November to April) seasons, comparing the period from 2010 to 2019 with the 1960–2009 climatology.

Series of air temperature and precipitation data at the weather station of Pontebba (Figure 3.1) were used in the analyses. We used this station because of its proximity to the Montasio Glacier, and for the high-quality and length of meteorological records. Calculations of monthly and seasonal data started mainly from daily measurements; hourly measurements have been used when available (Table 3.2). Quality check, homogenization, and gap-filling required the use of data from several other stations, listed in Table 3.2. The procedures used are in line with the guidelines from the World Meteorological Organization [45] and are detailed in Baldassi (2010) [46].

Table 3.2 *Characteristics of the weather stations and meteorological data used in this study.*

Station Name	Provider Institution [1]	Measured Variable [2]	Frequency [3] (Technique [4])	Working Period	Elevation m (a.s.l.)
Saletto (Chiusaforte)	RMR	T, P	H(A)	2003–	506
Saletto	SIMN	Tx, Tn	D(M)	1919–2013	507
Saletto	SIMN	P	D(M)	1938–2013	507
Pontebba	SIMN	Tx, Tn	D(M)	1915–2013	561
Pontebba	SIMN	P	D(M)	1926–2013	561
Pontebba	RMR	T, P	H(A)	2003–	568
Innsbruck	ZAMG	T, P	D	1877–2004	577
Malborghetto	SIMN	Tx, Tn	D(M)	1986–2013	720
Malborghetto	SIMN	P	D(M)	1921–2013	720
Malborghetto	RMR	T, P	H(A)	2004–	733
Tarvisio	RMR	T, P	H(A)	1999–	794
Ratece Planica	ECA&D	T, P	D	1961–2013	864
Cave del Predil	RMR	T, P	H(A)	2006–	900
Cave del Predil	SIMN	Tx, Tn	D(M)	1948–2013	904
Cave del Predil	SIMN	P	D(M)	1923–2013	904
Lussari	RMR	T, P	H(A)	1999–2017	1760

[1] Provider institutions: SIMN = Servizio Idrografico e Mareografico Nazionale; RMR = Rete Meteorologica Regionale Friuli Venezia Giulia; ZAMG = Zentralanstalt für Meteorologie und Geodynamik; ECA&D = European Climate Assessment and Dataset) [48,49]. [2] Measured variables: T = air temperature, Tx = maximum temperature, Tn = minimum temperature, P = rainfall. [3] Frequency: D = daily, H = hourly. [4] Technique: M = manual, A = automatic.

The obtained daily temperatures have been extrapolated at the mean elevation of the Montasio Glacier (1910 m a.s.l.), using monthly variable vertical gradients calculated over the period from

1999 to 2010 between the Pontebba and Lussari weather stations. The extrapolated temperature served for discriminating between liquid and solid precipitation (daily threshold temperature = 2 °C), required for the estimation of the nivometric coefficient at the glacier's mean elevation. We decided to avoid extrapolating precipitation in a way similar to air temperature, because the study area is affected by large horizontal and vertical gradients [47], which would require high-quality measurements of (gauge-corrected) precipitation at high elevation for their estimation. Because these measurements are not available, we assumed that quality-checked precipitation data at low altitude are more suitable for our analyses than extrapolations subject to a high uncertainty.

3.5 Results

3.5.1 Elevation Change and Mass Balance

The Montasio Glacier experienced significant interannual variability in surface elevation and mass balance in the period from 2006 to 2019. The middle and upper parts of the glacier showed the largest variability whereas the lower part, covered by thick debris, underwent smaller changes (Figure 3.3). Conditions favoring thickening prevailed from 2006 to 2014 (Table 3.3, Figure 3.4), with a cumulated average elevation change of +4.38 m, which corresponds to a mass balance rate of +0.42 m w.e. yr^{-1}. Thinning became dominant after 2014, with a mass balance rate averaging −0.92 m w.e. yr^{-1} from 2015 to 2019 and a cumulated average elevation change of −5.84 m. If the entire period from 2006 to 2019 is considered, the average mass balance rate of the Montasio Glacier was −0.07 m w.e. yr^{-1}. The Montasio Glacier was much closer to balanced-budget conditions than the nine "reference glaciers" of the European Alps (Sarennes, Saint Sorlin, Gries, Silvretta, Hintereis, Kesselwand, Vernagt, Careser and Sonnblick, WGMS [50,51]), whose mass balance rate averaged −1.42 m w.e. yr^{-1} in the same period (Table 3.3).

The large interannual variability in elevation change and mass balance was mostly related to the amount and extent of the snow cover at the end of the ablation season. In favorable years, the middle and upper parts of the glacier developed a snow and firn cover that was several meters thick (Figures 3.2 and 3.3); on the contrary, in unfavorable years, the winter snow vanished almost completely, and the firn of previous years was rapidly melted or buried by debris. The AAR was strongly related to mass balance ($r = 0.94$ considering years with AAR > 0.05). From the linear regression between AAR and mass balance, we can estimate a balanced-budget AAR_0 close to 0.30. Coherent with mass balance behavior, the firn-covered area expanded between 2006 and 2014, and considerably shrunk afterwards (Figures 3.3 and 3.5). The year-to-year variability in mass balance was directly proportional to the extent of the firn area.

Compared to annual changes (Figure 3.3), the spatial pattern of the cumulated elevation changes from 2006 to 2019 (Figure 3.6) looks less dependent on snow and firn cover, and more related to the deposition and spatial reworking of the debris cover. In particular, there are small thickening areas ("a" in Figure 3.6) that correspond to debris flow deposits in the middle and lower parts of the glacier, and a larger thickening area (b) in the middle-upper part, which is the deposit of a landslide fallen on the glacier in 2016. The areas where surface lowering is homogeneous indicate snow and firn melt (c) or ice melt below a thick debris cover (d) in the lower zone; areas showing inhomogeneous lowering represent gully erosion (e), and small sinkholes (f).

Table 3.3 *Comparison of annual balances and Accumulation Area Ratios (AARs) measured on the Montasio Glacier with the geodetic method, and on nine alpine reference glaciers (Sarennes, Saint Sorlin, Gries, Silvretta, Hintereis, Kesselwand, Vernagt, Careser, and Sonnblick) with the glaciological method. The mass balance data for the reference glaciers have been retrieved from Zemp et al. (2020) [50], unless otherwise specified.*

	Montasio Occidentale Glacier (Geodetic Balance)			**Alpine Reference Glaciers (Glaciological Balance)**		
Period [1]	**Annual Balance (m w.e. yr^{-1})**	**Error (m w.e. yr^{-1})**	**AAR**	**Annual Balance (m w.e. yr^{-1})**	**Standard Deviation (m w.e. yr^{-1})**	**AAR (Observations)**
2006–2010	0.52	0.05	/	−1.32	0.65	
2010–2011	−0.25	0.09	0.22	−2.01	1.08	0.11 (7)
2011–2012	−2.18	0.10	0.00	−1.76	0.68	0.08 (7)
2012–2013	0.50	0.05	0.41	−0.55	0.50	0.44 (7)
2013–2014	3.18	0.08	0.74	−0.50	0.78	0.52 (7)
2014–2015	−3.96	0.34	0.00	−2.12	0.80	0.07 (7)
2015–2016	0.40	0.38	0.19	−1.06	0.42	0.20 (7)
2016–2017	−0.64	0.13	0.02	−2.04	0.69	0.04 (7) [2]
2017–2018	0.46	0.10	0.36	−1.77	0.28 [2,3]	0.08 (5) [2,4,5,6]
2018–2019	−0.83	0.11	0.02	−1.37	1.00 [2,3]	0.25 (5) [2,4,5,6]
2006–2019	−0.07	0.01	/	−1.42	0.62	/

[1] Annual average values are reported on multi-year periods. [2] Sonnblickkees data were kindly provided by B. Zagel [52]. [3] Saint Sorlin Glacier data have been downloaded from the GLACIOCLIM website [53]. [4] Vernagtferner data have been downloaded from the Bayerische Akademie der Wissenschaften website [54]. [5] Hintereis ferner and Kesselwandferner data from Rotach M. and Prinz R. (2019) [55]. [6] Careser Glacier data from Baroni et al. (2019) [56].

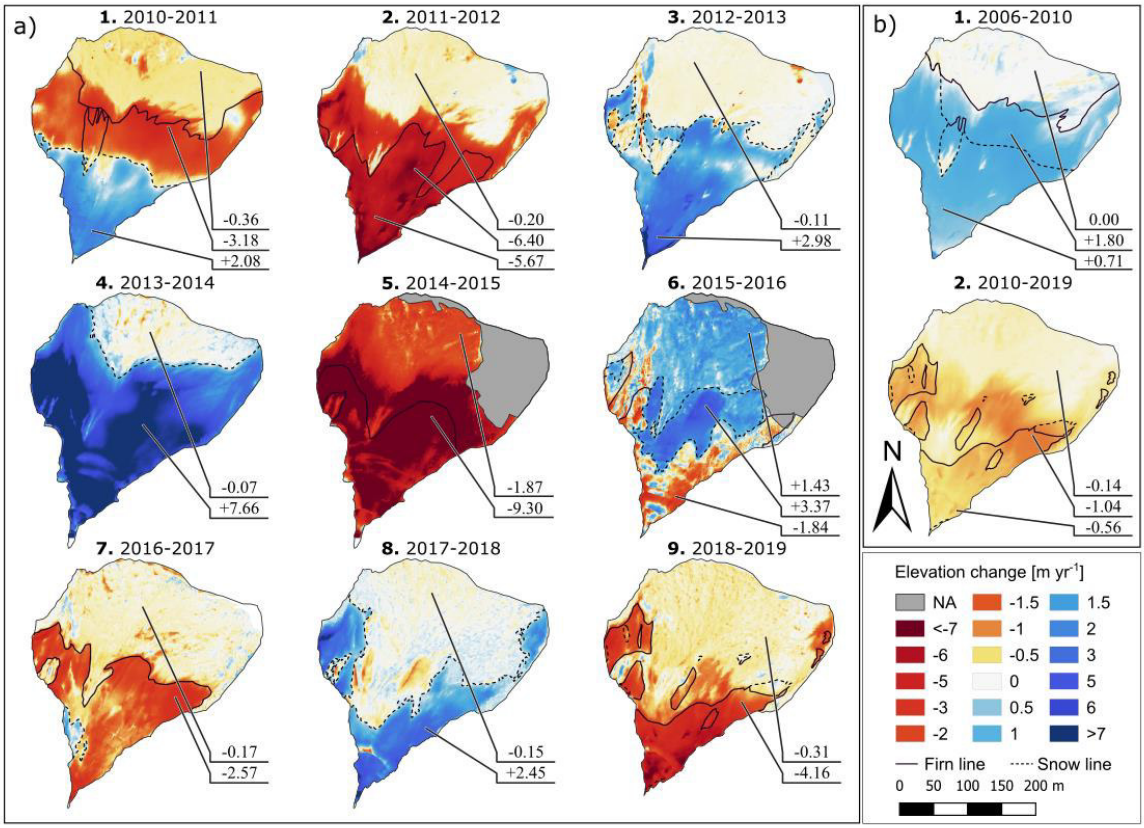

Figure 3.3 *Annual elevation change rate for (**a**) individual years and (**b**) two sub-periods.*

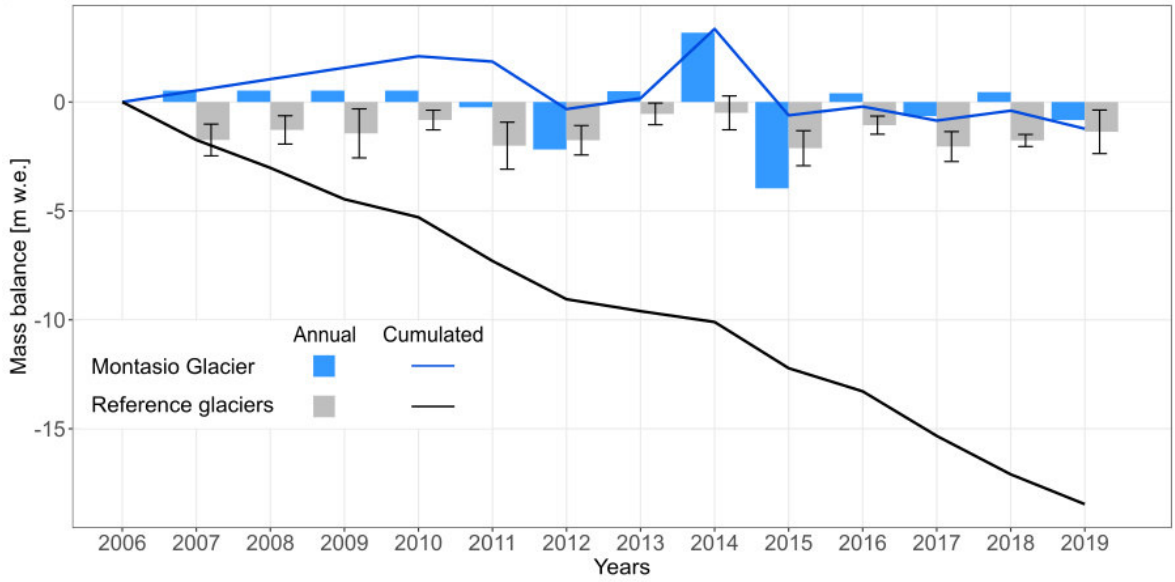

Figure 3.4 *Annual and cumulated geodetic mass balance on the Montasio Glacier compared with the average glaciological annual and cumulated balance of nine reference glaciers in the European Alps, in the period from 2006 to 2019.*

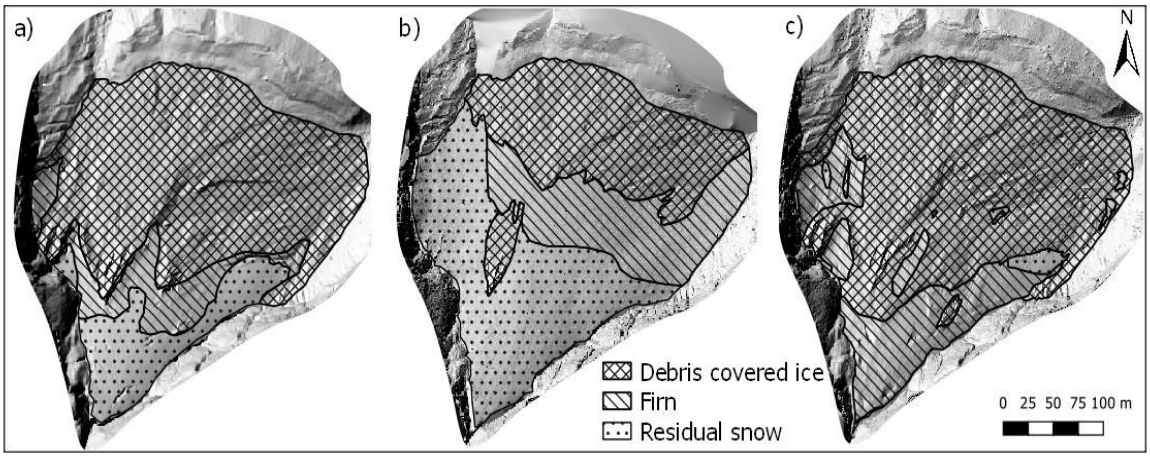

Figure 3.5 *Spatial extent of substrata covering the Montasio Glacier at the end of the ablation season in three different years: (**a**) 2006, (**b**) 2010, and (**c**) 2019.*

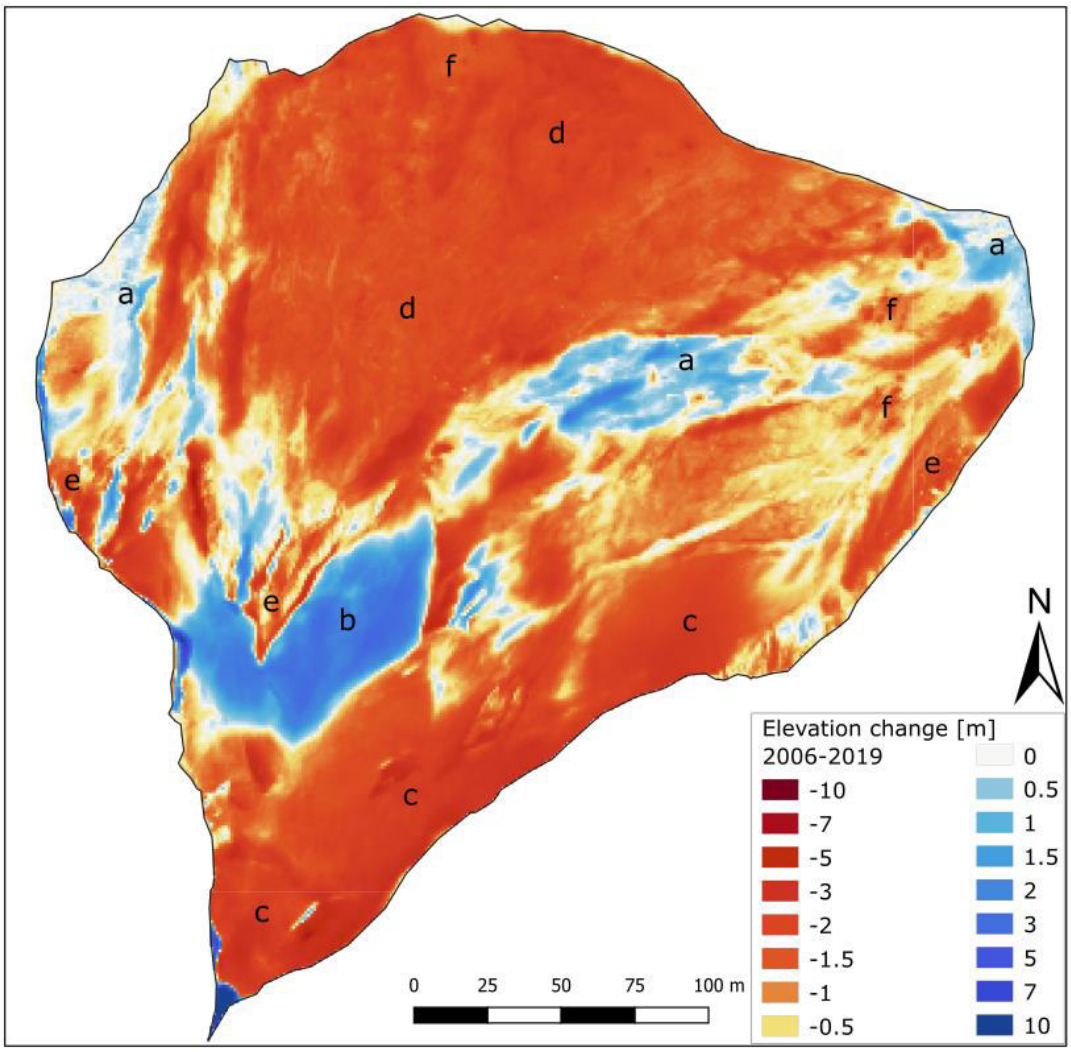

Figure 3.6 *Elevation change cumulated in the period from 2006 to 2019 on the Montasio Glacier. The letters represent areas described in Section 3.5.1.*

3.5.2 Glacier Dynamics

The horizontal surface displacement mapped in the period from 2010 to 2019 shows a divergent pattern (Figure 3.7) that confirms the findings of Carturan et al. (2013) [17]. The movement indicates internal deformation and flow, rather than a mass movement, which, together with mass transfer from the upper accumulation area to the lower ablation area, differentiates the Montasio Glacier from glacierets or ice patches [57].

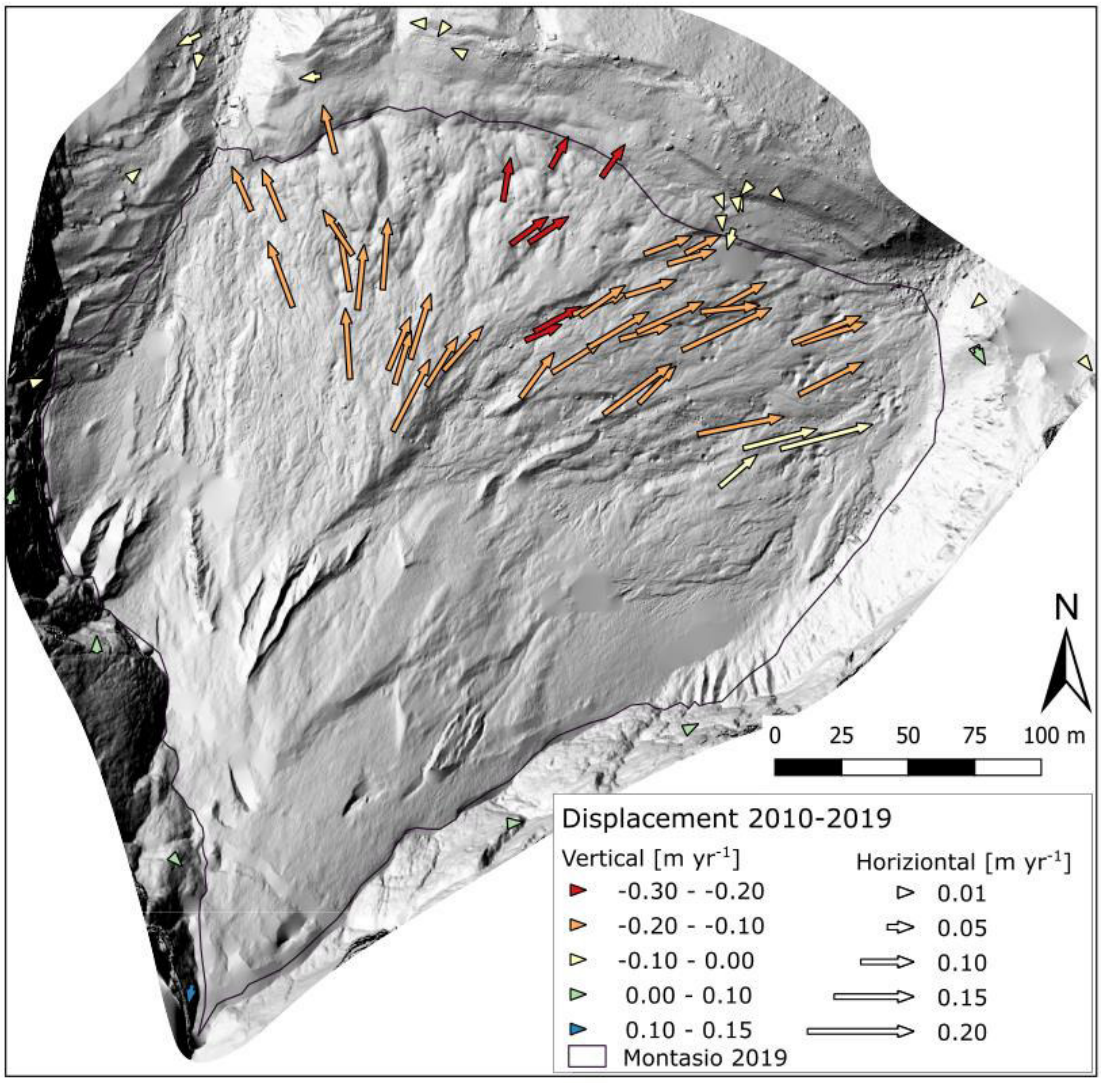

Figure 3.7 *Displacement rates in the period from 2010 to 2019. Arrow lengths show horizontal displacement, whereas colors show vertical displacement. The arrow length used in this image is arbitrary and does not display the real horizontal cumulated displacement.*

Horizontal velocities are lowest in the central part of the glacier front, were subsidence is highest (Figure 3.7). The frontal moraine clearly represents an obstacle to glacier flow, which diverges and tends to be conveyed laterally, towards breaches opened by water erosion at the eastern and western edges of the moraine. Surface and bedrock slope are highest in the eastern part of the glacier front

[17], and therefore surface velocities are maximal in this part of the glacier, which is also characterized by vertical displacements closer to zero.

Analyses focused in three different sub-periods indicate a tendency to deceleration, with decreasing horizontal displacement (Figure 3.8). The slowdown was remarkable after 2017 in the western part, which decelerated from 0.13 to 0.05 m yr^{-1}, whereas it was less significant in the eastern part. Vertical velocities tended towards less negative values, particularly between 2013 and 2017 and in the eastern part. In the last sub-period this tendency looks exhausting or even reversing.

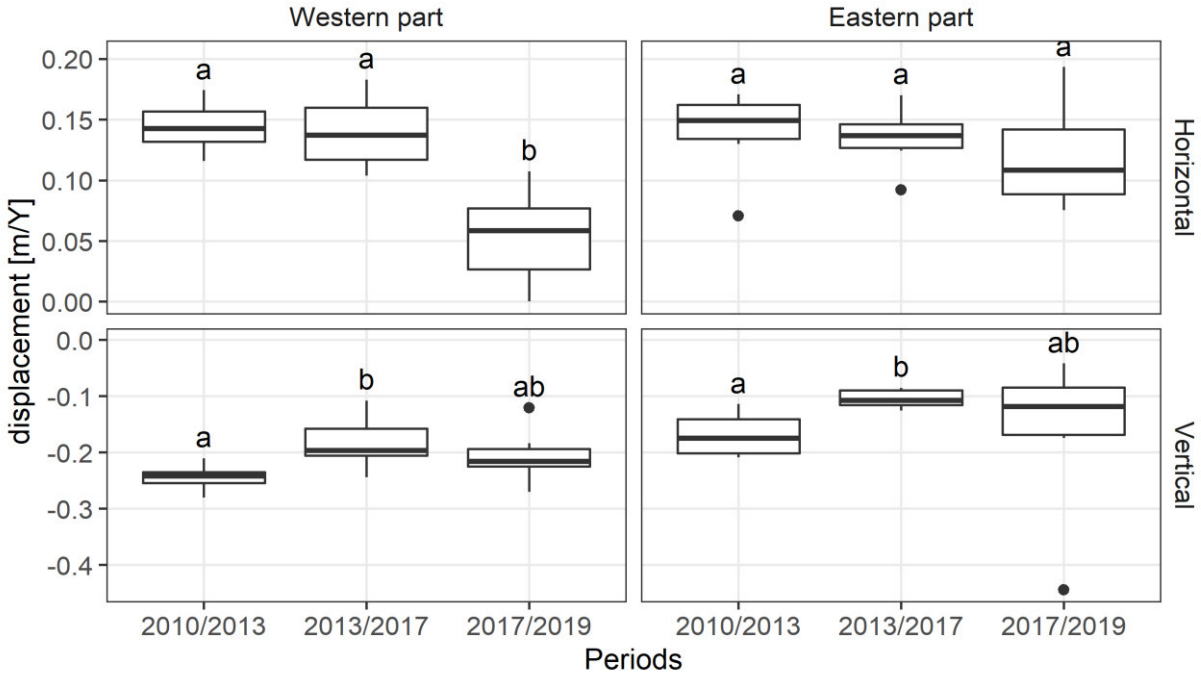

Figure 3.8 *Horizontal and vertical displacement rates in the three sub-periods 2010–2013, 2013–2017, and 2017–2019. The letters above boxplots "a" and "b" indicate which groups of samples are statistically similar (those sharing a common letter) and statistically different (those not sharing a common letter) according to the Wilcoxon test (p-values < 0.05).*

3.5.3 Meteorological Conditions

The long-term trend of the air temperature extrapolated with monthly gradients at the mean elevation of the Montasio Glacier is clearly positive, both in the accumulation and ablation season (Figure 3.9a). According to the Mann–Kendall test, the trend is highly significant ($p < 0.001$) and can be quantified in 0.57 °C/decade for the ablation season, and 0.53 °C/decade for the accumulation season. In the last decade the mean temperature in the ablation and accumulation season was 1.63 °C and 1.79 °C warmer than the 50-year mean, respectively (Table 3.4). We also point out that the ablation season is currently about 3 °C warmer than it was in the period from 1960 to 1980, when glacier advance occurred in the European Alps [58]. The warming trend began in the 1980s and looks to continue.

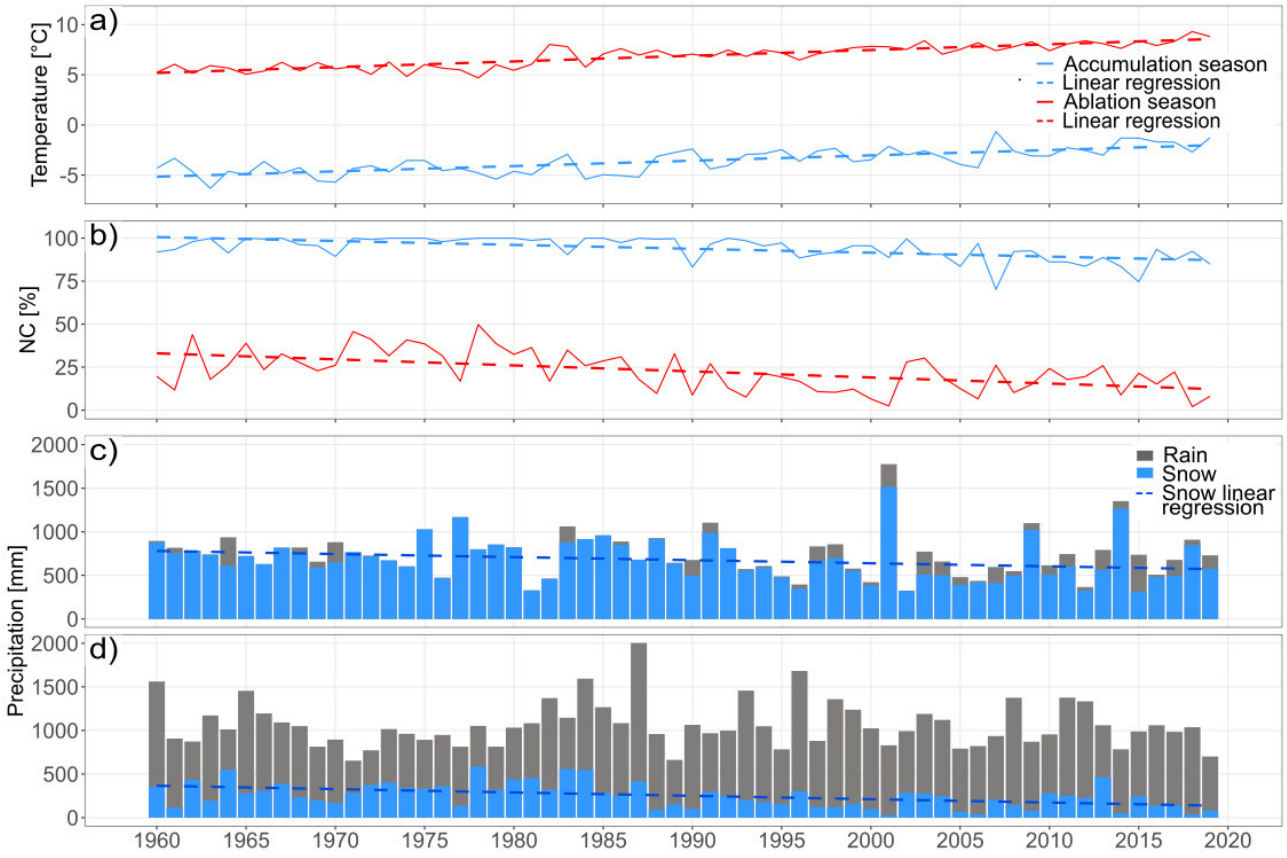

Figure 3.9. *Time series of: (**a**) mean temperature of accumulation and ablation seasons extrapolated at the glacier's mean elevation; (**b**) seasonal nivometric coefficient (NC) at the glacier's mean elevation; total precipitation amount of (**c**) accumulation season, and (**d**) ablation season, fractioned into solid and liquid portions at the glacier's mean elevation.*

The total precipitation in the accumulation and ablation season does not display long-term trends. This lack of trend can be appreciated visually from Figure 3.9c,d, and is confirmed by the Mann–Kendall test, which indicates that trends are not significant ($p > 0.05$). Total precipitation during the

warm semester is 1072 mm on average, which is 42% larger than the average total precipitation amount during cold semesters. In the period analyzed in this work, winters with abundant snowfall (e.g., 2009, 2014, and 2018) alternated with winters with scarce precipitation (e.g., 2012, 2015, and 2016).

Remarkable consequences in the glacier's mass balance are expected from increasing temperature, not only for the augmented melt but also for the decreased fraction of solid precipitation (the so-called nivometric coefficient, NC). As expected from temperature trends, both the accumulation and ablation seasons show decreasing NCs, with statistically significant trends ($p < 0.05$). After a period of stability, the NCs started to decrease in the early 1980s for the ablation season, and in the mid-1990s for the accumulation season. The annual NC decreased from 52% to 45% comparing the two periods 1960–2009 and 2010–2019. The largest variations are observed in spring and autumn, with the months of May, October, and November that have NCs already decreased, or just above, the 50% level (Figure 3.10). This transition of solid towards liquid precipitation is causing a decrease in the length of the accumulation season and a corresponding increase in the length of the ablation season. This transition is even more remarkable if one considers that the most affected months correspond with the annual maxima in precipitation

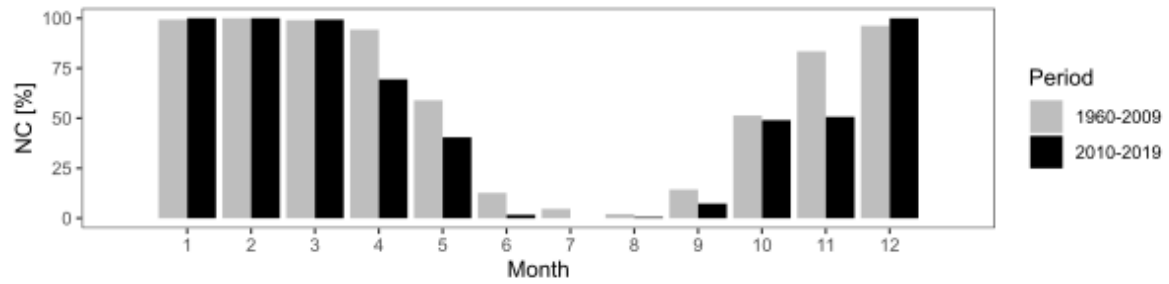

Figure 3.10 *Comparison of the 2010–2019 average monthly Nivometric Coefficient (NC) calculated at the glacier's mean elevation with the 50-year average between 1960 and 2009.*

Table 3.4 *Accumulation and ablation season temperature and precipitation in the 2010–2019 decade, compared to the 50-year means. Rain and snow fractions of total precipitation are also compared. Temperature is extrapolated at the mean elevation of the Montasio Glacier applying monthly-variable gradients to the Pontebba weather station data. Precipitation data from the same station are not extrapolated at the glacier's elevation, but are partitioned into liquid and solid fractions using extrapolated temperature.*

	Accumulation Season (November–April)			**Ablation Season (May–October)**		
	1960–2009	2010–2019	2010–2019 anomaly	1960–2009	2010–2019	2010–2019 anomaly
Temperature (°C)	−3.89	−2.10	+1.79	6.60	8.23	+1.63
Precipitation (mm)	750	743	−1%	1072	1028	−4%
Rain (mm)	59 (8%)	146 (20%)	+147%	808 (75%)	836 (81%)	+3%
Snow (mm)	692 (92%)	597 (80%)	−14%	263 (25%)	192 (19%)	−27%

3.6 Uncertainty Assessment

The accuracy of DEMs used in this work was assessed over stable areas in proximity to the glacier, calculating elevation differences between individual DEMs and the reference 2013 TLS DEM (Section 3.4.1). The mean of elevation differences ranges from −0.24 to +0.08 m, and averages −0.01 m. The standard deviation of elevation differences ranges from 0.04 to 0.38 m, with a mean value of 0.17 m (Table 3.5).

Table 3.5 *Statistics of elevation differences calculated among individual DEMs and the reference 2013 TLS DEM over stable area in proximity to the glacier.*

DEM (Year)	Mean	St dev
2006	−0.01	0.31
2010	−0.24	0.04
2011	0.08	0.11
2012	0.04	0.06
2013	-	-
2014	−0.09	0.10
2015	0.00	0.38
2016	0.02	0.18
2017	0.04	0.16
2018	0.06	0.15
2019	0.04	0.16
Mean	−0.01	0.17

The accuracy in geodetic mass balance calculations was evaluated comparing pairs of consecutives surveys, and was assessed over stable areas in proximity to the glacier, using the same procedure described above for individual DEMs. The standard deviation of elevation differences ranges from 0.06 to 0.47 m, (mean value of 0.20 m), which, multiplied by the density used in mass balance calculations, yields a range between 0.05 and 0.38 m w.e. yr^{-1} in geodetic mass balance calculations for single years (mean value of 0.15 m w.e. yr^{-1}). The mean elevation difference in stable areas ranged between −0.49 and +0.32 m (mean value of −0.01 m), and was removed from the raw elevation change calculated in the glacier area, prior to mass balance calculations. The residual error is generally smaller than 0.10 m w.e. yr^{-1} (Table 3.3), with the exception of the 2015 and 2016 mass balance years. The larger error in these two years is due to the 2015 SfM DEM, which is affected by a higher uncertainty and a lower spatial coverage caused by the presence of recent snow at the time of the SfM survey (Figure 3.2).

In this work we have compared mass balance results obtained using the geodetic and the glaciological methods (Table 3.3, Figure 3.4). Even if the two methods can give rather different results at the local scale [59], the geodetic method is widely used in glacier-wide reanalyses and validation of mass balance series obtained with the glaciological method [60], and for assessments

of glacier mass balance at the regional or mountain-range scale [7,8,61,62]. Our comparison serves to highlight possible macro differences between the response of the Montasio Glacier and the average response of glaciers in the European Alps, which far outweigh discrepancies due to the measurement methods.

The uncertainty in surface velocities was estimated evaluating the residual displacement of test points located on stable terrain outside the glacier. The residual errors in horizontal displacements are 0.03, 0.04, and 0.07 m yr^{-1} for the periods 2010–2013, 2013–2017, and 2017–2019, respectively. Corresponding errors for the vertical component of displacements are −0.04, −0.04, and 0.05 m yr^{-1}.

The directional error looks random and not systematic (Figure 3.7), with the possible exception of a small area of the frontal moraine, in contact with the glacier and possibly in active deformation due to the melt out of its ice core. The surface displacement could not be assessed in the upper part of the glacier, due to the presence of snow and firn and due to the absence of detectable features (e.g., crevasses, seracs, and moulins).

The exact position of the lower margins of the glacier is hard to establish, because of the thick debris mantle that covers the ablation area. For this reason, it is not possible to map the front variations, even at the decadal time scale, and we decided to keep fixed the lower margin of the glacier because there were no clear indications of advance or retreat. Moreover, the local morphology and the latest DoDs (Figure 3.3) suggest that the glacier front is stationary. For the same reasons we avoided analyzing changes in glacier area, which have been of minor importance and limited to the upper accumulation area.

The homogeneity tests revealed that the temperature data series of Pontebba is of good quality, with only two short inhomogeneous periods: the first between 1 June 1984 and 31 January 1987 (correction applied −0.70 °C), and the second between 1 January 2017 and 31 December 2019 (correction applied +0.42 °C). The detected inhomogeneities in the precipitation series were smaller than 5%, and therefore we considered them negligible and assumed homogeneous the entire 60-year period analyzed.

3.7 Discussion

The results of this study provide quantitative confirmation to our first observations on the current peculiar behavior of the Montasio Glacier, and on the hypothesized relationship between atmospheric changes and glacier response, based on preliminary investigations conducted between

2009 and 2011 [17]. The comparison with the sample of Alpine reference glaciers, in the period from 2006 to 2019, clearly shows how the Montasio Glacier has been much less impacted by the present warm phase, at least until now (Figure 3.4, Table 3.3). Even taking into consideration the possible underestimation of alpine-wide mass balance using few reference glaciers [63], the mass loss rate of the Montasio Glacier remains of an order of magnitude lower than the rate of −0.87 ± 0.07 m w.e. yr^{-1} recently estimated for all the glaciers in the Alps and Pyrenees, in the period from 2006 to 2016 [64].

In the highly scattered response of smaller glaciers to the climatic conditions of the last decades, the Montasio Glacier likely stands among ice bodies that are closer to balanced-budget conditions, taking advantage of a lower climatic sensitivity and/or negative feedbacks during deglaciation. Similar results showing an increasing control of local topography, and even a possible evolution towards steady-state conditions, have been reported by Carrivick et al. (2015) [65] for the Eastern Alps, Colucci (2016) [66] for the Julian Alps, and Scotti and Brardinoni (2018) [67] for the Val Viola in the Central Alps. The possible survival of avalanche-fed glaciers at low elevation to substantial atmospheric warming has been also suggested by Huss and Fischer (2016) [3], who modelled the climatic sensitivity of 1133 very small glaciers in the Swiss Alps. Outside the European Alps, similar results have been found, for example, by Dahl and Nesje (1992) [68] in Western Norway, and Debeer and Sharp (2009) [13] for the Canadian Rockies. Other studies have reported a contrasting behavior, with the smallest glaciers showing the highest vulnerability [e.g. 9,69–71]. However, these results are averaged over a large number of small glaciers, with characteristics that are different from the Montasio Glacier. Interesting results have been reported by Bhambri et al. (2011) [72], who documented low area loss rates between 1968 and 2006 for glaciers having the lowest mean elevation in the Garhwal Himalaya, India. This suggests that the same factors enabling glacier existence at low elevation (shadowing, enhanced snow accumulation, debris cover, or their combinations) are possibly responsible of a smaller imbalance in the analyzed period.

The presented series of annual balances, quite rare for this type of glaciers, is now sufficiently long to investigate quantitatively the role of different climatic variables in the glacier's mass balance. The high variability of meteorological conditions in the investigated period (Figure 3.9) helped in this regard. A Spearman's correlation analysis between annual balance and annual/seasonal meteorological variables (air temperature, total/liquid/solid precipitation, and NCs), suggests that the annual amount of solid precipitation is a major control on mass balance ($r = 0.88$, $p < 0.005$), followed by the solid precipitation amount in the accumulation season ($r = 0.73$, $p < 0.05$) and by

the total amount of precipitation in the accumulation season ($r = 0.68$, $p < 0.05$). The mean temperature in the ablation season is not significantly correlated with mass balance ($r = -0.52$, $p = 0.15$). These results highlight the importance of snow accumulation for this avalanche-fed and heavily debris-covered glacier, not only in the accumulation season, but also in the months of May and October, which regulate the length of the ablation period.

The high sensitivity to snow accumulation is remarkable, especially in periods of rapid deglaciation, when mass balance generally correlates extremely well with summer temperature and shows no correlation with winter accumulation [73]. This strong dependence on solid precipitation is related to the high "avalanche ratio" (i.e., the ratio between the total area susceptible to avalanche, which is defined as slopes >30° leading directly onto the glacier, and the total glacier area [74]), which is 2.9 for the Montasio Glacier. This high ratio leads to a considerable increase in snow accumulation on the glacier surface, which can be estimated in about 300% compared to sites at the same elevation, unaffected by avalanches [17]. Our observations indicate that the glacier is primarily fed by frequent and small avalanches of loose snow, which accumulate mostly in the upper half of the glacier, thereby potentially doubling the avalanche ratio. The concentration of large amounts of snow in a small area has a twofold effect. The first is a reduction of the contact surface between snow and atmosphere, where the largest part of ablation takes place. The second effect is a manifold multiplication of the snow accumulation anomaly, compared to areas unaffected by avalanches. A solid precipitation anomaly of +0.1 m w.e., for example, becomes +0.4 m w.e. (+0.7 m considering only the upper half of the glacier), thus representing a relevant energy sink for ablation processes compared to areas without snow redistribution.

These considerations are valid also for negative precipitation anomalies and provide a key to the interpretation of the high sensitivity of this glacier to precipitation variability and accumulation processes, and of the lower sensitivity to air temperature and ablation processes. Besides air temperature variability, the summer ablation is largely dependent on the extent and thickness of the firn cover. In case of warm summers, a thick and widespread firn cover exposes the glacier to large mass loss, as occurred in 2015 after the highly positive 2014 mass balance year (Figures 3.3 and 3.4). Once the firn is depleted, such as in the last four years, the 2–3 m thick debris mantle that covers the underlying ice strongly limits ablation, and significantly dampens the inter-annual variability of mass balance and its sensitivity to air temperature. In the observed period, the best example for this behavior came from 2018, when the mass balance was slightly positive in spite of a very warm ablation season (the warmest since 1960). The thick avalanche deposits due to the above-average winter snowfalls (Figure 3.9), concentrated in a small accumulation area (Figure

3.3), slightly exceeded the mass losses in the ablation area, which were mitigated by: (i) the small extent of the 2017 firn area, exposed to ablation for a short period, and (ii) the debris insulation over a large portion of the glacier (Figures 3.2 and 3.3). This mass balance year highlights also why the glacier currently exhibits such a low balanced-budget AAR (AAR_0 ~ 0.30).

The glacier entered a phase of prevailing negative mass balance after 2014, when there was a gradual expansion of the area covered by debris (Figures 3.2 and 3.5), caused by the shrinking of the accumulation area and by the surface accumulation of debris contained in firn, following melt. In addition, we observed the formation of new deposits of fine-grained debris in the upper half of the glacier, caused by rockfalls. In 2016 one of these events occurred at the beginning of the melt season, covering a considerable portion of the glacier (see the positive elevation changes in the upper half of the glacier in Figure 3.3) and leading to the incorporation of firn lenses in the glacier body. The alternating layers of snow, firn, and debris retrieved in the upper zone of the glacier by the geophysical investigations carried out in 2010 [17] likely originate from events similar to this one observed in 2016.

Overall, the sediment budget of the glacierized area looks positive. Debris supply is ensured by the continuous action of cryo-clastism and rock falls, and is abundant in comparison to glacier transportation efficiency, due to the high ratio between the area of debris-providing rock walls and the glacier area [15,75]. Debris evacuation by glacier transport outside the LIA and 1920s moraines has become negligible since the first decades of the 20th Century, and at present these moraines have a damming effect on debris transported by glacifluvial processes. In the investigated time span, there were only low-magnitude debris flows, which locally redistributed small amounts of debris within the glacier area. High-magnitude events, comparable to those reported in 1993 and 1999 by Chiarle et al. (2007) [76], and responsible of large sediment erosion, where completely absent. The resulting increase in area and thickness of the debris mantle is an important negative feedback that is contributing to the preservation of the Montasio Glacier.

Even if a short reaction/response time is expected for this small and steep ice body, subject to high mass balance gradients [77], the phase with a positive cumulated mass balance between 2006 and 2014 was likely too short or discontinuous to lead sizeable variations in the front area. The variations in surface displacement rates described in Section 3.4.3, between 2010 and 2019, show that the lower half of the glacier tends towards stagnation and stationary thinning. This tendency is more evident in the central-western part of the glacier. The higher residual activity of the eastern portion is documented by its smaller deceleration, and by vertical displacement rates that became closer to zero, possibly related to the phase of temporary mass gain mentioned above. Nevertheless,

the number of sinkholes has clearly increased also in this part of the front, suggesting low residual ice thickness beneath the debris layer.

Even if the measured surface displacement rates are typical of rock glaciers, the Montasio Glacier does not show the progressive transition from glacial to periglacial processes described for other small, avalanche-fed, and debris-covered glaciers in the Eastern Italian Alps [21,23,78,79]. These sites are originating rock glaciers or glacial-permafrost composite landforms, where the former accumulation area is downwasting, and the lower ablation area is evolving under permafrost conditions and generating active rock glaciers. We tend to exclude that such a transition is taking place on the Montasio Glacier, which completely lacks morphological features typical of active rock glaciers, such as transverse ridges and furrows, or a steep and advancing front. The limiting factors for a similar evolution of the Montasio Glacier are still poorly know, but are probably related to the lack of permafrost conditions (due to the low elevation, high snow accumulation, and absence of open-work deposits [80]), and to the residual activity of the glacier.

Outlining the possible future evolution of the Montasio Glacier, and of other ice bodies with similar characteristics, is not straightforward. Even if the presented observation series is rare for its length, further investigations are required to better understand how the climatic sensitivity of this glacier changes in the long term. As highlighted in this work, there is an important role played by the debris cover, which is a key negative feedback that acts to preserve the glacier remnants. Our results confirm a complex relationship between the glacier mass balance and the extent of the debris-covered area, which can change dramatically in the short term due to the wide fluctuations of the firn cover. However, additional investigations are required to highlight how the debris thickness and areal extent evolve in the long term, together with other important feedbacks associated with snow accumulation (e.g., the avalanche ratio), and ablation (e.g., the terrain shadowing). Effects from permafrost degradation in debris cover dynamics should be also taken into account in these studies, because the permafrost index map published by Boeckli et al. (2012) [80] indicates the possible presence of permafrost in the rock walls above the glacier.

3.8 Conclusions

The results of our investigations on the Montasio Glacier, spanning the period from 2006 to 2019, highlight how this glacier is currently subject to a low degree of imbalance, which is about one order of magnitude lower compared to the reference mass balance glaciers of the European Alps.

The cumulative mass balance has been even positive until 2014, thanks to snow-rich accumulation seasons, which occurred in particular in 2009 and 2014.

This work provides statistically significant evidence of the dominant role played by solid precipitation in regulating the annual mass balance of this type of glacier, which benefits from thick and spatially concentrated snow accumulation by avalanches. These deposits are effectively shadowed by the same rock walls that contributes avalanches, and which also release debris (mainly cryo clasts) that accumulate over the glacier.

The progressive shrinking and thinning of the glacier, in association with the ongoing debris deposition and the low effectiveness of glacifluvial erosion, has led to the formation of a widespread and thick debris cover, in particular over the lower half of the glacier. This is the main negative feedback affecting the mass balance evolution of the Montasio Glacier, which is currently characterized by a low sensitivity to regional temperature fluctuations. Together with the thick avalanche deposits, the debris cover is also responsible for the very low balanced-budget AAR, around 0.30, which is among the lowest reported in the literature [18,20,81,82].

The progressive accumulation, thickening, and reworking of the debris cover, and the reduction in the climatic sensitivity of the glacier, are long-term processes that could not be fully investigated in the time span of our recent investigations. For this reason, a detailed reconstruction of the geometric variations and surface evolution of the Montasio Glacier before 2006 is in progress, and will be extended to the first direct observations at the beginning of the 20th Century. This additional study will enable an even better understanding of how the geometry and climatic sensitivity of this type of glaciers respond to sustained atmospheric changes, in order to outline their possible evolution in the next decades. Moreover, they will serve to clarify why some glacierized alpine environments shift towards periglacial/paraglacial conditioning, whereas others (such as the Montasio) preserve a dominant glacial conditioning.

AUTHOR CONTRIBUTIONS

Conceptualization, L.C., F.C. and G.D.F.; Methodology, L.C., S.C., L.P. and J.D.M.; Validation, L.C., S.C., L.P. and J.D.M.; Formal analysis, L.P., S.C. and J.D.M.; Data curation, L.C., L.P., S.C., D.M. and J.D.M.; Writing—original draft preparation, J.D.M. and L.C.; Writing—review and editing, L.C., F.C., L.P., S.C., G.D.F., D.M. and J.D.M.; Visualization, J.D.M. and L.C.; Supervision, L.C. and F.C.; Funding acquisition, F.C., G.D.F. and L.C.

FUNDING

This study was carried out in the framework of two PhD studentships funded by the Universities of Udine and Trieste (Department of Agricultural, Food, Environmental and Animal Sciences—DI4A and Department of Life Sciences—DSV), and a PhD studentship funded by the University of Padova (Department of Land, Environment, Agriculture and Forestry—TeSAF). The study was also funded by (i) the Italian research program MIUR PRIN 2010–2011 "Response of Morphoclimatic System Dynamics to Global Changes and Related Geomorphological Hazards" (local and national coordinators G. Dalla Fontana and C. Baroni); (ii) the research program MIUR PRIN 2010–2011 20104ALME4-ITSE (local and national coordinators F. Cazorzi and M.A. Lenzi); (iii) the research program MIUR PRIN 2008 "La degradazione della criosfera nelle Alpi centro orientali. Analisi delle trasformazioni in atto attraverso lo studio di aree campione e di unità morfologiche chiave" (coordinator A. Carton); (iv) the University of Padova Junior Research Grant: "Sperimentazione di tecniche di rilievo LiDAR e TLS per lo studio della criosfera alpina".

ACKNOWLEDGMENTS

The authors would like to thank the OSMER Office (Osservatorio Meteorologico Regionale) of the Autonomous Region of Friuli Venezia Giulia for providing access to regional meteorological datasets, and in particular Andrea Cicogna and Roberto Medeossi for their availability. A special thanks to the personnel of the "Direzione Centrale Risorse Agroalimentari, Forestali e Ittiche, Servizio Foreste e Corpo Forestale" office of the Autonomous Region of Friuli Venezia Giulia for their support during field activities. Thanks as well to Alberto Carton, Alberto Guarnieri, Simone Calligaro and Giovanni Andrea Baldassi, (University of Padova), Riccardo De Infanti and Giacomo Blasone (University of Udine) for their contribution during field activities and preliminary analyses. The authors would like to thank Bernhard Zagel for the updated data of Stubacher Sonnblickkees.

Conflicts of Interest: The authors declare no conflict of interest.

REFERENCES

1. Pfeffer, W.T.; Arendt, A.A.; Bliss, A.; Bolch, T.; Cogley, J.G.; Gardner, A.S.; Hagen, J.O.; Hock, R.; Kaser, G.; Kienholz, C.; et al. The randolph glacier inventory: A globally complete inventory of glaciers. *J. Glaciol.* **2014**, *60*, 537–552, doi:10.3189/2014JoG13J176.
2. Paul, F.; Kääb, A.; Maisch, M.; Kellenberger, T.; Haeberli, W. Rapid disintegration of alpine glaciers observed with satellite data. *Geophys. Res. Lett.* **2004**, *31*, doi:10.1029/2004GL020816.
3. Huss, M.; Fischer, M. Sensitivity of very small glaciers in the swiss alps to future climate change. *Front Earth Sci.* **2016**, *4*, 1–17, doi:10.3389/feart.2016.00034.
4. Paul, F. Changes in glacier area in Tyrol, Austria, between 1969 and 1992 derived from landsat 5 thematic mapper and Austrian glacier inventory data. *Int. J. Remote. Sens.* **2002**, *23*, 787–799, doi:10.1080/01431160110070708.
5. Lambrecht, A.; Kuhn, M. Glacier changes in the Austrian alps during the last three decades, derived from the new Austrian glacier inventory. *Ann. Glaciol.* **2007**, *46*, 177–184, doi:10.3189/172756407782871341.
6. Andreassen, L.M.; Paul, F.; Kääsignb, A.; Hausberg, J.E. Landsat-derived glacier inventory for Jotunheimen, Norway, and deduced glacier changes since the 1930s. *Cryosphere* **2008**, *2*, 131–145, doi:10.5194/tc-2-131-2008.
7. Paul, F.; Haeberli, W. Spatial variability of glacier elevation changes in the Swiss Alps obtained from two digital elevation models. *Geophys. Res. Lett.* **2008**, *35*, 1–5, doi:10.1029/2008GL034718.
8. Carturan, L.; Filippi, R.; Seppi, R.; Gabrielli, P.; Notarnicola, C.; Bertoldi, L.; Paul, F.; Rastner, P.; Cazorzi, F.; Dinale, R.; et al. Area and volume loss of the glaciers in the ortles-cevedale group (Eastern Italian alps): Controls and imbalance of the remaining glaciers. *Cryosphere* **2013**, *7*, 1339–1359, doi:10.5194/tc-7-1339-2013.
9. Schmidt, S.; Nüsser, M. Changes of high altitude glaciers from 1969 to 2010 in the Trans-Himalayan Kang Yatze Massif, Ladakh, Northwest India. *Arct. Antarct. Alp. Res.* **2012**, *44*, 107–121, doi:10.1657/1938-4246-44.1.107.
10. López-Moreno, J.I.; Nogués-Bravo, D.; Chueca-Cía, J.; Julían-Andrés, A. Change of topographic control on the extent of cirque glaciers since the little ice age. *Geophys. Res. Lett.* **2006**, *33*, 1–5, doi:10.1029/2006GL028204.
11. Chueca, J.; Julián, A.; López-Moreno, J.I. Recent evolution (1981–2005) of the Maladeta glaciers, pyrenees, Spain: Extent and volume losses and their relation with climatic and topographic factors. *J. Glaciol.* **2007**, *53*, 547–557, doi:10.3189/002214307784409342.
12. Kuhn, M. The mass balance of very small glaciers. *Z. für Gletsch. Und Glazialgeol.* **1995**, *31*, 171–179.
13. DeBeer, C.M.; Sharp, M.J. Topographic influences on recent changes of very small glaciers in the Monashee Mountains, British Columbia, Canada. *J. Glaciol.* **2009**, *55*, 691–700, doi:10.3189/002214309789470851.
14. Grunewald, K.; Scheithauer, J. Europe's southernmost glaciers: Response and adaptation to climate change. *J. Glaciol.* **2010**, *56*, 129–142, doi:10.3189/002214310791190947.

15. Zemp, M.; Kääb, A.; Hoelzle, M.; Haeberli, W. GIS-based modelling of glacial sediment balance. *Z. Fur Geomorphol. Suppl.* **2005**, *138*, 113–129, doi:10.5167/uzh-40580.

16. Benn, D.; Evans, D.J.A. *Glaciers & Glaciation*, 2nd ed.; Hodder Education: London, UK, 2010; ISBN 978 0 340 905791.

17. Carturan, L.; Baldassi, G.A.; Bondesan, A.; Calligaro, S.; Carton, A.; Cazorzi, F.; Dalla Fontana, G.; Francese, R.; Guarnieri, A.; Milan, N.; et al. Current behaviour and dynamics of the lowermost Italian Glacier (Montasio occidentale, Julian Alps). *Geogr. Ann. Ser. A Phys. Geogr.* **2013**, *95*, 79–96, doi:10.1111/geoa.12002.

18. Benn, D.I.; Lehmkuhl, F. Mass balance and equilibrium-line altitudes of glaciers in high-mountain environments. *Quat. Int.* **2000**, *65–66*, 15–29, doi:10.1016/S1040-6182(99)00034-8.

19. Cogley, J.G.; Hock, R.; Rasmussen, L.A.; Arendt, A.A.; Bauder, A.; Braithwaite, R.J.; Jansson, P.; Kaser, G.; Möller, M.; Nicholson, L.; et al. In *Glossary of Glacier Mass Balance and Related Terms, IHP-VII Technical Documents in Hydrology No.86, IACS Contribution No. 2*; UNESCO-IHP: Paris, France, 2011.

20. Kern, Z.; László, P. Size specific steady-state accumulation-area ratio: An improvement for equilibrium-line estimation of small palaeoglaciers. *Quat. Sci. Rev.* **2010**, *29*, 2781–2787, doi:10.1016/j.quascirev.2010.06.033.

21. Seppi, R.; Zanoner, T.; Carton, A.; Bondesan, A.; Francese, R.; Carturan, L.; Zumiani, M.; Giorgi, M.; Ninfo, A. Current transition from glacial to periglacial processes in the Dolomites (South-Eastern Alps). *Geomorphology* **2014**, *228*, 71–86, doi:10.1016/j.geomorph.2014.08.025.

22. Bosson, J.B.; Lambiel, C. Internal structure and current evolution of very small debris-covered glacier systems located in alpine permafrost environments. *Front Earth Sci.* **2016**, *4*, doi:10.3389/feart.2016.00039.

23. Seppi, R.; Carturan, L.; Carton, A.; Zanoner, T.; Zumiani, M.; Cazorzi, F.; Bertone, A.; Baroni, C.; Salvatore, M.C. Decoupled kinematics of two neighbouring permafrost creeping landforms in the Eastern Italian Alps. *Earth Surf. Process. Landf.* **2019**, *44*, 2703–2719, doi:10.1002/esp.4698.

24. Serandrei Barbero, R.; Rabagliati, R.; Zecchetto, S. Analisi delle misure alle fronti dei ghiacciai delle Apli Giulie e correlazioni con i dati climatici. *Geogr. Fis. Din. Quat.* **1989**, *12*, 139–149.

25. Carturan, L.; Seppi, R. Comparison of current behavior of three glaciers in western Trentino (Italian Alps)-evoluzione recente di tre ghiacciai nel Trentino occidentale (Alpi Italiane). In Proceedings of the Geoitalia 2009 Congress. EPITOME, Rimini, Italy, 9–11 September 2009;Volume 3, p. 298.

26. Colucci, R.R.; Guglielmin, M. Precipitation-temperature changes and evolution of a small glacier in the southeastern European Alps during the last 90 years. *Int. J. Climatol.* **2015**, *35*, 2783–2797, doi:10.1002/joc.4172.

27. Passalacqua, P.; Belmont, P.; Staley, D.M.; Simley, J.D.; Arrowsmith, J.R.; Bode, C.A.; Crosby, C.; DeLong, S.B.; Glenn, N.F.; Kelly, S.A.; et al. Analyzing high resolution topography for advancing the understanding of mass and energy transfer through landscapes: A review. *Earth-Sci. Rev.* **2015**, *148*, 174–193, doi:10.1016/j.earscirev.2015.05.012.

28. Lague, D. *Terrestrial Laser Scanner Applied to Fluvial Geomorphology*. In Developments in Earth Surface Processes, 1st ed.; Elsevier B.V.: Amsterdam, The Netherlands., 2020; Volume 23, p. 231-254, ISBN 9780444641779.

29. Eltner, A.; Sofia, G. *Structure from Motion Photogrammetric Technique*. In Developments in Earth Surface Processes, 1st ed.; Elsevier B.V.: Amsterdam, The Netherlands., 2020; Volume 23, p- 1-24, ISBN 9780444641779.

30. Tarolli, P.; Arrowsmith, J.R.; Vivoni, E.R. Understanding earth surface processes from remotely sensed digital terrain models. *Geomorphology* **2009**, *113*, 1–3, doi:10.1016/j.geomorph.2009.07.005.

31. Fischer, M.; Huss, M.; Kummert, M.; Hoelzle, M. Application and validation of long-range terrestrial laser scanning to monitor the mass balance of very small glaciers in the Swiss alps. *Cryosphere* **2016**, *10*, 1279–1295, doi:10.5194/tc-10-1279-2016.

32. Piermattei, L.; Carturan, L.; Guarnieri, A. Use of terrestrial photogrammetry based on structure-from-motion for mass balance estimation of a small glacier in the Italian alps. *Earth Surf. Process. Landf.* **2015**, *40*, 1791–1802, doi:10.1002/esp.3756.

33. Piermattei, L.; Carturan, L.; De Blasi, F.; Tarolli, P.; Dalla Fontana, G.; Vettore, A.; Pfeifer, N. Suitability of ground-based SfM-MVS for monitoring glacial and periglacial processes. *Earth Surf. Dyn.* **2016**, *4*, 425–443, doi:10.5194/esurf-4-425-2016.

34. Cucchiaro, S.; Cavalli, M.; Vericat, D.; Crema, S.; Llena, M.; Beinat, A.; Marchi, L.; Cazorzi, F. Monitoring topographic changes through 4D-structure-from-motion photogrammetry: application to a debris-flow channel. *Environ. Earth Sci.* **2018**, *77*, 632, doi:10.1007/s12665-018-7817-4.

35. Piermattei, L.; Karel, W.; Vettore, A.; Pfeifer, N. Panorama image sets for terrestrial photogrammetric surveys. *ISPRS Ann. Photogramm. Remote Sens. Spat. Inf. Sci.* **2016**, *III–5*, 159–166, doi:10.5194/isprsannals-iii-5-159-2016.

36. Cucchiaro, S.; Maset, E.; Fusiello, A.; Cazorzi, F.; Weiss, V.E. 4D-Sfm photogrammetry for monitoring sediment dynamics in a debris-flow catchment : Software testing and results comparison. *Int. Arch. Photogramm. Remote. Sens. Spat. Inf. Sci.* **2018**, *XLII*, 4–7.

37. Loye, A.; Jaboyedoff, M.; Isaac Theule, J.; Liébault, F. Headwater sediment dynamics in a debris flow catchment constrained by high-resolution topographic surveys. *Earth Surf. Dyn.* **2016**, *4*, 489–513, doi:10.5194/esurf-4-489-2016.

38. World Glacier Inventory (WGI) Available online: https://nsidc.org/ (accessed on 26 March 2020).

39. Haeberli, W.; Bösch, H.; Scherler, K.; Østrem, G.; Wallén, C.C. *World Glacier Inventory; Status 1988. A Contribution to the Global Environ-Ment Monitoring System (GEMS) and the International Hydrological Programme*; International Association of Hydrological Sciences; lARS Press: Nairobi, Kenya-United Nation, 1989; ISBN 92-807-1217-9.

40. Cucchiaro, S.; Maset, E.; Cavalli, M.; Crema, S.; Marchi, L.; Beinat, A.; Cazorzi, F. How does co-registration affect geomorphic change estimates in multi-temporal surveys? *GIScience Remote Sens.* **2020**, *57*, 611–632, doi:10.1080/15481603.2020.1763048.

41. Agisoft PhotoScan.

42. Pfeifer, N.; Mandlburger, G.; Otepka, J.; Karel, W. OPALS-A framework for airborne laser scanning data analysis. *Comput. Environ. Urban Syst.* **2014**, *45*, 125–136, doi:10.1016/j.compenvurbsys.2013.11.002.

43. Sorge, E. Glaziologische untersuchungen in eismitte-glaciological research at eismitte. *Wiss.-Ergeb. Dtsch. Groenl. Exped. Alfred Wegener.* **1935**, *3*, 270.

44. Ai, S.; Yan, B.; Wang, Z.; Yan, M. A decadal record of inter-annual surface ice flow from pedersenbreen, svalbard (2005-15). *Polar Sci.* **2019**, *22*, doi:10.1016/j.polar.2019.100485.

45. World Meteorological Organization. *Climate Observations and Climate Data Management Guidelines*; WMO: Geneva, Switzerland, 2009.

46. Baldassi, G.A. *Analisi su Base Climatologica Delle Variazioni Storiche Del Ghiacciaio Del Montasio (FVG);* MSC Thesis, University degli Stud di Padova, Padova, Italy, 2010..

47. Schwarb, M. The Alpine Precipitation Climate: Evaluation of a High-Resolution Analysis Scheme Using Comprehensive Rain-Gauge Data. Ph.D. Thesis, ETH Zurich, Zurich, Switzerland, 2000.

48. Klein Tank, A.M.G.; Wijngaard, J.B.; Können, G.P.; Böhm, R.; Demarée, G.; Gocheva, A.; Mileta, M.; Pashiardis, S.; Hejkrlik, L.; Kern-Hansen, C.; et al. Daily dataset of 20th-century surface air temperature and precipitation series for the European climate assessment. *Int. J. Climatol.* **2002**, *22*, 1441–1453, doi:10.1002/joc.773.

49. European Climate Assessment & Dataset. Available online: https://www.ecad.eu/ (accessed on 20 March 2020).

50. Zemp, M.; Gärtner-Roer, I.; Nussbaumer, S.U.; Bannwart, J.; Rastner, P.; Paul, F.; Hoelzle, M. *WGMS 2020. Global Glacier Change Bulletin No. 3 (2016-2017)*; Publisher: Zurich, Switzerland, 2020.

51. World Glacier Monitoring Service, W. WGMS online dataset. Available online: https://wgms.ch/latest-glacier-mass-balance-data/ (accessed on 5 June 2020).

52. Zagel, B.; Slupetzky, H. LTER Site Stubacher Sonnblickkees, Mass Balance. Available online: https://deims.org/f904bf5e-60a5-4d0d-b8b9-6ca009fbcb9f (accessed on 22 June 2019).

53. Observatoire des Sciences de l'Univers de Grenoble, O. Service d'Observation GLACIOCLIM. Available online: https://glacioclim.osug.fr/Donnees-des-Alpes (accessed on 6 July 2020).

54. Bavarian Academy of Sciences and Humanities Website. Available online: https://geo.badw.de/vernagtferner-digital/massenbilanz.html (accessed on 27 July 2020).

55. Rotach, M.; Prinz, R. *Hintereis-und Kesselwandferner Massenhaushaltsstudien, Abschlussbericht über das Haushaltsjahr 2018/19*; Publisher: Innsbruck, Austria, 2019.

56. Baroni, C.; Bondesan, A.; Luca, C.; Chiarle, M. Eds.; Preliminary Results on Antarctic Albedo from Remote Sensing Observations *Geogr. Fis. Dinam. Quat*. **2019**, *42*, doi:10.4461/ GFDQ.2019.42.15.

57. Serrano, E.; González-trueba, J.J.; Sanjosé, J.J.; Del río, L.M. Ice patch origin, evolution and dynamics in a temperate high mountain environment: the jou negro, picos de europa (nw spain). *Geogr. Ann. Ser. A Phys. Geogr.* **2011**, *93*, 57–70, doi:10.1111/j.1468-0459.2011.00006.x.

58. Zemp, M.; Paul, F.; Hoelzle, M.; Haeberli, W. Glacier fluctuations in the European Alps 1850–2000: An overview and spatio-temporal analysis of available data. *Darkening Peaks Glacial Retreat Sci. Soc. Context* **2008**, 152–167, doi:10.5167/uzh-9024.

59. Fischer, A. Comparison of direct and geodetic mass balances on a multi-annual time scale. *Cryosph.* **2011**, *5*, 107–124, doi:10.5194/tc-5-107-2011.

60. Zemp, M.; Thibert, E.; Huss, M.; Stumm, D.; Rolstad Denby, C.; Nuth, C.; Nussbaumer, S.U.; Moholdt, G.; Mercer, A.; Mayer, C.; et al. Reanalysing glacier mass balance measurement series. *Cryosph.* **2013**, *7*, 1227–1245, doi:10.5194/tc-7-1227-2013.

61. Abermann, J.; Lambrecht, A.; Fischer, A.; Kuhn, M. Quantifying changes and trends in glacier area and volume in the Austrian Ötztal Alps (1969-1997-2006). *Cryosph.* **2009**, *3*, 205–215, doi:10.5194/tc-3-205-2009.

62. Fischer, M.; Huss, M.; Hoelzle, M. Surface elevation and mass changes of all swiss glaciers 1980–2010. *Cryosphere* **2015**, *9*, 525–540, doi:10.5194/tc-9-525-2015.

63. Sommer, C.; Malz, P.; Seehaus, T.C.; Lippl, S.; Zemp, M.; Braun, M.H. Rapid glacier retreat and downwasting throughout the European Alps in the early 21st century. *Nat. Commun.* **2020**, *11*, 3209, doi:10.1038/s41467-020-16818-0.

64. Zemp, M.; Huss, M.; Thibert, E.; Eckert, N.; McNabb, R.; Huber, J.; Barandun, M.; Machguth, H.; Nussbaumer, S.U.; Gärtner-Roer, I.; et al. Global glacier mass changes and their contributions to sea-level rise from 1961 to 2016. *Nature* **2019**, *568*, 382–386, doi:10.1038/s41586-019-1071-0.

65. Carrivick, J.L.; Berry, K.; Geilhausen, M.; James, W.H.M.; Williams, C.; Brown, L.E.; Rippin, D.M.; Carver, S.J. Decadal-scale changes of the ödenwinkelkees, central austria, suggest increasing control of topography and evolution towards steady state. *Geogr. Ann. Ser. A Phys. Geogr.* **2015**, *97*, 543–562, doi:10.1111/geoa.12100.

66. Colucci, R.R. Geomorphic influence on small glacier response to post-little ice age climate warming: Julian Alps, Europe. *Earth Surf. Process. Landf.* **2016**, *41*, 1227–1240, doi:10.1002/esp.3908.

67. Scotti, R.; Brardinoni, F. Evaluating millennial to contemporary time scales of glacier change in Val Viola, central Italian Alps. *Geogr. Ann. Ser. A Phys. Geogr.* **2018**, *100*, 319–339, doi:10.1080/04353676.2018.1491312.

68. Dahl, S.O.; Nesje, A. Paleoclimatic implications based on equilibrium-line altitude depressions of reconstructed Younger dryas and holocene cirque glaciers in inner Nordfjord, western Norway. *Palaeogeogr. Palaeoclim. Palaeoecol.* **1992**, *94*, 87–97, doi:10.1016/0031-0182(92)90114-K.

69. Kulkarni, A.V.; Bahuguna, I.M.; Rathore, B.P.; Singh, S.K.; Randhawa, S.S.; Sood, R.K.; Dhar, S. Glacial retreat in Himalaya using Indian remote sensing satellite data. *Curr. Sci.* **2007**, *92*, doi:10.1117/12.694004.

70. Winsvold, S.H.; Andreassen, L.M.; Kienholz, C. Glacier area and length changes in Norway from repeat inventories. *Cryosph* **2014**, *8*, 1885–1903, doi:10.5194/tc-8-1885-2014.

71. Schmidt, S.; Nüsser, M. Changes of high altitude glaciers in the trans-himalaya of ladakh over the past five decades (1969–2016). *Geosciences* **2017**, *7*, 27, doi:10.3390/geosciences7020027.

72. Bhambri, R.; Bolch, T.; Chaujar, R.K.; Kulshreshtha, S.C. Glacier changes in the garhwal himalaya, India, from 1968 to 2006 based on remote sensing. *J. Glaciol.* **2011**, *57*, 543–556, doi:10.3189/002214311796905604.

73. Schöner, W.; Auer, I.; Böhm, R. Climate variability and glacier reaction in the Austrian eastern Alps. *Ann. Glaciol.* **2000**, *31*, 31–38, doi:10.3189/172756400781819806.

74. Hughes, P.D. Response of a montenegro glacier to extreme summer heatwaves in 2003 and 2007. *Geogr. Ann. Ser. A Phys. Geogr.* **2008**, *90*, 259–267, doi:10.1111/j.1468-0459.2008.00344.x.

75. Haeberli, W. Factors influencing the distribution of rocky and sedimentary glacier beds-hydraulic effects at the glacier bed and related phenomena. *Mitt. Vers. Für Wasserbau, Hydrol. Und Glaziologie* **1986**, *90*, 48–49.

76. Chiarle, M.; Iannotti, S.; Mortara, G.; Deline, P. Recent debris flow occurrences associated with glaciers in the Alps. *Glob. Planet. Chang.* **2007**, *56*, 123–136, doi:10.1016/j.gloplacha.2006.07.003.

77. Bahr, D.B.; Pfeffer, W.T.; Sassolas, C.; Meier, M.F. Response time of glaciers as a function of size and mass balance: 1. theory. *J. Geophys. Res. Solid Earth* **1998**, *103*, 9777–9782, doi:10.1029/98JB00507.

78. Krainer, K.; Lang, K.; Hausmann, H. Active rock glaciers at croda Rossa/Hohe gaisl, eastern Dolomites (Alto Adige/South Tyrol, Northern Italy). *Geogr. Fis. E Din. Quat.* **2010**, *33*, 25–36.

79. Krainer, K.; Mussner, L.; Behm, M.; Hausmann, H. Multi-disciplinary investigation of an active rock glacier in the sella group (Dolomites; Northern Italy). *Austrian J. Earth Sci.* **2012**, *105*, 48–62.

80. Boeckli, L.; Brenning, A.; Gruber, S.; Noetzli, J. Permafrost distribution in the European Alps: Calculation and evaluation of an index map and summary statistics. *Cryosph* **2012**, *6*, 807–820, doi:10.5194/tc-6-807-2012.

81. Clark, D.H.; Clark, M.M.; Gillespie, A.R. Debris-Covered Glaciers in the Sierra Nevada, California, and their implications for snowline reconstructions. *Quat. Res.* **1994**, *41*, 139–153, doi:10.1006/qres.1994.1016.

82. Kulkarni, A.V. Mass balance of himalayan glaciers using AAR and ELA methods. *J. Glaciol.* **1992**, *38*, 101–104, doi:10.3189/S0022143000009631.

Chapter 4

Century-long multi-source analyses highlight decreasing vulnerability for a small, debris-covered and avalanche-fed glacier in the Eastern Italian Alps

Jessica De Marco [1,2,*], Luca Carturan [3], Eleonora Maset [1], Sara Cucchiaro [1], Domenico Visintini [4], Riccardo De Infanti [1] and Federico Cazorzi [1]

[1] Department of Agricultural, Food, Environmental and Animal Sciences (DI4A), University of Udine, Via Delle Scienze, 206, 33100 Udine, Italy

[2] Department of Life Sciences, University of Trieste (DSV), Via E. Weiss, 2, 34128 Trieste, Italy

[3] Department of Land, Environment, Agriculture and Forestry (TESAF), University of Padova, Viale dell'Università, 16, 35020 Legnaro (Padova)

[4] Polytechnic Department of Engineering and Architecture (DPIA), University of Udine, Via Delle Scienze, 206, 33100 Udine, Italy

* Corresponding author

Under submission

4 Century-long multi-source analyses highlight decreasing vulnerability for a small, debris-covered and avalanche-fed glacier in the Eastern Italian Alps

4.1 Abstract

The very small Montasio Glacier is the lowermost Italian glacier, located in the Eastern Italian Alps. Its recent dynamics show unusual response to climatic changes compared to most alpine glaciers, but it is unclear whether this response is a short- or a long-term characteristic. This work documents changes in elevation, mass balance rate and surface cover in the last century (from 1920 to 2020), primarily through Digital Elevation Model reconstructed from different type of data sources (maps, terrestrial and aerial images, point clouds). Glacier changes are analysed jointly with trends in the most relevant climatic variables.

In the analysed time, the glacier experienced phases of rapid mass loss (1920-1948 and 1982-2006) and phases of small imbalance (1948-1982 and 2006-2020). Whereas the 1948-1982 was a favourable time-window for most glaciers in the Alps, the last fifteen years were characterized by rapid warming and show a clear divergence between the behaviour of the Montasio Glacier and of the rest of Alpine glaciers. A century-long increase in thickness and extent of debris cover explains largely this divergence. Snow-rich winters in recent years also played a role, because this glacier is fed by avalanches and reacts sensitively to changes in solid precipitation. Even in the case of possible decreased snowfalls and increased melt associated to warming temperatures during the next decades, the glacier is not expected to vanish soon, because it will likely survive under thick layers of debris. On the other hand, the results of this study paired with the current distribution of permafrost in the study area suggest that the Montasio Glacier will unlikely evolve into a rock glacier or a glacial-permafrost composite landform.

Keywords: glacier mass balance; glacier fluctuations; very small glaciers; debris-covered glaciers; climate change; geodetic method; Structure from Motion (SfM), retrospective analysis

4.2 Introduction

Glaciers are changing very rapidly in response to climate changes [1] and their high mass loss rate is considered to have the atmospheric global warming as primary driver [2,3]. Indeed, the retreat of worldwide glaciers in the period 1884-1978 was found to be proportional to global warming [4]. A

significant increase in glacier mass loss rates has been observed in the last decades, causing a loss of 9,625 billion tons of ice (27 mm sea-level equivalent) between 1961 and 2016 [5]. Moreover, the glacier ice mass loss rate in the last three decades has been estimated to be 335 billion tons y^{-1}, which is equivalent to almost 1 mm y^{-1} in sea level rise [6].

Even though glacier mass losses are evident at a global scale, very small glaciers show a high variability in their response based on their individual characteristics and topo-climatic controls [7–10]. In the European Alps, for example, very small glaciers that are fed by avalanches and partly covered by debris tend to experience a much smaller imbalance compared to the majority of other glaciers, where avalanche activity and debris cover are negligible [11]. The latter are usually responsive to temperature changes (e.g., 12), while the former ones are more sensitive to precipitation variability [11,13,14], and tend to decouple from regional temperature fluctuations.

The concentration of avalanche snow and debris over receding glaciers represent well know negative feedbacks during deglaciation [15,16], which can affect a large number of ice bodies, especially in high-relief mountain groups with sub-vertical rock walls, such as the Dolomites (Eastern Italian Alps). However, these processes are quantitatively documented for short periods, in recent decades [17–19], whereas long-term studies of these dynamics, at secular time scales, are scarcely available in the literature [20,21]. This is remarkable because they are generally long-term processes, which require observations of sufficient length to be fully investigated and understood.

This paper aims at providing a contribution to the knowledge of these long-term processes, performing a century-long analysis of the behavior and climatic response of the very small Occidentale del Montasio Glacier (Julian Alps, North-East Italy), which is fed by avalanches and has the ablation area covered by debris. Digital Elevation Models (DEMs) were reconstructed from different data sources (maps, aerial photos, terrestrial photos, Terrestrial Laser Scanner-TLS and Aerial Laser Scanner-ALS) and the glacier variations from 1920 to 2020 have been assessed in terms of *i*) elevation changes, *ii*) geodetic mass balance, and *iii*) debris cover and surface characteristics. The results have been discussed in relation to air temperature and precipitations trends in the same observation period.

4.3 The Montasio Glacier

The Occidentale del Montasio Glacier ("Montasio Glacier" hereinafter) lies on the northern side of the Mount Jôf di Montasio (2754 m a.s.l., Italian Julian Alps, Eastern European Alps) between 1860

m and 2050 m a.s.l. (median elevation at 1900 m a.s.l. and mean elevation at 1910 m a.s.l.) and it is the lowermost Italian glacier (Figure 4.1). The glacier is mainly nourished by winter avalanches, which have their deposition zone over the steep and cone-shaped accumulation area, while the ablation area is defined by a gently sloped surface entirely covered by a 2-3 m thick debris layer.

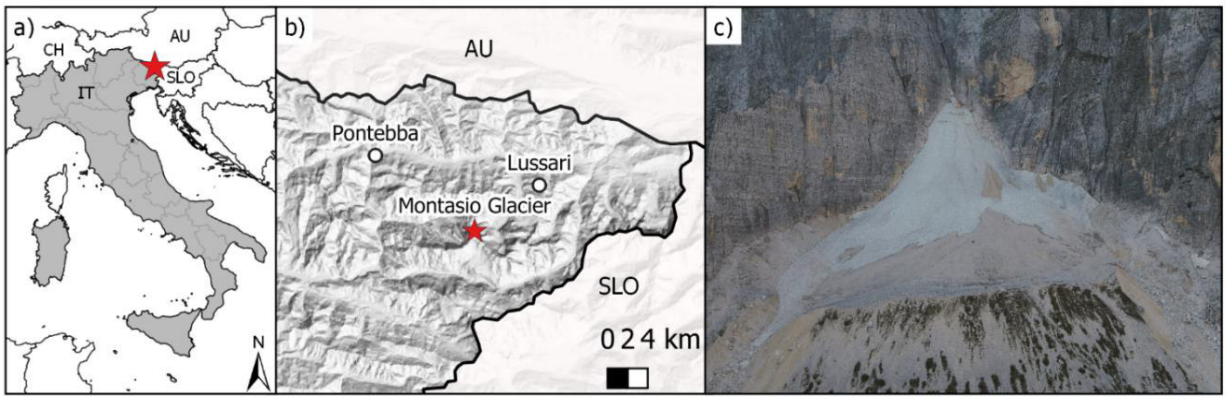

Figure 4.1 *(**a-b**) Geographic location of the Montasio Glacier and of the weather stations in the study area; (**c**) photo of the glacier (Hydrolab-UNIUD research group 28 September 2021).*

The first information source regarding the Montasio Glacier is represented by photos taken by Austrian soldiers during the First World War (WWI, 1914-1918). These photos show the glacier covered by abundant snow, even during summer, and are taken from too far away to enable a quantitative reconstruction of the glacier geometry. Systematic observations date back to the early 1920s, when the glacier was visited and classified as a real 'glacier' for the first time by Ardito Desio [22]. He performed the first length change measurements between 1920 and 1923, documenting a stationarity of the front, whose lower margin was already covered by debris and hard to recognize. In September 1920 Desio produced the first topographic map of the glacier, using a compass [22]. In 1923, Desio reported surface elevation differences due to differential ablation processes in the lower part of the glacier, covered by a debris band.. After these first observations, glacier conditions and length changes have been monitored by different observers from 1938 to 1940 (Manfredi Mazzocca), from 1945 to 1947 (Bruno Martinis and Dino di Colbertaldo), from 1951 to 1989 (Dino and Giancarlo di Colbertaldo, Rossana Serandrei Barbero and Carlo Phoar) and in the 1990s (Rossana Serandrei Barbero). These observations were sparse and discontinuous [23,24]. The observers reported a progressive shrinking of the glacier front, a general thinning of the glacier and an increase in debris coverage, as can be appreciated from their photos (Figure 4.2). The thickness of the debris cover increased with time, making it difficult to recognize the lower

margin of the glacier already in the first decades of observations. In the 1940s the debris thickness at the front was of 0.5 m.

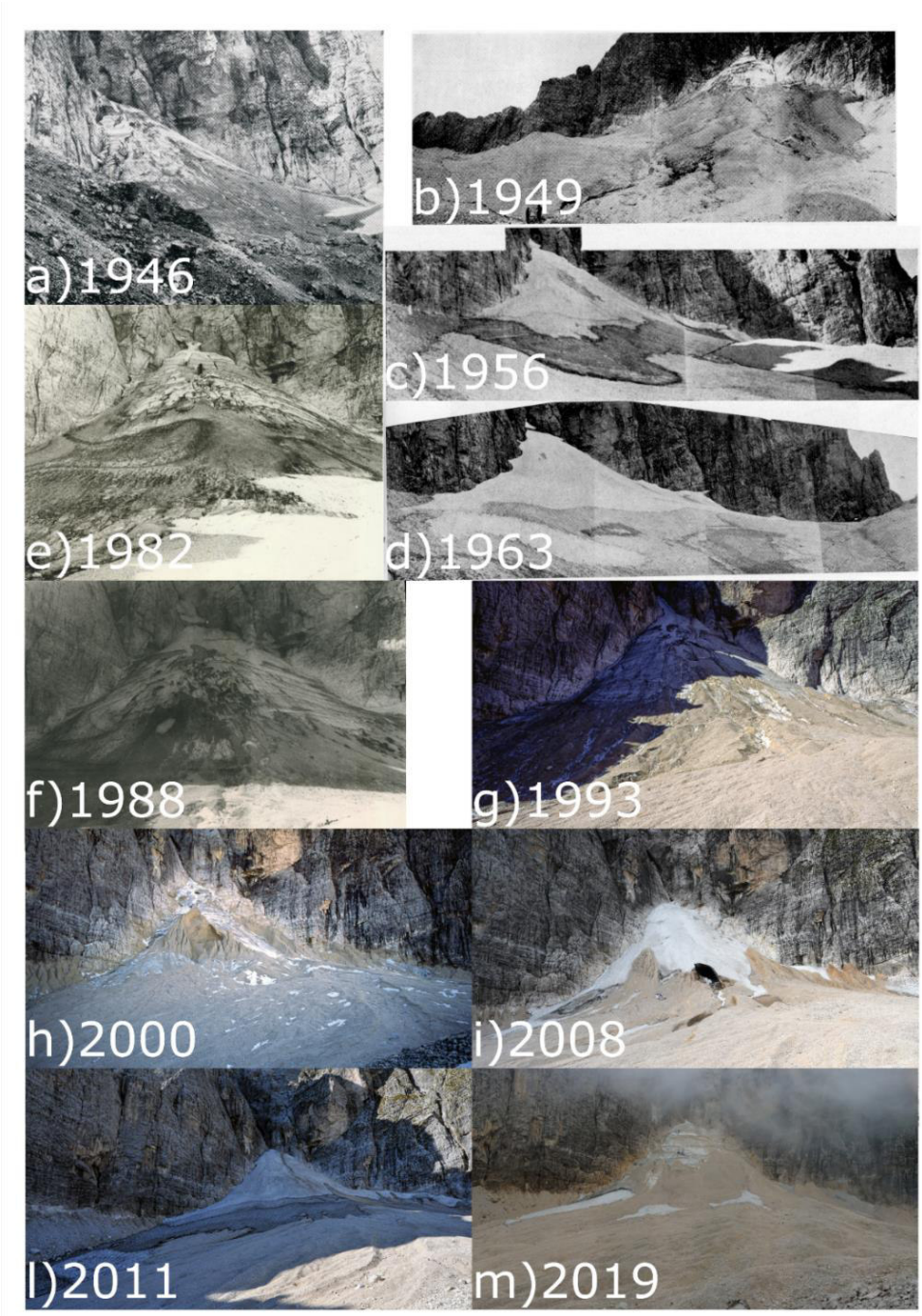

Figure 4.2 *Photo of the Montasio Glacier taken at the end of the ablation season (authors in brakets): (**a**) september 1946 (Dino Di Colbertaldo,* [25]*); (**b**) 1949 (Dino di Colbertaldo,* [23]*); (**c**) 1956 (di Colbertaldo,* [23]*); (**d**) 1963 (Dino di Colbertaldo,* [23]*); (**e**) 1982 (Rossana Serandrei Barbero, archivio CGI); (**f**) 1988 (Rossana Serandrei Barbero, archivio CGI); (**g**) 1993 (Roberto Degli Uomini); (**h**) 2000 (Roberto Degli Uomini); (**i**) 2008 (Roberto Degli Uomini); (**l**) 2011 (Roberto Degli Uomini); (**m**) 2019 (Jessica De Marco).*

Roberto Degli Uomini built independently a unique series of observations consisting of annual photographs taken at the end of the ablation season from 1987 to 2021. These photos are unpublished and have been made available for this study.

In the last two decades the glacier has been extensively investigated by Universities of Udine and Padova [7,11,26]. These studies analysed the glacier's behaviour, applying innovative geodetic techniques, and documenting conditions of minor imbalance compared to the majority of other Alpine glaciers. Similar investigations carried out at neighbouring ice bodies confirm this peculiarity, which is related to the specific glaciers' characteristics and to the climatic setting of this geographic area, which benefits from a recent increase in solid precipitations [14].

4.4 Materials and methods

The behaviour of the Montasio Glacier in the last century has been investigated and characterised analysing *i*) changes in surface cover (type and spatial coverage of different substrata), *ii*) elevation changes, *iii*) mass balance across different periods, and iv) corresponding changes in the most relevant meteorological variables. The input data used in this study are summarized in Table 4.1.

Table 4.1 *Data retrieved for this study, related reference/data provider, and applications.*

Data source	**Data**	**Reference/data provider**	**Application**		
			Mass balance calculation	Extent and surface cover analysis	Meteorological analysis
Maps	Map 1920	Desio A. [22]		X	
DEMs	DEM from map 1920 and image 1917	Carturan et al. (2021) [27]	X		
	DEM from aerial images 1948	This study	X		
	DEM from map 1983	FVG Region	X	X	
	DEM from ALS 2006	FVG Region	X		
	DEM from TLS (2010-2013)	Carturan et al., (2013); Piermattei et al., (2015)[7,26]	X	X	
	DEM from images by SfM (2014-2019)	De Marco et al. (2020)[11]	X	X	
	DEM from images by SfM 2019-2020	This study	X	X	
	DEM and Point cloud from ALS 2018	FVG Region	X		
Aerial images	Aerial images 1948	IGM copyright		X	
	Orthophoto 2006	FVG Region		X	
Terrestrial images	Images 1921-1948.	Desio, Di Colbertaldo [23]		X	
	Annual images 1987-2021	Degli Uomini [not published]		X	
	Annual images 2010-2021	Hydrolab research group (UniUD)		X	
Meteorological data	Temperature, precipitation 1926-2020	De Marco et al. (2020)[11] and this study			X

4.4.1 Glacier change analysis

Surface cover analysis

Changes in the areal extent and surface cover of the Montasio Glacier have been reconstructed and analysed since 1920 using available aerial photographs and maps, with the help of oblique terrestrial images taken mostly from the frontal moraine (Table 4.1 and Figure 4.2). The aerial photos have been georeferenced using the Qgis georeferencing tool, based on the coordinates of stable and recognisable Ground Control Points (GCPs) selected on the glacier surroundings from the 2018 ALS DEM (Table 4.1). In addition, we used field survey notes, qualitative observations and descriptions of morphological changes reported in the glaciological campaigns [23,24].

Field surveys also report length change measurements, which however are affected by a high degree of uncertainty. Since the beginning of observations, in the early 1920s, it was increasingly difficult to locate the lower margin of the glacier due to the debris coverage. In addition, there are uncertainties related to the use of different marks by the different observers, which could not be solved unambiguously. For this reason, we avoided analysing length changes, which anyway are of minor importance for this glacier. Recent geophysical investigations, indeed, have shown that the current lower edge of the glacier lies just 40 m upstream of the Little Ice Age maximum moraine [7].

The glacier extent in 1920 was available from the work of Carturan et al., (2021)[27]. The extent in 1948, 1982, 2006 and 2020 have been mapped outlining its the glacier perimeter in the georeferenced aerial photographs, with a planimetric accuracy of about 10 m. The lateral and upper edges of the glacier were easy to identify because the debris cover was absent or thin, and they clearly stand out from the surrounding terrain. The lower edge was more difficult to map, and we drew it using the current edge (derived from geophysics) and the 1920 edge (marked by an evident moraine ridge) as constrains. We assume negligible frontal advance in the analysed period, testified by a lack of moraine ridges between the 1920 and the current front positions, and positioned the frontal margin in correspondence of breaks of local slope visible in photographs and hillshaded DEMs of the corresponding years.

The surface cover was classified into five main types: snow, firn, ice, shallow debris cover, and thick debris cover. These substrata have been mapped by visual recognition in the photographs, and with the help of hillshaded DEMs. Snow was relatively easy to distinguish from firn due its lighter colour, caused by a lower coverage of dust and debris. Moreover, ice without debris cover was

rather easy to distinguish from snow and firn because it clearly shows a finely layered structure. Thick and shallow debris cover were distinguished based on their appearance: dry with a lighter colour the first, darker and wet-looking the second.

Generation of DEMs

Elevation changes and geodetic mass balance have been calculated using all data available for generating DEMs dated between 1920 and 2020. Five DEMs with pixel size of 1 x 1 m (year 1920, 1948, 1982, 2006, and 2020) have been reconstructed, applying different methods based on the type and quality of input data (Table 4.1).

The 1920 DEM derives from the Desio's topographic map [22]. The map has been georeferenced, digitized and converted to a DEM using the ArcGIS software (ESRI, USA). Details on the workflow are reported in Carturan et al. (2021)[27].

The 1948 DEM was obtained from four aerial photographs taken on September 19, 1948 by the IGM (Italian Military Geographic Institute). The photos were scanned using a photogrammetric hardware to avoid distortions during digitization, which could negatively affect the photogrammetric pipeline and increase the error of the derived DEM [28]. Images were processed with the Structure-from-Motion (SfM) algorithm implemented in the Metashape software (v. 1.6.4 build 10928, Agisoft LLC, St. Petersburg, Russia) to create a dense point cloud which was initially georeferenced and scaled using 13 highly recognisable and stable Ground Control Points (GCPs), located outside the glacier. 3D coordinates of the GCPs had been obtained from the 2018 ALS survey. Residual misalignments in the georeferencing were subsequently minimized by applying the Iterative Closest Point (ICP) algorithm implemented in JRC 3D Reconstructor software (v. 4.3.1, Gexcel, Cagliari, Italy) using the 2018 ALS survey as reference cloud. To compute the roto-translation transformation, only the stable areas outside the glacier have been used. The point cloud was then subsampled using the ArcGIS (ESRI) plugin TopCAT (Topographic Point Cloud Analysis Tool), converted to a TIN (Triangular Irregular Network) model and subsequently rasterized to a 1x1 m grid.

The only cartographic information regarding the Montasio Glacier between 1948 and 2006 is a photogrammetric map (scale 1:5000) surveyed on June 6, 1983, which has been georeferenced, digitized and converted to a DEM. Unfortunately, this date is far from the end of the ablation season, and close to the end of the accumulation season. Due to the high snow accumulation in this

geographic area, the surface topography in June is normally several metres higher than the underlying glacier surface, hiding the 'true' glacier geometry. To overcome this issue and try to account for the snow accumulated in the 1982-'83 accumulation season, we estimated the 1982-'83 winter balance by means of a linear regression between available geodetic winter balance measurements (in the period from 2011 to 2021) and the winter precipitation data (from November 1 to April 30) at the Pontebba weather station (Section 4.4.2). The obtained winter balance was converted to snow depth using the end-of-winter mean snow density measured in snow pits. The snow depth was finally subtracted to the June 1983 surface topography, obtaining the 1982 end-of-summer surface topography of the glacier. As we are aware of the limitations of this approach, which does not account for the spatial distribution of snow, we only used this topography for geodetic mass balance calculations (i.e. we did not analyse the spatial variability of elevation changes). We choose to use the 1983 survey, even with these limitations, because the early 1980s represent an important climatic shift (Section 4.5.2).

Two DEMs derived from ALS surveys commissioned by the Civil Protection Department of the Friuli Venezia-Giulia Region were available, one for 2006 and another one for 2018. The surveys have been performed by the same private company (Helica srl). In 2006 the flight was performed in September 13, using the Optech ALTM 3100 EA at an average flight altitude of 800 m above ground level (a.g.l.) with an acquisition mode up to 4 returns and a vertical uncertainty <0.15 m up to 1200 m a.g.l.. The resulted nominal point density was 4 points m^{-2}. The 2018 survey was done in July 23, using a Riegl LMS-Q780 at an average flight altitude of 500 m a.g.l.. Data were acquired with a full waveform acquisition mode, achieving a vertical accuracy of 0.02 m at 250 m a.g.l. and obtaining a nominal point density of 18 points m^{-2}. The 2006 point cloud has been employed for mass balance calculations whereas the 2018 point cloud has been used as a reference for georeferencing all the other surveys and for calculating residual errors.

The 2020 DEM was calculated from an *ad hoc* SfM survey carried out on October 8, 2020 with a DJI Matrice 210v2 quadcopter equipped with a DJI X5S camera (20.8 MP, 4:3, 17.3x13 mm sensor, 15 mm focal length). A total of 513 nadir and 209 oblique images were collected and then processed using Metashape software. GCPs positions were measured via GNSS on the same day and they were used as georeferencing constraints in the photogrammetric pipeline described in Cucchiaro et al. (2018)[29]. Both 2006 and 2020 point clouds were co-registered to the 2018 ALS [30] and successively subsampled, converted to TIN and rasterized to DEM as described for the 1948 DEM.

DEM errors have been assessed on stable areas outside the glacier, computing the elevation difference from the 2018 reference DEM. Estimated errors for single pixels range from 0.09 to 4.95 m (Table 4.2). The total uncertainty for glacier-wide calculations of elevation and volume change depends on the size of the averaging area and the scale of the spatial correlation of elevation differences among the DEMs [31]. Unfortunately, it was impossible to obtain reliable statistics (i.e. the spatial correlation function), given the insufficient coverage outside the glacier. Therefore, the errors estimated for single pixels represent an upper limit of the errors in glacier-wide calculations. For the 1920 DEM, uncertainty assessments were only possible along the 1920 glacier perimeter, because the Desio's map reports topographic information only inside the glacier. An error of 4.94 m could be estimated for this DEM, however this has to be considered as a rough estimation (the only feasible) because paraglacial reworking may have affected the deposits along the 1920 glacier margin.

Elevation change analysis

Elevation changes have been calculated for each 1 x 1 m pixel and for different sub-periods, subtracting couples of DEMs (the so-called calculation of the DEM of Differences - DoDs). The area of interest for each comparison has been set equal to the merged area between the initial and final extent of the glacier in the analysed period. The DoDs enabled analysing the spatial variability of elevation changes and of their annual rates. For the 1948-1982 and 1982-2006 sub-periods, however, we only calculated the total elevation difference (used in mass balance calculations) and not attempted to map or analyse its spatial distribution, due to the limitations of the 1982 DEM described in the section above.

Mass Balance calculation

Geodetic mass balance for different sub-periods have been derived from the calculated DoDs (Section 4.4.1). Total volume changes calculated over the merged initial/final area of the glacier have been converted to water equivalent using a mean density of 850 kg m^{-3} [32,33]. To obtain the average annual mass balance rate, the obtained value was divided by the mean glacier area (half-sum of the initial and final area) and by the time interval (in years). The residual errors in DEMs construction, detailed in Section 4.4.1, translate to an error in geodetic annual mass balance rates

ranging from 0.01m w.e.y^{-1} for the 2006-2020 mass balance period, to 0.16 m w.e.y^{-1} for the 1982-2006 mass balance period (Table 4.3).

Table 4.2 *Statistics of elevation differences calculated among individual DEMs and the reference 2018 Lidar DEM over stable areas in proximity of the glacier.*

DEM	Mean (m)	St Dev (m)
1920	0.65	4.94
1948	-0.07	0.69
1983	1.34	4.93
2006	-0.019	0.09
2020	0.149	0.11

4.4.2 Analysis of Meteorological data

A meteorological data series of daily air temperature and precipitation from 1927 to 2020 is analysed in this work. This analysis enabled us to detect possible long-term trends in meteorological condition and to relate them to the evolution of the Montasio Glacier in the last century. The series analysed in this paper is an extension of the data of the Pontebba weather station (568 m a.s.l.), presented in De Marco et al. (2020)[11], which spans the period from 1961 to 2020. This weather station was selected due to its relative proximity to the glacier, the high quality of air temperature and precipitation series, and the length of meteorological records. Data prior to 1961 have been taken from Baldassi (2010) [34], who performed quality check, homogenization, and gap-filling in meteorological data in the period from 1927 to 1961. The temperature series was extrapolated at the Montasio Glacier mean elevation (1910 m a.s.l.) using monthly vertical gradients calculated over the period from 1999 to 2010 between the Pontebba and Lussari (1760 m a.s.l.) weather stations. The resulting temperature was used for discriminating between liquid and solid precipitation at the glacier's elevation, using a daily threshold temperature of 2 °C [11]. In this way, it was possible to estimate the nivometric coefficient (fraction of solid precipitation) at the glacier's mean elevation and its variability in the last century. We avoided extrapolating precipitation data at the glacier's elevation because the study area is affected by large horizontal and vertical gradients in precipitation, which are difficult to calculate due to the lack of reliable precipitation data at high elevation [35]. For this reason, we preferred quality-checked precipitation data at low altitude to extrapolations subject to high uncertainty.

Air temperature, precipitation, and nivometric coefficients have been analysed separately for the ablation and the accumulation seasons (May to October and November to April, respectively). Trends and break points were assessed using non-parametric tests for annual and seasonal data of temperature and precipitation (solid, liquid, and total). The Mann-Kendall test was used to establish whether a trend exists in the time series; afterwards, break points presence and their positions were assessed using the Pettitt's test [36]. Finally, the occurrence of multiple break points was verified based on the BIC test (Bayesian Information Criterion) implemented in the "strucchange" R package [37]. Descriptive statistics have been calculated for each meteorological series and for sub-periods detected by the break point analysis.

4.5 Results

4.5.1 Glacier changes analysis

Elevation changes and mass balance

The Montasio Glacier underwent a thinning of 27.75 m ± 5.32 m, on average, between 1920 and 2020 (Table 4.3). Forty-nine percent of the total thinning occurred before 1948, another 18% by 1982, an additional 31% by 2006, and only 2% after 2006. The available DEMs show continuous thinning, even though short periods of temporary thickening cannot be excluded, due to the time distance among DEMs. Thinning rates were largest between 1920 and 1948, with an average value of 0.52 m y^{-1} and a mass balance rate of -0.49 ± 0.13 m w.e. y^{-1}. In the period between 1948 and 1982 the surface lowered more slowly in comparison with the previous time interval, with a mean rate of 0.16 m y^{-1} and a mass balance of -0.14 ± 0.11 m w.e. y^{-1}. Rates of lowering and mass loss increased substantially afterwards, reaching 0.39 m y^{-1} and -0.36 ± 0.16 m w.e. y^{-1}, respectively, in the period from 1982 to 2006. The last period showed the lowest thinning rates, with a mean value of 0.04 m y^{-1} in the period from 2006 to 2020 and a mass balance of -0.03 ± 0.01 m w.e. y^{-1}, which was closer to equilibrium.

The spatial patterns of elevation changes show that the largest cumulated thinning between 1920 and 2020 occurred in the upper part and in the orographic right portions of the glacier, locally exceeding 40 m (Figure 4.3). In comparison, the lower part of the glacier underwent smaller thinning, comprised between 10 and 30 m. The different behaviour of the upper and lower glacier portions is more evident after 1948, whereas before 1948 the thinning rates of the two parts showed

higher similarity. After 2006 thickening prevailed in the upper part, while the lower part continued thinning with a rate that is comparable to the period between 1948 and 2006 (Figure 4).

Table 4.3 *Total elevation change and mass balance rates averaged on the Montasio Glacier in different periods.*

Period	Years	Total elevation change ±σ (m)	Annual Balance (m w.e. year^{-1})	Error (m w.e. year^{-1})
1920-1948	28	-14.55±4.37	-0.49	0.13
1948-2006	58	-14.54±0.97	-0.24	0.01
1948-1982	34	-5.51±4.57	-0.14	0.11
1982-2006	24	-9.35±4.62	-0.36	0.16
2006-2020	14	-0.56±0.24	-0.03	0.01
1920-2020	100	-27.75±5.32	-0.28	0.05
1948-2020	72	-14.93±0.95	-0.19	0.01

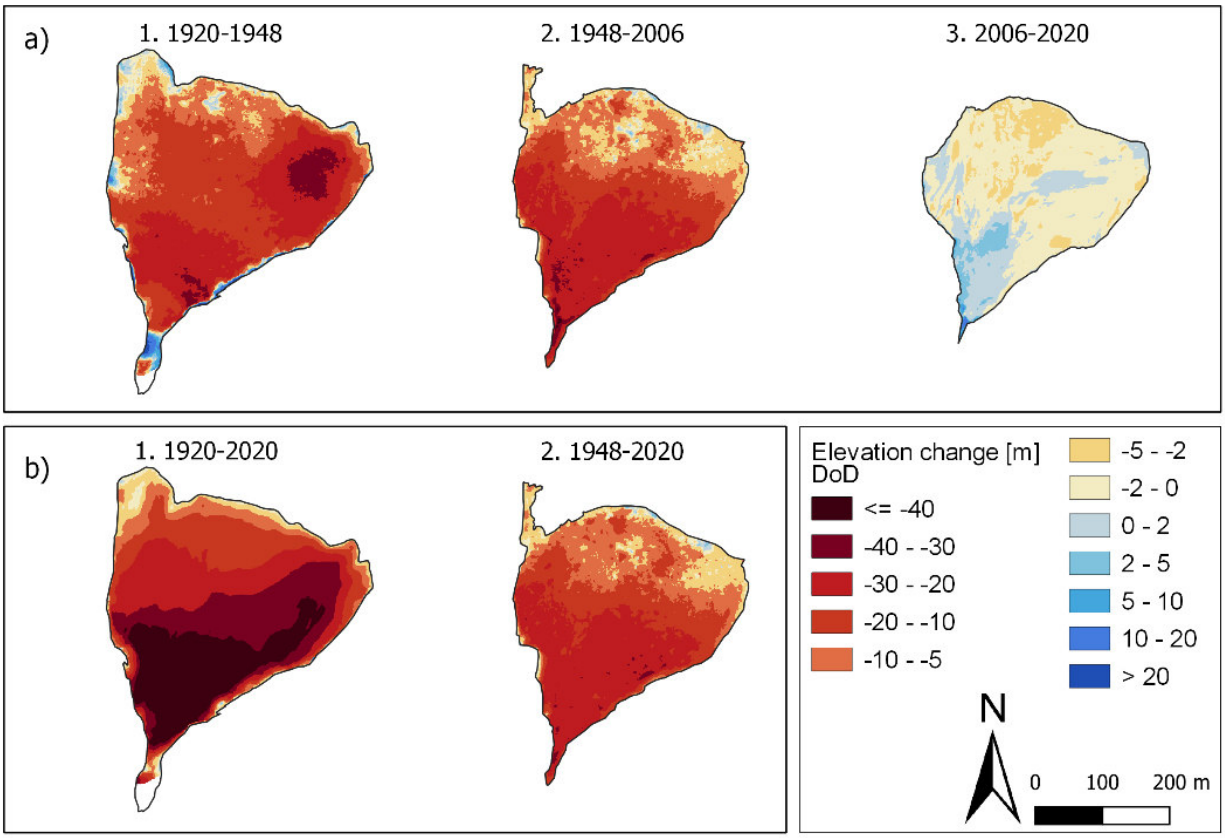

Figure 4.3 *Total elevation changes on the Montasio Glacier a) for three sub-periods, and b) cumulated from 1920 and 1948*

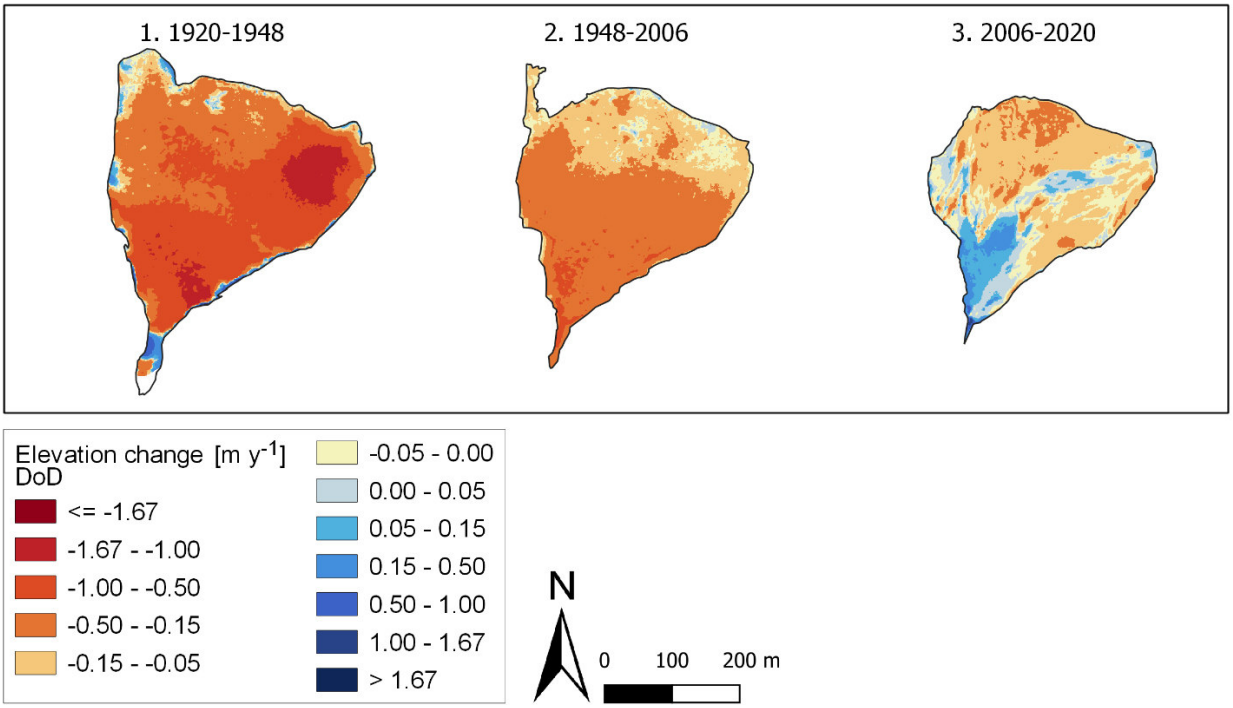

Figure 4.4 *Annual rates of elevation change on the Montasio Glacier averaged during three sub-periods.*

Changes in surface cover types

The surface cover analysis shown in Figure 4.5 highlights a significant increase in debris cover on the Montasio Glacier during the last century. In 1920, as reported by A. Desio [22], the surface was almost free from debris, except for the lower margin and for the top of the glacier where there was a shallow debris cover. By 1948, the glacier thinned considerably and became mostly covered by debris, as can be appreciated from various terrestrial photos taken by observers in the 1940s. These photos show the top of the glacier almost free from debris, the middle part with discontinuous and shallow debris cover over stratified glacier ice (Figure 4.2a-b), and the lower part covered by thick debris and with a complex surface morphology due to differential ablation, similar to 'hummocky moraine' terrain. Unfortunately, the 1948 aerial photo only shows the lowermost part of the glacier due to a widespread snow cover.

Terrestrial photos taken in the 1950s and 1960s, and field reports from the 1970s, document the existence of several layers of snow and firn from different years covering most of the glacier. The new firn layers covered a large fraction of the debris-covered area, whose spatial extent decreased significantly and was limited to the lower portion. The surface cover analysis for 1986 (Figure 4.5) depicts the glacier at the end of this period, which was rather favorable for glacier preservation. As

can be seen, in 1986 the glacier surface was still covered by snow, firn and stratified glacier ice in the middle and upper areas, whereas the debris cover was confined to the lower part. Crevasses were clearly visible in the upper area until the 1980s.

By 2000, the glacier was completely buried under a thick debris mantle, except for the top of the avalanche cone where very small patches of snow, firn and glacier ice were still visible. During the 1990s and the early 2000s the glacier has been repeatedly affected by flooding events, some of which of large magnitude [38], which left clear traces of glacial-fluvial reworking (debris flows) on the glacier surface and surrounding deposits (Figure 4.2h and 4.2i).

In the last years, the most significant changes occurred in the upper part, with the alternation of periods with snow and firn cover expansion (2009-2011, 2013-2014) and periods of rapid snow and firn depletion (2012, 2015-2019), when there was a tendency to a new, rapid increase in the debris cover. After the 1980s, only few transverse crevasses were visible and were limited to the top of the glacier. Nevertheless, recent investigations have shown that the glacier still preserve surface dynamics and mean displacement rates of ~0.2 m y^{-1} in the lower part [11]. Geophysical investigations carried out in 2010 showed that the thickness of the debris cover in the lower half of the glacier is of 2-3 m [7]. The hummocky moraine morphology observed in the 1940s in this area has been completely replaced by glacial-fluvial reworking (debris flows), although some dead-ice landforms (kettle-holes) are still present.

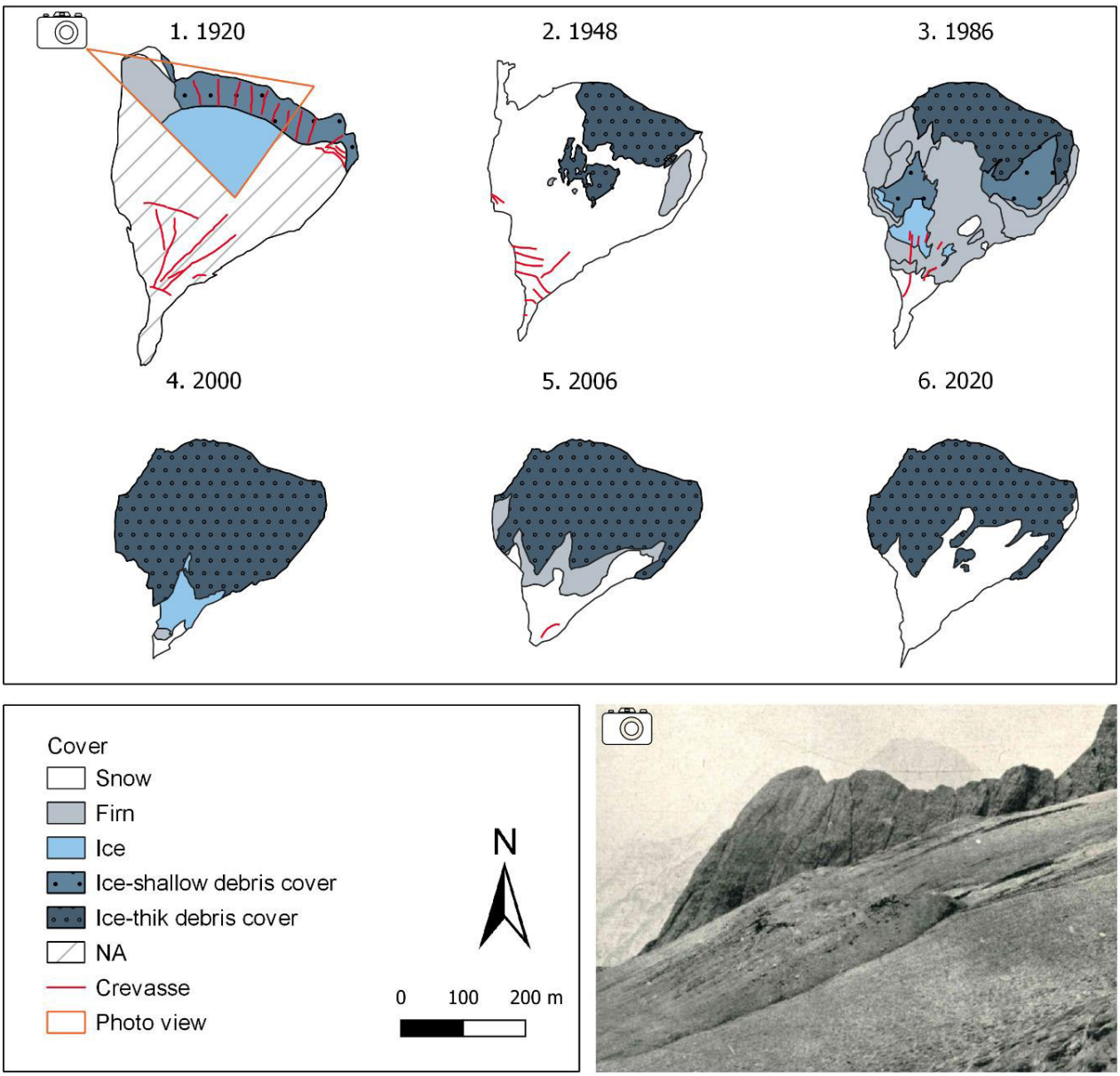

Figure 4.5 *Surface cover types on the Montasio Glacier: snow, firn, ice with shallow debris cover, debris cover (ice with thick debris cover). Cover types are derived from aerial photos available in September-October of each year. The 1920 map shows surface types visible in the only photo available for that year (Desio, 1923, photo reported in the figure) and the crevasses reported in the Desio's topographic map.*

4.5.2 Change in climatic conditions

The breakpoint analysis applied to the meteorological data series available from 1927 to 2020 revealed significant breakpoints for air temperature, Nivometric Coefficient (NC) and solid precipitations. No breakpoints were detected in the time series of total precipitation for the

accumulation and ablation seasons, total annual precipitation, and solid precipitation in the accumulation season; linear trends were also inexistent or without statistical significance for these variables.

Temperature breakpoints occurred for both accumulation and ablation seasons in the 1980s (Figure 4.6a). In the accumulation season, one break point was identified in 1987 that separates a first subperiod without trend, followed by another subperiod with a positive and significant trend (0.052 °C y^{-1}, $p<0.05$). A break point in the ablation season temperature series was detected 6 years earlier, in 1981, preceded by a slightly negative trend (-0.012 °C y^{-1}, $p<0.05$) and followed by a positive trend (0.040 °C y^{-1}, $p<0.001$). The air temperature in the accumulation season averaged -4.62 ± 0.89 °C before 1987 and -2.66 ± 0.92°C afterwards. In the ablation season, it increased from a mean value of 5.72 ± 0.75 °C before 1981 to 7.62 ± 0.69 °C afterwards.

Before 1970, the NC in the accumulation season did not show a significant trend, while, after 1970, the NC started to decrease with a rate of -0.35 % y^{-1} ($p<0.001$). After 1995, the NC in the accumulation season consistently deviated from 100%, highlighting an increasing fraction of liquid precipitation. Regarding the ablation season, no significant trends were found before and after the break point in 1984, but the two subperiods were characterised by different mean values (32 ± 12% and 17 ± 9%, respectively), which highlight a substantial halving of solid precipitation during summer. Indeed, the analysis of solid precipitation in the ablation season detected a decrease in mean values from 328 ± 128 mm before a break point in 1987, to 171 ± 98 mm after it.

The Figure 4.7 plots time series of air temperature and total precipitation anomalies compared to the 1927-2020 means. In the first period of highly negative mass balance, between 1920 and 1948, the most relevant anomaly was for total precipitation in the accumulation season, which shows a long period (from 1937 to 1947) with low snow accumulation. This is the driest decade in the entire series. Temperature anomalies were of lower significance, although the dry period was associated to increasing air temperature.

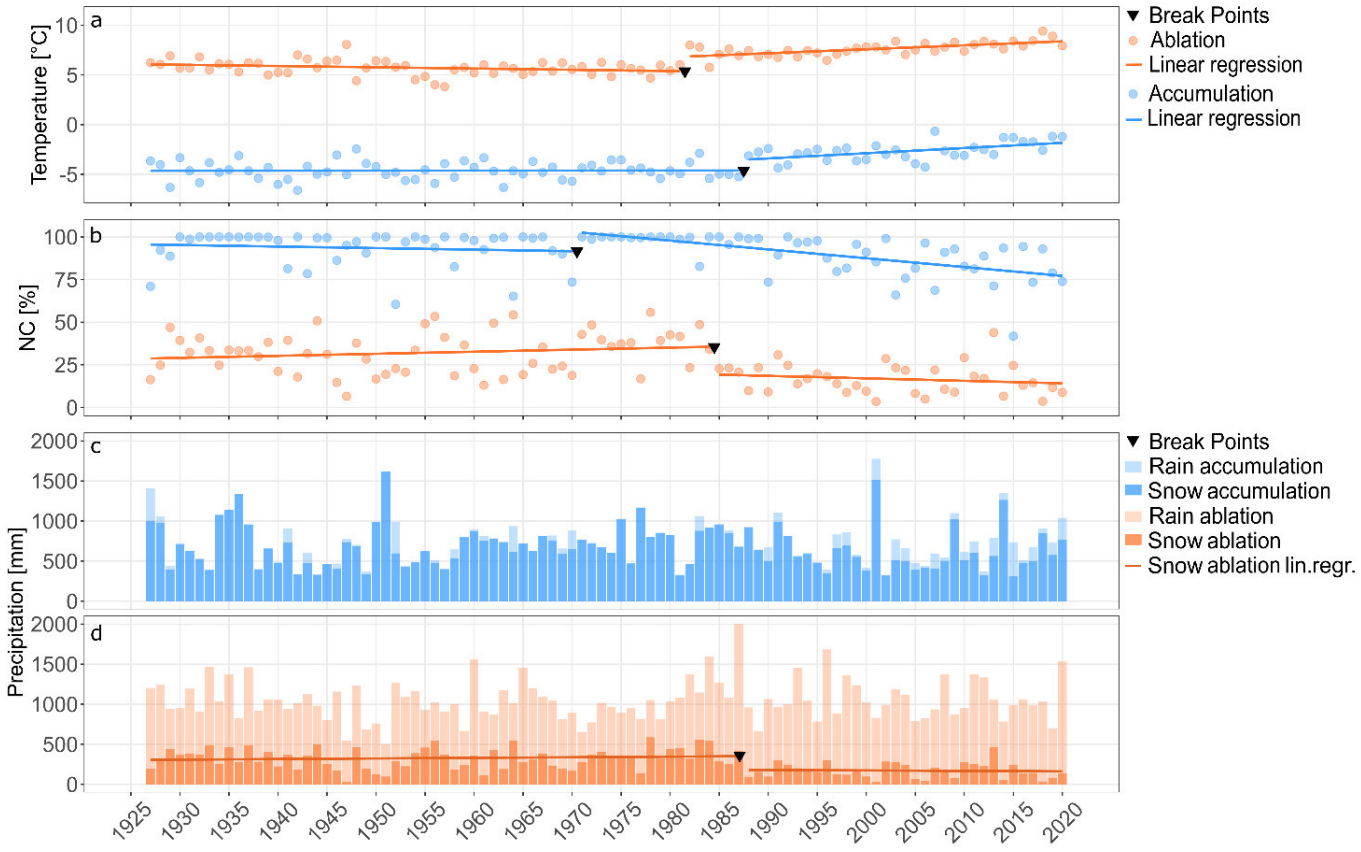

Figure 4.6 *Meteorological time series for the area of Montasio Glacier: (**a**) air temperature, (**b**) Nivometric Coefficient (NC), (**c**) precipitation in the accumulation season (light blue = rain, dark blue = snow), (**d**) precipitation in the ablation season (light orange = rain, dark orange = snow). Blue tones represent the accumulation season (November to April), while orange tones represent the ablation season (May to October). Significant trends for the Mann Kendall Test are represented by solid lines. Break points are represented with black triangles.*

In the period of slightly negative mass balance, between 1948 and 1982, there was an evident decrease in air temperature, especially in the ablation season. Total precipitation in the accumulation season came back to average or slightly above-average values, with smaller inter-annual variability and a small tendency to increase between the late 1950s and the 1980s, after a dry period in the first half of the 1950s.

Starting in the 1980s, there was a visible warming, which is still going on. The precipitation in the accumulation season was mostly below average from the late 1980s to the early 2000s, with increasing inter-annual variability. Accumulation came back to the long-term average after 2008, with snow-rich winters in 2009, 2014, and 2020.

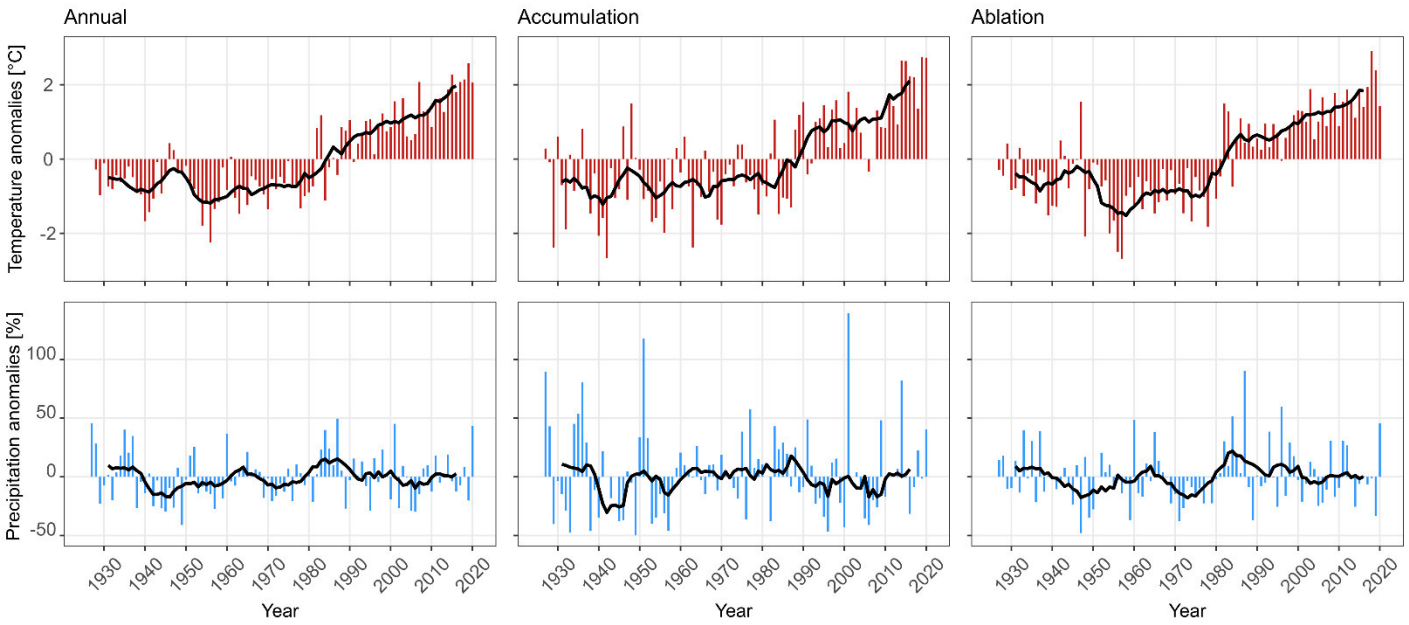

Figure 4.7 *Seasonal and annual temperature and total precipitation anomalies for the period from 1927 to 2020. Black lines are 9-year centred moving averages.*

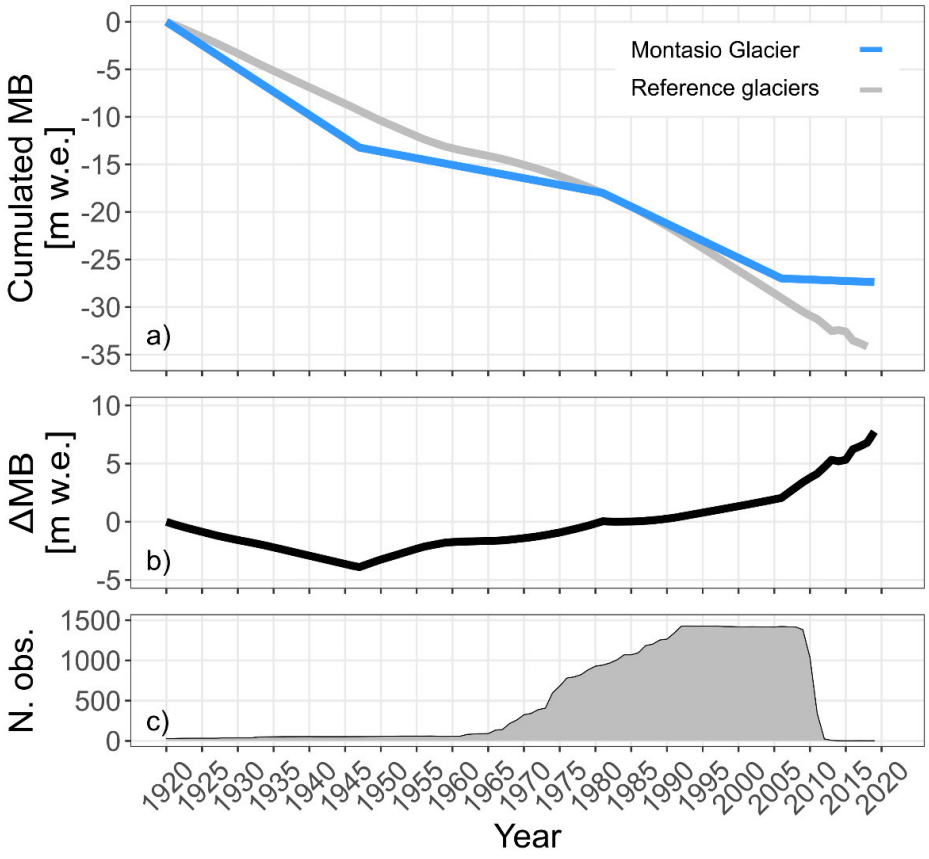

Figure 4.8 *(**a**) difference between the two cumulated data, (**b**) Cumulated mass balance of Montasio Glacier compared to the average geodetic cumulated balance WGMS data set for Central*

Europe [39]*; (**c**) number of geodetic mass balance observations used to estimate the average geodetic cumulated balance*

4.6 Discussion

The peculiar behaviour and climatic response of the Montasio Glacier has been analysed in detail by recent investigations [7,11], whose main results highlight:

i) a low response to regional air temperature variability;
ii) a high response to regional snow accumulation variability;
iii) a 'normal' relationship between mass balance and elevation in years with positive mass balance (i.e., net accumulation in the upper part and net ablation in the lower part);
iv) 'inverted' mass balance gradient in years with negative mass balance (i.e. lower mass balance in the upper part, free from debris);
v) high mass balance sensitivity after years with positive mass balance (expansion of the firn area, which is free from debris);
vi) low mass balance sensitivity after years with negative mass balance (expansion of the debris-covered area).

These dynamics have been investigated with a quantitative approach, and high spatial and time resolution, for the most recent years, whereas longer-term effects were only hypothesized. In this work we report major variations in the surface conditions and climatic response of the glacier across a much longer period. The integrated analysis of mass balance, surface cover and meteorological data enabled a good description of glacier variations and dynamics in the last century (1920-2020).

This analysis shows an overall trend towards decreasing imbalance and decreasing mass balance sensitivity for the Montasio Glacier. Although snowy winters can explain some positive mass balances in recent years, the current behaviour of this glacier is mostly associated with debris cover dynamics over multi-decadal time scales. Debris supply is ensured by the continuous action of cryo-clastism, avalanches and rock falls, and is abundant in comparison to glacier transportation efficiency, due to the high ratio between the area of debris-providing rock walls and the glacier area [40,41]. Debris evacuation by glacier transport outside the LIA and 1920s moraines has become negligible since the first decades of the 20th Century, and these moraines have a damming effect on debris transported by glacifluvial processes. The resulting increase in area and thickness of the debris mantle is an important negative feedback that is contributing to the preservation of the Montasio Glacier.

In the last century, the mass balance of the glacier has been characterized by four major phases: rapid mass loss until the 1940s, conditions close to balanced-budget until the 1980s, rapid mass loss (but slower than in the 1930s and 1940s) in the 1990s and early 2000s, and balanced-budget conditions afterwards. This behaviour is similar to most alpine glaciers until the 1980s; however, it tends to diverge from the majority of alpine glaciers starting in the 1990s (Figure 4.8.a-b), showing decreased imbalance and mass balance sensitivity. The Figure 4.8 compares the cumulated geodetic mass balance of the Montasio Glacier with the mean of all glaciers in the European Alps that have geodetic balance measurements in the same period [39] . The two series and their cumulated difference (Figure 4.8a and 4.8b) clearly highlight a higher balance sensitivity of the Montasio Glacier between the 1920s and the 1940s, and a transition to a lower climatic sensitivity afterwards. The cumulated difference line reverses its slope after 1948, and becomes much steeper after 2006, suggesting a further decrease in the climatic sensitivity of the Montasio Glacier compared to other monitored glaciers in the Alps.

The mass loss of Montasio Glacier is not associated with 'active retreat', as for other glaciers showing low climate change vulnerability. Indeed, the Montasio Glacier experienced small areal changes in the last decades, and its front lies in close proximity to the LIA moraines [7]. This behaviour might suggest a sort of 'stationary thinning', which however is not associated with the positive feedbacks (elevation feedback, decreased cooling effect, increasing thermal emission from the surrounding deglaciated terrain) that speed up deglaciation in other cases [10,42,43]. The stationary thinning of the Montasio Glacier is instead associated to negative feedbacks brought by *i*) increasing debris cover extent and thickness, *ii*) avalanche snow concentration over a smaller area, and *iii*) increasing shadowing by the surrounding terrain. The first process is dominant in the lower half of the glacier, whereas in the upper part there is a prevalence of effects from avalanche concentration and increased shadowing.

The high mass loss in the period from 1920 to 1948 represents 49% of the total mass loss in a century, and can be explained by very low snow accumulation in the decade after 1936, based on meteorological data series. Moreover, the debris coverage was still limited to the lower ablation area, and was relatively thin (up to 50 cm at the lower margin of the glacier). The spatial pattern of surface lowering (Figure 4.3) is clearly related to the spatial extent and thickness of debris cover, as visible in the photos of that period. Indeed, the highest losses occurred in the upper part and in the eastern ablation area, where the debris cover was absent or thin and discontinuous. The middle and western ablation areas were already covered by thick debris, as can be assessed by differential

ablation phenomena reported by observers and visible in the photos, which protected the underlying ice from ablation. The eastern ablation area was, and remains, the most active of the glacier, due to a depression in the bedrock [7].

Favourable meteorological conditions in the following decades, especially between the 1960s and early 1980s, led to a preservation of the glacier, associated to an expansion of the debris-free area and a contraction of the debris-covered area. This however set up conditions of higher vulnerability when meteorological conditions become unfavourable, starting in the late 1980s, because the debris-free area is prone to rapid mass loss in periods with low snow accumulation and/or high summer temperature [11].

After a period of rapid mass loss, however, the areal extent and thickness of the debris cover become so large that it gradually offset a potential increase of ablation due to rising temperatures. Currently, the glacier behaves as a nearly stagnant ice mass covered by a thick mantle of debris, which reactivates following snowy winters. Probably, the active part of the glacier has to be considered its upper and steeper half, which completely rebuilds after snow-rich winters and undergoes rapid thinning and burial by debris in periods with scarce snowfalls (Figure 4.2). This part, for example, underwent negligible change in thickness between the 1940s and the 1980s (Figures 4.2a, 4.2e, 4.2f), rapidly collapsed in the 1990s (Figures 4.2f and 4.2h), and quickly rebuilt with the increase in winter accumulation after 2008 (Figures 4.2h and 4.2l).

A comparison is possible with other ice bodies in the Julian Alps (especially with the Canin East Glacieret), which are located within 10 km from the Montasio Glacier. Several works highlight similar behaviours with positive mass balance in recent years and even mass rebuilt, influenced mainly by winter precipitations[14,44]. The climatic causes are the same (recent snowy winters), however Montasio and Canin glaciers are very different. The latest is indeed without debris cover, and therefore it is expected to have higher climatic sensitivity, and to disappear completely without abundant snowfalls.

The Figure 4.8a compares the cumulated geodetic mass balance of the Montasio Glacier with the mean of all glaciers in the European Alps that have geodetic balance measurements in the same period [39]. The two series and their cumulated difference (Figure 4.8a-b) clearly highlight a higher balance sensitivity of the Montasio Glacier between the 1920s and the 1940s, and a transition to a lower climatic sensitivity afterwards. The cumulated difference line, nearly straight until 2006, sharply changes its slope afterwards, suggesting a further decrease in the climatic sensitivity of the

Montasio Glacier compared to other monitored glaciers in the Alps. After ~80 years with similar behaviour, now there is a clear tendency towards a clear decoupling between the Montasio Glacier and the rest of the glaciers in the Alps.

On the basis of collected evidences and current trends in meteorological variables, it is possible to outline a plausible evolution for the Montasio Glacier (and other similar ice bodies) in the next few decades. The increasing temperature is leading to a decrease in the solid fraction of precipitation, not only in the ablation season but also in the accumulation season. The latest tends to become shorter, whereas the former tends to expand. Warmer temperature causes also permafrost degradation, and this could be linked with an increase in rock fall activity from the rock walls above the glacier, where the permafrost map published by Boeckli et al. (2012) [45] indicates the possible presence of permafrost above ~2400 m a.s.l. Thanks to a likely increase in the coverage and thickness of the debris cover, the Montasio Glacier is not expected to disappear soon, even with a decrease in snow accumulation. However, it is expected to become progressively less active if the warming continues.

A transition to a rock glacier, or a glacial-permafrost composite landforms [46,47] cannot be completely ruled out. Nevertheless, in our opinion this occurrence is unlikely in the next future because in the glacier area the conditions are unfavourable for permafrost. The Boeckli et al. (2012) [45] map plots 'permafrost only in very favourable conditions' there. Considering the low elevation of the glacier, almost entirely below 2000 m, only open-work deposits could enable the presence or formation of sporadic permafrost and a possible shift from glacial towards periglacial conditioning. The current grain size distribution (with considerable infill of fine debris between blocks) and the surface morphology of the debris-covered area and proglacial deposits (complete lack of morphological features typical of active rock glaciers) lead us to exclude the presence of permafrost in the glacier area and the impending transition to permafrost-related landforms. Geophysical investigations carried out in late summer of 2010 highlighted massive glacier ice under the debris cover, but no frozen sediments [7]. Additional investigations are probably required to check or exclude the possible occurrence of permafrost conditions in the glacier area, for example by means of thermal methods associated to other geophysical prospections.

The sediment budget is currently positive thanks to the damming effect of moraine deposits in front of the glacier. Further thinning from ice melt is expected to increase the maximum volume of debris that can accumulate upstream of these deposits. Only fluvial or glacio-fluvial processes can erode

substantial amounts of debris. Recent investigations have shown that high-magnitude flooding events can rework and even erode large amounts of debris from the glacier area, through the lateral breaches of the LIA moraine [38]. In case of increased frequency of these extreme events, sediment dynamics will possibly change in the future and lead to a more efficient removal of debris from the glacier area, with adverse consequences on the preservation of the residual ice body.

4.7 Conclusions

This work presents a reconstruction of the behaviour of the Montasio Glacier during the last 100 years. The reconstruction is based on a comprehensive collection of data, which have been processed to derive series of elevation change, geodetic balance rate and surface cover change from 1920 to 2020. The results show a consistency with the behaviour of most alpine glaciers until the 1990s, and a clear decoupling in the 2000s. In fact, most of the mass losses occurred between 1920 and 1948 (49% of the total mass loss), followed by nearly balance-budget condition until the 1980s (18% of the total mass loss). The high melt rate observed in the first decades was associated to negative anomalies in snow accumulation, in particular between the late 1930s and the early 1940s, while relatively favourable conditions characterised the period between 1960s and 1980s.

A new phase of rapid mass loss occurred between the 1980s and the -1990s, when temperature started increasing sharply. However, in the last two decades, the glacier entered a new phase close to balanced-budget conditions, in spite of sustained atmospheric warming. This behaviour is clearly decoupled from the regional temperature fluctuations and from the behaviour of Alpine glaciers with similar monitoring series.

Even if the glacier experienced recent winters with abundant snow accumulation, the main causes of this progressive decrease in climatic sensitivity have to be looked for in negative feedbacks, which offset potential increased melt due to warmer temperature. In particular, starting in the 1940s, the glacier became increasingly covered by a thick layer of debris in the ablation area, which strongly limits ablation. The role of the thick debris cover was already acknowledged by previous investigations on this glacier, but this work documents for the first time the debris cover dynamics in the long term. In addition, the glacier has a lower sensitivity to air temperature fluctuations, compared to precipitation variability, because it is mainly fed by avalanches.

For these reasons, it is important to avoid generalizations and inferences on regional glacier balance and climatic trend based on the behaviour of this small glacier, or of glaciers with similar characteristics, which are common in the carbonatic massifs of the Eastern Italian Alps.

In case of further atmospheric warming, the accumulation seasons are expected to become shorter and less snowy on the Montasio Glacier, with concomitant longer and warmer ablation seasons. This could also lead to permafrost degradation in the surrounding rock walls, potentially increasing rock fall activity and debris supply. For these reasons, a further increase in the spatial coverage and thickness of debris is likely, and therefore the glacier will not disappear in the near future. Unlike other similar ice bodies in the Alps, however, the Montasio Glacier is not expected to evolve into a rock glacier, or a glacial-permafrost composite landform, due to the low elevation and lack of conditions favourable to permafrost.

REFERENCES

1. IPCC *Climate Change 2013: The Physical Science Basis. Contribution of Working Group I to the Fifth Assessment Report of the Intergovernmental Panel on Climate Change*; Stocker, T.F., Qin, D., Plattner, G.-K., Tignor, M., Allen, S.K., Boschung, J., Nauels, A., Xia, Y., Bex, V., Midgley, P.M., Eds.; Cambridge University Press, Cambridge, United Kingdom and New York, NY, USA., 2013; ISBN 978-92-9169-138-8.

2. Marzeion, B.; Jarosch, A.H.; Gregory, J.M. Feedbacks and mechanisms affecting the global sensitivity of glaciers to climate change. *Cryosph.* **2014**, *8*, 59–71, doi:10.5194/tc-8-59-2014.

3. Vuille, M.; Carey, M.; Huggel, C.; Buytaert, W.; Rabatel, A.; Jacobsen, D.; Soruco, A.; Villacis, M.; Yarleque, C.; Elison Timm, O.; et al. Rapid decline of snow and ice in the tropical Andes – Impacts, uncertainties and challenges ahead. *Earth-Science Rev.* **2018**, *176*, 195–213, doi:10.1016/j.earscirev.2017.09.019.

4. Oerlemans, J. Quantifying Global Warming from the Retreat of Glaciers. *Science (80-.).* **1994**, *264*, 243–245, doi:10.1126/science.264.5156.243.

5. Zemp, M.; Huss, M.; Thibert, E.; Eckert, N.; McNabb, R.; Huber, J.; Barandun, M.; Machguth, H.; Nussbaumer, S.U.; Gärtner-Roer, I.; et al. Global glacier mass changes and their contributions to sea-level rise from 1961 to 2016. *Nature* **2019**, *568*, 382–386, doi:10.1038/s41586-019-1071-0.

6. Zemp, M.; Huss, M.; Eckert, N.; Thibert, E.; Paul, F.; Nussbaumer, S.U.; Gärtner-Roer, I. Brief communication: Ad hoc estimation of glacier contributions to sea-level rise from the latest glaciological observations. *Cryosph.* **2020**, *14*, 1043–1050, doi:10.5194/tc-14-1043-2020.

7. Carturan, L.; Baldassi, G.A.; Bondesan, A.; Calligaro, S.; Carton, A.; Cazorzi, F.; Dalla fontana, G.; Francese, R.; Guarnieri, A.; Milan, N.; et al. Current behaviour and dynamics of the lowermost italian glacier (montasio occidentale, julian alps). *Geogr. Ann. Ser. A, Phys. Geogr.* **2013**, *95*, 79–96, doi:10.1111/geoa.12002.

8. Kuhn, M. The mass balance of very small glaciers. *Zeitschrift für Gletscherkd. und Glazialgeol.* **1995**, *31(1)*, 171–179.

9. DeBeer, C.M.; Sharp, M.J. Topographic influences on recent changes of very small glaciers

in the Monashee Mountains, British Columbia, Canada. *J. Glaciol.* **2009**, *55*, 691–700, doi:10.3189/002214309789470851.

10. Carturan, L.; Rastner, P.; Paul, F. On the disequilibrium response and climate change vulnerability of the mass-balance glaciers in the Alps. *J. Glaciol.* **2020**, C, doi:10.1017/jog.2020.71.

11. De Marco, J.; Carturan, L.; Piermattei, L.; Cucchiaro, S.; Moro, D.; Dalla Fontana, G.; Cazorzi, F. Minor Imbalance of the Lowermost Italian Glacier from 2006 to 2019. *Water* **2020**, *12*, 2503, doi:10.3390/w12092503.

12. Gharehchahi, S.; Ballinger, T.J.; Jensen, J.L.R.; Bhardwaj, A.; Sam, L.; Weaver, R.C.; Butler, D.R. Local- and Regional-Scale Forcing of Glacier Mass Balance Changes in the Swiss Alps. *Remote Sens.* **2021**, *13*, 1949, doi:10.3390/rs13101949.

13. Pellicciotti, F.; Stephan, C.; Miles, E.; Herreid, S.; Immerzeel, W.W.; Bolch, T. Mass-balance changes of the debris-covered glaciers in the Langtang Himal, Nepal, from 1974 to 1999. *J. Glaciol.* **2015**, *61*, 373–386, doi:10.3189/2015JoG13J237.

14. Colucci, R.R.; Žebre, M.; Torma, C.Z.; Glasser, N.F.; Maset, E.; Del Gobbo, C.; Pillon, S. Recent Increases in Winter Snowfall Provide Resilience to Very Small Glaciers in the Julian Alps, Europe. *Atmosphere (Basel).* **2021**, *12*, 263, doi:10.3390/atmos12020263.

15. Nicholson, L.; Benn, D.I. Calculating ice melt beneath a debris layer using meteorological data. *J. Glaciol.* **2006**, *52*, 463–470, doi:10.3189/172756506781828584.

16. Benn, D.; Evans, D.J.A. *Glaciers and Glaciation, 2nd edition*; Education, H., Ed.; 2nd Editio.; Routledge: London, 2010; ISBN 9781444128390.

17. Anderson, L.S.; Armstrong, W.H.; Anderson, R.S.; Scherler, D.; Petersen, E. The Causes of Debris-Covered Glacier Thinning: Evidence for the Importance of Ice Dynamics From Kennicott Glacier, Alaska. *Front. Earth Sci.* **2021**, *9*, doi:10.3389/feart.2021.680995.

18. Tielidze, L.G.; Bolch, T.; Wheate, R.D.; Kutuzov, S.S.; Lavrentiev, I.I.; Zemp, M. Supra-glacial debris cover changes in the Greater Caucasus from 1986 to 2014. *Cryosph.* **2020**, *14*, 585–598, doi:10.5194/tc-14-585-2020.

19. Fleischer, F.; Otto, J.; Junker, R.R.; Hölbling, D. Evolution of debris cover on glaciers of the Eastern Alps, Austria, between 1996 and 2015. *Earth Surf. Process. Landforms* **2021**, *46*,

1673–1691, doi:10.1002/esp.5065.

20. Nüsser, M.; Schmidt, S. Glacier changes on the Nanga Parbat 1856–2020: A multi-source retrospective analysis. *Sci. Total Environ.* **2021**, *785*, 147321, doi:10.1016/j.scitotenv.2021.147321.

21. Triglav Čekada, M.; Zorn, M.; R. Colucci, R. Changes in the area of the Canin (Italy) and Triglav glaciers (Slovenia) since 1893 based on archive images and aerial laser scanning. *Geod. Vestn.* **2014**, *58*, 274–313, doi:10.15292/geodetski-vestnik.2014.02.274-313.

22. Desio, A. Su di una forma particolare di ghiacciai delle Alpi venete. *Atti VIII Congr. Geogr. Ital. Firenze 29/3-6/4-1921* **1923**, *2*.

23. CGI (Comitato Glaciologico Italiano) *Reports of the glaciological surveys. 1914-1977*;

24. CGI (Comitato Glaciologico Italiano) Reports of the glaciological surveys. *Geogr. Fis. e Din. Quat.* 1978–2012, 1–35.

25. Dino di Colbertaldo *I ghiacciaio del Canin e del Contasio nel 1946 ed il loro regresso durante l'ultimo ventennio*; CAI, S. monte L.V., Ed.; Stabilimento Poligrafico Longo & Zoppelli: Treviso;

26. Piermattei, L.; Carturan, L.; Guarnieri, A. Use of terrestrial photogrammetry based on structure-from-motion for mass balance estimation of a small glacier in the Italian alps. *Earth Surf. Process. Landforms* **2015**, *40*, 1791–1802, doi:10.1002/esp.3756.

27. Carturan, L.; Bondesan, A.; Carton, A.; Cazorzi, F.; Cucchiaro, S.; De Marco, J.; Piermattei, L. The glaciated landscape across the first world war front: quantitative reconstructions based on digitized historical images and modern techniques. *Geogr. Fis. e Din. Quat.* **2021**, *43*, 143.155, doi:10.4461/GFDQ.2020.43.5.

28. Sevara, C. Capturing the Past for the Future: an Evaluation of the Effect of Geometric Scan Deformities on the Performance of Aerial Archival Media in Image-based Modelling Environments. *Archaeol. Prospect.* **2016**, *23*, 325–334, doi:10.1002/arp.1539.

29. Cucchiaro, S.; Cavalli, M.; Vericat, D.; Crema, S.; Llena, M.; Beinat, A.; Marchi, L.; Cazorzi, F. Monitoring topographic changes through 4D-structure-from-motion photogrammetry: application to a debris-flow channel. *Environ. Earth Sci.* **2018**, *77*, 632, doi:10.1007/s12665-018-7817-4.

30. Cucchiaro, S.; Maset, E.; Cavalli, M.; Crema, S.; Marchi, L.; Beinat, A.; Cazorzi, F. How does co-registration affect geomorphic change estimates in multi-temporal surveys? *GIScience Remote Sens.* **2020**, *57*, 611–632, doi:10.1080/15481603.2020.1763048.

31. Rolstad, C.; Haug, T.; Denby, B. Spatially integrated geodetic glacier mass balance and its uncertainty based on geostatistical analysis: application to the western Svartisen ice cap, Norway. *J. Glaciol.* **2009**, *55*, 666–680, doi:10.3189/002214309789470950.

32. Huss, M. Density assumptions for converting geodetic glacier volume change to mass change. *Cryosph.* **2013**, *7*, 877–887, doi:10.5194/tc-7-877-2013.

33. Sapiano, J.J.; Harrison, W.D.; Echelmeyer, K.A. Elevation, volume and terminus changes of nine glaciers in North America. *J. Glaciol.* **1998**, *44*, 119–135, doi:10.3189/S0022143000002410.

34. Baldassi, G.A. Analisi su base climatologica delle variazioni storiche del ghiacciaio del Montasio (FVG), University of Padua (Ms Thesis), 2010.

35. Schwarb, M. The alpine precipitation climate evaluation of a high-resolution analysis scheme using comprehensive rain-gauge data, ETH Zurich, Zurich. doi: 10.3929/ethz-a-004121274, 2000.

36. Emmanuel, L.; Hounguè, N.; Biaou, C.; Badou, D. Statistical Analysis of Recent and Future Rainfall and Temperature Variability in the Mono River Watershed (Benin, Togo). *Climate* **2019**, *7*, 8, doi:10.3390/cli7010008.

37. R Core Team R: A language and environment for statistical computing. R Foundation for Statistical Computing, Vienna, Austria. URL https://www.R-project.org/. **2021**.

38. Chiarle, M.; Iannotti, S.; Mortara, G.; Deline, P. Recent debris flow occurrences associated with glaciers in the Alps. *Glob. Planet. Change* **2007**, *56*, 123–136, doi:10.1016/j.gloplacha.2006.07.003.

39. World Glacier Monitoring Service, W. WGMS (2021): Fluctuations of Glaciers Database.Zurich, Switzerland. DOI:10.5904/wgms-fog-2021-05. Online access: http://dx.doi.org/10.5904/wgms-fog-2021-05 2021.

40. Zemp, M.; Kääb, A.; Hoelzle, M.; Haeberli, W. GIS-based modelling of glacial sediment balance. *Zeitschrift fur Geomorphol. Suppl.* **2005**, *138*, 113–129, doi:10.5167/uzh-40580.

41. Haeberli, W. Factors influencing the distribution of rocky and sedimentary glacier beds. - Hydraulic effects at the glacier bed and related phenomena. *Mitteilungen der Versuchsanstalt für Wasserbau, Hydrol. und Glaziologie* **1986**, *90*, 48–49.

42. Paul, F.; Kääb, A.; Haeberli, W. Recent glacier changes in the Alps observed by satellite: Consequences for future monitoring strategies. *Glob. Planet. Change* **2007**, *56*, 111–122, doi:10.1016/j.gloplacha.2006.07.007.

43. Pelto, M.S. Forecasting temperate alpine glacier survival from accumulation zone observations. *Cryosph.* **2010**, *4*, 67–75, doi:10.5194/tc-4-67-2010.

44. Colucci, R.R.; Guglielmin, M. Precipitation-temperature changes and evolution of a small glacier in the southeastern European Alps during the last 90 years. *Int. J. Climatol.* **2015**, *35*, 2783–2797, doi:10.1002/joc.4172.

45. Boeckli, L.; Brenning, A.; Gruber, S.; Noetzli, J. Permafrost distribution in the European Alps: calculation and evaluation of an index map and summary statistics. *Cryosph.* **2012**, *6*, 807–820, doi:10.5194/tc-6-807-2012.

46. Seppi, R.; Zanoner, T.; Carton, A.; Bondesan, A.; Francese, R.; Carturan, L.; Zumiani, M.; Giorgi, M.; Ninfo, A. Current transition from glacial to periglacial processes in the Dolomites (South-Eastern Alps). *Geomorphology* **2015**, *228*, 71–86, doi:10.1016/j.geomorph.2014.08.025.

47. Seppi, R.; Carturan, L.; Carton, A.; Zanoner, T.; Zumiani, M.; Cazorzi, F.; Bertone, A.; Baroni, C.; Salvatore, M.C. Decoupled kinematics of two neighbouring permafrost creeping landforms in the Eastern Italian Alps. *Earth Surf. Process. Landforms* **2019**, *44*, 2703–2719, doi:10.1002/esp.4698.

Chapter 5

Final dissertation

5 Final dissertation

This thesis is a comprehensive and extended study of the Montasio Glacier and of its dynamics in the last century, based on the application of different high-resolution techniques for the estimation of geometric variations and geodetic mass balance. The results were compared with seasonal/annual series of meteorological variables, to enable an interpretation of observed changes and possible inference of the behaviour of the glacier in the next future (Chapter 3-4).

Before glacier applications, the repeatability and reproducibility of the SfM-MVS technique were tested under different acquisition and processing conditions (i.e., camera, GCP number, GCP coordinate precision, and UAV flight mode) over off-glacier, debris covered and easy-to-access study areas, characterised by different morphologies (Chapter 2). High precisions were obtained when repeated flights were performed with the same sensor, whereas significant discrepancies emerged when 3D models of challenging scenarios (i.e., flat surfaces with homogeneous texture) were calculated from images acquired with different cameras. These aspects should be properly addressed before performing elevation change analysis, to avoid systematic errors. Results from Chapter 2 showed a great potential for SfM-MVS repeated surveys over debris-covered areas, which were in fact confirmed when the technique was applied to the Occidentale del Montasio Glacier, obtaining errors around 0.15 m in recent surveys (Chapter 3) and achieving 0.69 m error in DEM reconstruction from historical data (Chapter 4).

These errors translates into errors in annual geodetic balance rates comprised between 0.01 and 0.13 m w.e., which are within the range of geodetic balance errors reported in the literature [1, and references therein].

Results from Chapters 3 and 4 provide a century-long reconstruction and analysis of changes for a very small glacier in the Alps. This is an original and rare outcome, almost unique considering the characteristics of the Montasio Glacier. The study allows to greatly improve our understanding on the climatic response of Montasio Glacier, and highlighted a peculiar behaviour compared to most other monitored glaciers in the European Alps. The Montasio Glacier behaved similarly to most of the alpine glaciers before the 1980s, with a rapid lowering until the 1940s followed by a period of smaller mass loss rates (Chapter 4). After the 1980s, the glacier mass loss increased, in response to a dramatic change in climatic conditions, which mostly affected air temperature. Between 1988 and 1998, the glacier lost high amount of volume, due to combined rising temperature and decreasing precipitation.

Recent dynamics in the period from 2006 to 2020, both from long-term investigations (Chapter 4) and repeat annual surveys (Chapter 3), show an unusual behaviour compared to alpine reference glaciers. Indeed, the Montasio Glacier experienced a mass balance close to balanced-budget conditions (-0.07 m w.e. y^{-1}), while at the same time the largest part of monitored glaciers underwent increasing rates of mass loss, in particular after 2002. Precipitation was found to play a dominant role in regulating the annual mass balance of the Montasio Glacier, while sensitivity to air temperature was considerably lower. This behaviour seems to be linked primarily to the debris cover extent and thickness, whit a significant role played also by the avalanche concentration over a small area, and the shadowing of the ice body by the Jof di Montasio. The glacier mass loss rate started to decrease at the end of the 1990s in conjunction with a sensible increase in the thickness and extend of the debris cover. Recent snowy winters in the years 2004, 2009, 2013, 2014, brought large amount of snow over the glacier, leading to highly positive mass balances, which compensated warmer ablation seasons.

With the current and ongoing global warming, the glacier monitoring is becoming more and more important, not only for ice free glaciers but also for those that are partially debris covered and fed by avalanches. The latter are usually small and characterized by smaller elevation changes and, therefore, require higher precisions in topographic survey methods. The SfM-MVS is a cost-effective technique to obtain high quality annual surveys for this type of glaciers. The high-resolution annual monitoring data discussed in this thesis allows a clear comprehension of the Montasio Glacier dynamics, and enables also a characterization of vertical and horizontal displacement rates. These activities should be carried on in the future, possibly integrating SfM-MVS with other techniques such as laser scanners mounted on UAVs. Finally, it would also be interesting to extend the historical reconstruction analysis to other very small glaciers in the Alps with similar characteristics (for example in the Dolomites) in order to compare their behaviour and obtain a characterization over a larger spatial scale.

REFERENCE

1. Zemp, M.; Thibert, E.; Huss, M.; Stumm, D.; Rolstad Denby, C.; Nuth, C.; Nussbaumer, S.U.; Moholdt, G.; Mercer, A.; Mayer, C.; et al. Reanalysing glacier mass balance measurement series. *Cryosph.* **2013**, 7, 1227–1245, doi:10.5194/tc-7-1227-2013.